2012

THE EFFECTS OF MICRO- AND MACRO-SCALE GEOMETRIC PARAMETERS ON PERFORMANCE OF THE PLEATED AEROSOL FILTERS

Shahryar Fotovati
Virginia Commonwealth University

School of Engineering
Virginia Commonwealth University

This is to certify that the Dissertation prepared by Shahryar Fotovati entitled THE EFFECTS OF MICRO- AND MACRO-SCALE GEOMETRIC PARAMETERS ON PERFORMANCE OF THE PLEATED AEROSOL FILTERS has been approved by his or her committee as satisfactory completion of the thesis or dissertation requirement for the degree of Doctor of Philosophy

Dr. Hooman V. Tafreshi, School of Engineering

Dr. Gary C. Tepper, School of Engineering

Dr. Ramana M. Pidaparti, School of Engineering

Dr. P. Worth Longest, School of Engineering

Dr. Stephen S. Fong, School of Engineering

Dr. Umit Ozgur, School of Engineering

Dr. J. Charles Jennett, Dean of the School of Engineering

Dr. F. Douglas Boudinot, Dean of the School of Graduate Studies

MARCH 12, 2012

THE EFFECTS OF MICRO- AND MACRO-SCALE GEOMETRIC PARAMETERS ON PERFORMANCE OF THE PLEATED AEROSOL FILTERS

A Dissertation submitted in partial fulfillment of the requirements for the degree of Doctor of Philosophy at Virginia Commonwealth University.

by

SHAHRYAR FOTOVATI
MS in Mechanical Engineering, Shiraz University, IR, 2007
BS in Mechanical Engineering, Persian Gulf University, IR, 2001

Director: HOOMAN V. TAFRESHI
QIMONDA ASSISTANT PROFESSOR, DEPARTMENT OF MECHANICAL AND NUCLEAR ENGINEERING

Virginia Commonwealth University
Richmond, Virginia
March 2012

Acknowledgement

First and foremost, I offer my sincere gratitude to my supervisor, Dr. Hooman V. Tafreshi, who has supported me throughout my PhD studies with his patience and knowledge while allowing me the room to work in my own way. I attribute the level of my PhD degree to his encouragement, enthusiasm, and immense knowledge. One simply could not wish for a better or friendlier supervisor.

Besides my advisor, I would like to thank the rest of my thesis committee: Professor Tepper, Professor Longest, Professor Pidaparti, Professor Fong, and Professor Ozgur, for their insightful comments, and hard questions.

This work was supported by The Nonwovens Institute at NC State University. Their financial supports are highly appreciated.

Last but not least, I would like to thank my family: my parents, Mahvash and Shahram, my sister, Shahrzad and my beautiful Morvarid for supporting me spiritually throughout my life. They always soften the life difficulties for me. I owe all my achievements to them and I am happy to devote this work to them.

Table of Contents

List of Tables

Page

List of Figures

Page

Abstract

THE EFFECTS OF MICRO- AND MACRO-SCALE GEOMETRIC PARAMETERS ON PERFORMANCE OF THE PLEATED AEROSOL FILTERS

By Shahryar Fotovati, M.Sc.

A Dissertation submitted in partial fulfillment of the requirements for the degree of Doctor of Philosophy at Virginia Commonwealth University.

Virginia Commonwealth University, 2012

Major Director: Dr. Hooman V. Tafreshi
Qimonda Assistant Professor, Department of Mechanical and Nuclear Engineering

While most filters are made of pleated fibrous media, almost all existing theories of aerosol filtration are developed for flat media placed perpendicular to the air flow. Expressions developed for flat sheet media do not provide accurate information directly useful for designing a pleated filter, and therefore, most progress made in developing pleated filters is based on empiricism. This study is aimed at establishing an enabling knowledge that allows for a better design and optimization of pleated aerosol filters. This study is focused on developing a predictive simulation method that accounts for the influence of a filter's micro-scale geometric parameters, such as fiber orientation, as well as its macro-scale

features, like pleat shape, in predicting the transient pressure drop and collection efficiency with or without the effects of dust loading. The dual-scale simulation method developed in this work is believed to be the only feasible approach for design and optimization of pleated aerosol filters with the current academic-level computational power.

Our study is divided into two major tasks of micro- and macro-scale modeling. Our micro-scale studies are comprised of a series of CFD simulations conducted in virtual 2-D or 3-D fibrous geometries that resemble the internal micro-structure of a fibrous medium. These simulations are intended to isolate the effects of each micro structural parameter and study its influence on the performance of the filter medium. In detail, it is intended to propose a method to predict the performance of micro-structures with fiber size distribution. Also, the effects of micro-structural fiber orientation were investigated. Moreover, we offered methodology to predict the performance of noncircular fibers using available analytical expressions for circular fibers. It is shown that the circumscribed circle for a trilobal shaped fiber gives the best prediction for collection efficiency. In macro-scale simulations, on the other hand, the filter medium is treated as a lumped porous material with its properties obtained via micro-scale simulations. Our results showed that more number of pleats helps better performance of pleated filters, however, if the pleat channel becomes blocked by dust cake then this effect is no longer valid.

CHAPTER 1 Background Information

Many works have been devoted to study of flow in nonwoven media and model and even optimize them especially if they are used as aerosol filters. In some studies, only the clean structures were assumed, however, in very few, dust depositions inside media were considered. At first, we briefly review the theory of aerosol filtration and introduce analytical expressions which will be used for validations purposes or introduce micro-scale parameters in macro-scale modeling in other chapters. Another part of this chapter is focused on introducing pleated filters as they are used as our macro-scale domain.

1.1 Aerosol Filtration from a Micro-Scale Point of View

Usually, Performance of any fibrous structure is pointed by their filtration characteristics or more specifically, their pressure drop and particles collection efficiencies. Performance of fibrous media has been studied for many years and there are many analytical, numerical, and/or empirical correlations available for such calculations. In almost all of these studies a fibrous medium is assumed to be made up of fibers with a unimodal circular fiber diameter distribution (referred to as unimodal or mono dispersed medium here), placed normal to the flow. It is more general to refer to permeability (inversely proportional to pressure drop) of a medium instead of pressure drop. There are various well-known models for predicting the pressure drop or permeability of such media. In almost all permeability models, permeability of unimodal media, k, is presented as a function of fiber radius, r,

and Solid Volume Fraction (SVF), α, of the media regardless of dust deposition(Tafreshi et al. 2009, Jaganathan et al. 2008):

$$\frac{k}{r^2} = \frac{1}{f(\alpha)} \tag{1.1}$$

Where, $f(\alpha)$ is referred to as dimensionless pressure drop and is only a function of solid volume fraction.

Collection efficiency of a fibrous structure is defined as the fraction of the particles which were captured by the fibrous medium. Knowing the number (concentration) of the particles at the inlet and outlet gives us the collection efficiency of fibrous medium:

$$E = \frac{N_{\text{inlet}} - N_{\text{outlet}}}{N_{\text{inlet}}} \tag{1.2}$$

It is common to relate the collection efficiency to the penetration, the penetration is:

$$P = \frac{N_{\text{outlet}}}{N_{\text{inlet}}} \tag{1.3}$$

and therefore the collection efficiency is:

$$E = 1 - P \tag{1.4}$$

1.1.1 Pressure Drop of the Clean Fibrous Structures

One of the most popular methods to predict the pressure drop of fibrous media is based on the single fiber theory. In this method, according to pressure drop of a single circular fiber, the total filter pressure drop will be estimated. In pioneering works done by Kuwabara

(1959) and Happel (1959), cell model was proposed to obtain an acceptable prediction for performance of a single fiber. In this model, parallel circular cylinders are distributed randomly and homogeneously in a viscous flow. They considered a circular cylindrical fiber enclosed by imaginary coaxial circle. In that model, the Stokes approximation was used to define the stream function as:

$$\psi = \left(Ar + \frac{B}{r} + C\,ln\left(\frac{r}{R}\right) + D r^3 \right) sin\theta \qquad (1.5)$$

where A, B, C and D are constants to be found. The stream function ψ, was obtained by the general solution for Stokes flow equation which is as:

$$\left[\frac{1}{r}\frac{\partial}{\partial r}\left(r\frac{\partial}{\partial r}\right) + \frac{1}{r^2}\frac{\partial^2}{\partial \theta^2} \right]^2 \psi = 0 \qquad (1.6)$$

Kuwabara assumed the vorticity to vanish at the outer boundary, and found the constants in equation (1.5) and he proposed the dimensionless pressure drop to be as:

$$f\ \alpha\ = \frac{4\alpha}{Ku} \qquad (1.7)$$

Ku in equation (1.7) is Kuwabara factor which can be expressed as:

$$Ku = -\frac{1}{2}\ln\ \alpha\ - 0.75 + \alpha - \frac{\alpha^2}{4} \qquad (1.8)$$

Happel used a given tangential stress and found constants in equation (1.5) and came up with the following expression for dimensionless pressure drop:

$$f\ \alpha\ = \frac{4\alpha}{\left(-\frac{1}{2} ln\ \alpha\ - \frac{1}{2}\frac{1-\alpha^2}{1+\alpha^2} \right)} \qquad (1.9)$$

Works of Kuwabara and Happel are limited to some special boundary conditions that they assumed. Other definitions for dimensionless pressure drop proposed and are available in literature inspired by work of Kuwabara, but for more general arrangements of fibers. Henry and Ariman (1983) numerically solved the flow field around a staggered array of parallel circular cylindrical fibers and offered the following for dimensionless pressure drop:

$$f\ \alpha\ = 2.446\alpha + 38.16\alpha^2 + 138.9\alpha^3 \qquad (1.10)$$

One of the most important correlations for dimensionless pressure drop for randomly oriented layered fibrous structure was proposed by Davis (1973) which holds for vast range of solid volume fractions of 0.6% to 30%:

$$f\ \alpha\ = 64\alpha^{3/2}\ 1 + 56\alpha^3 \qquad (1.11)$$

Some other important expressions for dimensionless pressure drop have been listed in Table 1.1a, as well. In that table, $Kn_f = 2\lambda / d_f$ is the fiber Knudsen number, where λ is the molecular mean free path of air (about 64 nm in normal temperatures and pressures) and d_f is fiber diameter.

In Table 1.1b, the presented common equations give permeability explicitly. In those equations, K_0 and K_1 are zeroth and first order Bessel functions of the second kind, whereas k_{TP}^{lay} and k_{IP}^{lay} are permeability constants in the through-plane and in-plane directions, respectively. By through-plane, this means that the permeability is in the normal direction to the fibrous plane, where, in-plane refers to the direction parallel with the fibrous plane.

The superscript "iso" is used to denote the permeability of a randomly 3-D fibrous medium. In these equations, α is the solid volume fraction of the media and r is the fiber radius. Other expressions can be found in literature which we avoid to mention them here for brevity (Jackson and James 1986, Rao and Faghri 1988). Using the dimensionless pressure drop, the total filter pressure drop according to Darcy's law (Dullien, 1992) will be achieved as follow:

$$\Delta p = f \quad a \quad \frac{\mu U t}{r^2} \tag{1.12}$$

In above expression, μ is viscosity related to the flow, U is the flow face velocity (velocity normal to the fibrous domain) and t is the fibrous domain thickness.

1.1.2 Collection Efficiency of the Clean Fibrous Structures

Single fiber theory holds valid to predict collection efficiency of the fibrous structures. It has to be mentioned that by collecting particles means particle collection by mechanical means and the influence of magnetic force and other attractive forces between aerosol particles and fibers will be neglected. According to single fiber theory, the collection efficiency for single fiber is defined as:

$$E_{\text{single}} = \frac{2Y}{d_f} \tag{1.13}$$

In above d_f is the fiber diameter and Y denotes the distance between a trajectory and the axis passing toward the fiber center, in such a way that particles injecting nearer to the axis than this trajectory will be captured and those which are further will not. Figure 1.1

demonstrates the graphical explanation of Equation 1.13. In this study, we only consider mechanical capture mechanisms, due to Brownian diffusion, interception and impaction.

i. Brownian Diffusion (E_D)

Diffusion motion of the small particles has an important effect on capture efficiency. The flow is at equilibrium and there is a distribution of thermal energy among the gas molecules. When there are particles suspended inside the gas, they become in equilibrium with it and hence, they receive a portion of the gas thermal energy as well. The Brownian motion is caused by a constant energy exchange between gas molecules and suspended particles. According to this fact the particles will start to diffuse randomly (Brownian motion), and due to this random motion, the chance of collision between particles and fibers increases, which leads to capture due to Brownian diffusion. This motion quantifies by diffusion coefficient, which shows how single fiber collection efficiency is related to Brownian diffusion.

ii. Direct Interception (E_R)

This mechanism for capturing particles happens when aerosol particles size is large enough to cause Brownian diffusion to be negligible, but it is not too large to let inertial effects dominate particles motion. Under this circumstance, the particles are following streamlines perfectly. Therefore, the capture due to interception can be explained entirely by the airflow. The streamlines pattern in Stokes flow is independent of velocity. This causes the interception to be also velocity-independent. The particles must have the velocity equal to

that of the airflow and therefore, the air viscosity has no effect on particles. The only important parameters are particles and fibers diameter. The ratio of particles to fibers diameter gives a dimensionless number which quantifies what portion of overall single fiber efficiency is related to direct interception.

iii. Inertial Impaction (E_I)

There are conditions that the particles are not following streamlines. Imagine sharp curvature of streamlines, or any convergence or divergence of them, if acceleration of the air flow is involved, the particles would not follow streamlines perfectly. Obviously, under such conditions, the particles mass or inertia becomes important as well as the Stokes drag exerted by the air over the particles. Considering and solving the equation of motion for a spherical particle with diameter of d_p and velocity of U , inside a flow with viscosity of μ , the stopping time and distance for this particle before it comes to rest can be calculated. These two parameters show that if a particle has larger aerodynamic diameter, this particle will be least able to follow the streamlines. The dimensionless parameter which describes capture by inertial impaction is the ratio between particles stoppage distance and fiber diameter, which refers to the filter characteristic length. This dimensionless parameter is so called Stokes number.

There are different available empirical/analytical expressions which predict the single fiber collection efficiency due to each mechanism, and depend on fibrous medium based on its

solid volume fraction α, fibers diameter d_f, and particles diameter d_p. As we don't intend to discuss how these expressions are derived, we only refer to those expressions that we might use in this study and in the following sections. Any of these expressions which comes to our model, have been listed in Tables 1.2, 1.3 and 1.4 for SFE due to Brownian diffusion, interception and inertial impaction, respectively.

In Table 1.2, Ku is the Kuwabara factor (see equation 1.8), and Pe is Peclet number which is defined as $Pe = U d_f / D$. Here $D = \sigma C_C T / (3\pi \mu d_P)$ is the diffusivity, and σ denotes the Boltzmann constant and is $\sigma = 1.38 \times 10^{-23} (m^2 kg\, s^{-2} K^{-1})$. T and μ are the air temperature and viscosity, respectively, and d_P is the particle diameter. In Table 1.3, R is the ratio of particles to fibers diameter ($R = d_p / d_f$) and the equations are valid for the range of $R < 0.4$.

The Stokes number Stk, in Table 1.4, can be expressed as:

$$Stk = \frac{\rho_P d_P^2 C_C V}{18 \mu d_f} \tag{1.14}$$

In above, the general description for each captured mechanism which is included in this thesis was provided. Knowing the thickness of the fibrous domain t, the total collection efficiency of the filter can be achieved as:

$$E = 1 - exp\left(\frac{-4 \alpha E_\Sigma t}{\pi d_f (1-\alpha)} \right) \tag{1.15}$$

where E_Σ is the overall single fiber efficiency for the medium and can be stated as:

$$E_\Sigma = 1 - \ 1 - E_D \quad 1 - E_R \quad 1 - E_I \tag{1.16}$$

Note that some of these expressions are limited to some assumptions related to special range for particles diameter or SVF. We will use some of aforementioned dimensionless pressure drop and SFE correlations to validate our simulations. We also use them to introduce micro-scale parameters into our macro-scale model and simulate depth deposition,

1.2 Aerosol Filtration from a Macro-Scale Point of View

The main objective of this study is to develop a macro-scale simulation methodology for aerosol filtration that can be implemented with minimum CPU cost. In this method, instead of focusing on fibrous micro-structures, we simulate the filter by assuming it as a lumped porous zone. In particular, this method is applied on pleated filters, as very little previous research exists in the literature. Almost all existing theories of aerosol filtration are developed for flat media placed perpendicular to the air flow direction. These theories have resulted in a series of semi-analytical expressions derived for calculating filter collection efficiency and pressure drop, which have been widely used to design flat panel air filters. Most filters, however, are made of pleated media. Expressions for flat filters do not provide any information directly useful for designing pleated ones. Most of the progress made in developing pleated media has therefore been based on empiricism.

Pressure drop across a pleated filter is caused by two equally important factors. The first and most obvious contributor in the filter's pressure drop is the fibrous medium. The second contributing factor is the pleat geometry. In a pioneering work, Chen *et al.* (1995)

modeled the pressure drop across clean filters with rectangular pleats using a finite element method and discussed the influence of the above factors in a filter's total pressure drop. These authors also showed that increasing the pleat count increases the pressure drop due to the geometry but decreases that caused by the fibrous media. Therefore, there exists an optimum pleat count at which the total pressure drop of a clean pleated filter is a minimum. Raynor and Chae (2005) investigated the long term performance of the electrically charged filters in a ventilation system. They tested fifteen pleated filters consisting of two different fibers at each test, with small and large aerosol particles. They proposed a polynomial correlation for the single fiber efficiency and the total fiber efficiency of the tested media. The coefficients however are strongly dependent on their test filters. To our knowledge, there are only very few studies in the literature dedicated to studying the influence of pleat geometry, and almost all of them neglect the effects of dust deposition on pressure drop (Chen *et al.,* 1995; Lucke and Fissan, 1996; Del Fabbro *et al.,* 2002; Caesar and Schroth, 2002; Subernat *et al.*, 2003; Tronville and Sala, 2003; Wakeman *et al.*, 2005; Waghode *et al.*, 2007; and Rebai *et al.*, 2010).

Dust deposition can adversely affect the performance of a filter over time, and surprisingly, it has not yet been included in the theories developed for filter design. The only published work to include the collection efficiency in evaluating the influence of pleat geometry is that of the work of Chen et al. (2008). This work is an experimental observation and although presents some insights into the importance of collection efficiency in filter optimization, do not propose any model useful for product development. These authors

tested V-shaped pleated filters with a solid volume fraction of 15% using DOP particles. They showed that for the particles less that 0.5 μm in diameter, the pleat filters have higher penetration rate than the flat filters, and concluded that face velocity in pleated filters is higher than the velocity of the uniform flow. They reported that filtration efficiency increases with increasing pleat count for the particles with diameter greater than 0.5 μm.

We will consider rectangular (U-shaped) and triangular (V-shaped) pleat shapes with different dimensions, and solve the flow field with and without dust load. Figure 1.2 shows the sample geometries that will be used to model pleated filters in this thesis. In this figure, the independent geometrical parameters are shown where they are pleat height L, pleat distance d, and pleat angle 2θ. Boundary conditions are presented in this figure as well. In addition, the inlet velocity and face velocity are shown individually. The difference between inlet and face velocity should be noticed as the inlet velocity has a constant magnitude and denotes flow velocity at the far field, upstream of the media. However, face velocity is the one at which the flow enters the medium and it varies locally. The pleats can be considered as channels with permeable walls. At the inlet of the channel, the streamlines will be contracted and rotated to enter into the channels. The flow will start to enter the medium and the amount of mass inside the pleats will be reduced as we go deeper inside the channels. Therefore, the centerline velocity and face velocity magnitude will vary as flow penetrates into the channels. In addition, the pleat count (pleat distance or pleat angle) and pleat height will strongly affect the velocity profile inside the pleats. We expect to see different flow pattern inside rectangular and triangular geometries as well. At the pleat

channel inlet, streamlines have to contract and rotate even more sharply when the geometry has rectangular shape. Previously, it was mentioned that particle size is the main factor to specify how that particle follows streamline and based on what mechanism they will be captured. It was pointed out that highly inertial particles will not follow streamlines if they have sharp curvature or they converge or diverge fast. This becomes very important when deposition of highly inertial particles starts, where these particles are not going to follow streamlines and therefore, with different injected particles size, the dust cake pattern is expected to be formed differently.

It is known that the dimensions of pleated geometries are usually on the order of centimeters, while scales of the filter's internal structure are ten thousand times smaller (see Figure 1.3). The best way to model such geometries is dual-scale modeling. At micro-scales we study the effects of in-plane and/or through-plane fiber orientation, fiber diameter, and other microstructural parameters, while at macro-scales we investigate the influence of pleat geometry. The first step to predict the performance of a pleated filter is to study the importance of the flat sheets microstructural parameters. To obtain the permeability of the fibrous medium, components of permeability tensor have to be calculated. These components are related to the flow direction with respect to the fibers' plane. For any given flow direction, there will be a component describing the medium's permeability normal to the fibers' plane, and another component representing the permeability parallel with the fibers. To model dust deposition, two methodologies will be chosen. In one step, we consider the fibrous medium to be highly efficient (such as that of

a HEPA filter), and hence all the aerosol particles are assumed to be captured as they hit the filter surface. Dust surface deposition pattern will be modeled and demonstrated as a result. In order to model deposition, we will use Lagrangian approach. In addition, the dust cake properties can be obtained if the cake is considered as a granular bed of particles. As mentioned earlier, different pleated geometries, particles size and flow regimes, cause different dust cake, and hence the pleated filter performance will change and can be optimized. In general, the depth deposition will take place before surface deposition occurs. To model more accurate dust cake, the second method is to consider depth and surface deposition combined together. To do so, we introduced Eulerian-Lagrangian approach. The details related to these methodologies will be explained in following sections. Also, in many practical applications, the filters will not face mono-dispersed particles. As will be seen later, simulating poly-dispersed dust cake is a real challenge. However, it is of the interest to model deposition of particles with different diameters. According to the literature, not many researches can be found on poly-dispersed particle deposition and most of the available works are devoted to study mono-dispersed beds of particles (Dullien, 1992, and Kasper et al., 2010). As will be explained in following sections, we intend to define a novel method to simulate dust cake made of the poly-dispersed particle distribution.

Table 1.1a: Commonly used expressions for dimensionless pressure drop

Eq. No.	Investigator(s)	Dimensionless pressure drop, $f(\alpha)$
(1.17)	Brown (1993)	$\frac{4\alpha\left(+1.996\,Kn_f\right)}{Ku+1.996\,Kn_f\,(-0.5\ln\alpha-0.25+\alpha^2/4)}$
(1.18)	Drummond and Tahir (1984)	$\frac{8\alpha}{-\ln\alpha-1.476+2\alpha-1.774\alpha^2}$

Table 1.1b: Commonly used expressions for permeability

Eq. No.	Investigator(s)	Permeability, k
(1.19)	Spielman and Goren (1968)	$\frac{1}{4\alpha}=\frac{1}{4}+\frac{3}{4}\frac{\sqrt{k_{IP}^{lay}}}{r}\frac{K_1(r/\sqrt{k_{IP}^{lay}})}{K_0(r/\sqrt{k_{IP}^{lay}})}$
(1.20)	Spielman and Goren (1968)	$\frac{1}{4\alpha}=\frac{1}{2}+\frac{\sqrt{k_{TP}^{lay}}}{r}\frac{K_1(r/\sqrt{k_{TP}^{lay}})}{K_0(r/\sqrt{k_{TP}^{lay}})}$
(1.21)	Spielman and Goren (1968)	$\frac{1}{4\alpha}=\frac{1}{3}+\frac{5}{6}\frac{\sqrt{k^{iso}}}{r}\frac{K_1(r/\sqrt{k^{iso}})}{K_0(r/\sqrt{k^{iso}})}$

Table 1.2: Expressions for SFE due to Brownian diffusion

Eq. No.	Investigator(s)	SFE expressions for diffusion
(1.22)	Stechkina (1966)	$E_D = 2.9 Ku^{-1/3} Pe^{-2/3} + 0.62 Pe^{-1}$
(1.23)	Liu and Rubow (1990)	$E_D = 1.6\left(\frac{1-\alpha}{Ku}\right)^{1/3} Pe^{-2/3} C_d \quad C_d = 1 + 0.388 Kn_f \left(\frac{(1-\alpha)Pe}{Ku}\right)^{\frac{1}{3}}$
(1.24)	Payet (1991)	$E_D = 1.6\left(\frac{1-\alpha}{Ku}\right)^{1/3} Pe^{-2/3} C_d C_d' \qquad C_d' = \frac{1}{1 + (E_D)_{Liu\&Rubow}}$
(1.25)	Lee and Liu (1982)	$E_D = 1.6\left(\frac{1-\alpha}{Ku}\right)^{1/3} Pe^{-2/3}$
(1.26)	Pich (1965)	$E_D = 2.27 Ku^{-1/3} Pe^{-2/3}(1 + 0.62 KnPe^{1/3} Ku^{-1/3})$

Table 1.3: Expressions for SFE due to interception

Eq. No.	Investigator(s)	SFE expressions for interception
(1.27)	Lee and Gieske (1980)	$E_R = \frac{1-\alpha}{Ku} \frac{R^2}{(+R)^m} \qquad m = \frac{2}{(1-\alpha)}$
(1.28)	Pich (1966)	$E_R = \frac{(1+R)^{-1} - (1+R) + 2(1+1.996 Kn)(1+R)\ln(1+R)}{2(-0.75 - 0.5\ln\alpha) + 1.996 Kn(-0.5 - \ln\alpha)}$
(1.29)	Liu and Rubow (1990)	$E_R = 0.6\left(\frac{1-\alpha}{Ku}\right)\frac{R^2}{(1+R)} C_r \qquad C_r = 1 + \frac{1.996 kn_f}{R}$
(1.30)	Lee and Liu (1982)	$E_R = 0.6 \frac{1-\alpha}{Ku} \frac{R^2}{(1+R)}$

Table 1.4: Expressions for SFE due to inertial impaction

Eq. No.	Regime / Investigator	SFE expressions for inertial impaction
(1.31)	Low Stokes Numbers (Stechkina et al., 1969)	$E_I = \frac{J \times Stk}{4Ku^2}$ $J = (29.6 - 28\alpha^{0.62})R - 27.5R^{2.8}$
(1.32)	Moderate Stokes Numbers (Brown, 1993)	$E_I = \frac{Stk^3}{Stk^3 + 0.77Stk^2 + 0.22}$
(1.33)	High Stokes Numbers (Brown, 1993)	$E_I = 1 - \frac{0.805}{Stk}$

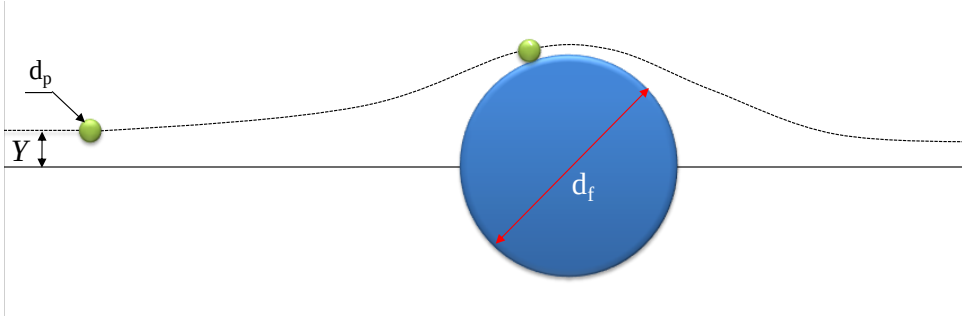

Figure 1.1: Graphical demonstration for single fiber efficiency

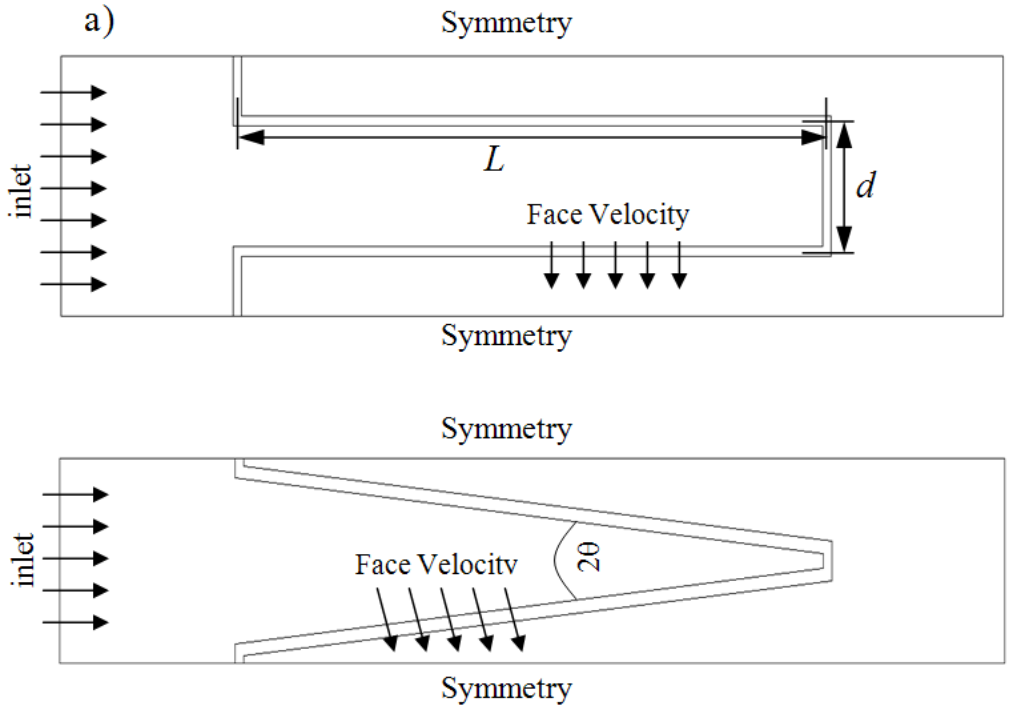

Figure 1.2: Pleated geometry (a) Rectangular geometry, (b) Triangular geometry

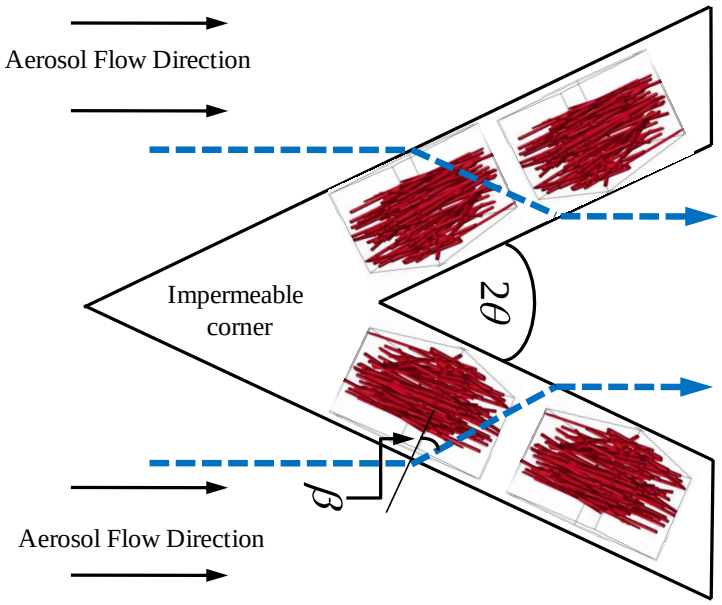

Figure 1.3: Dual scale configuration of a pleated medium

CHAPTER 2 Micro-Scale Modeling of Poly-Dispersed Fibrous Filter Media[♣]

2.1 Introduction

Performance of fibrous media has been studied for many years and there are many analytical, numerical, and/or empirical correlations available for such calculations. In almost all of these studies a fibrous medium is assumed to be made up of fibers with a unimodal fiber diameter distribution (referred to as unimodal medium in this study). However, a great portion of the fibrous filters are made up of blends of coarse and fine fibers (referred to as bimodal filters). In these filters, fine fibers contribute to the high filtration efficiency while coarse fibers provide the mechanical rigidity. Despite their importance, bimodal (or multimodal/poly disperse) media have not been adequately studied in the literature and, unlike the case of unimodal media, there are no simple expressions/correlations that can be used to predict their pressure drop or collection efficiencies. This is partly because there are too many independent, but coupled, variables that need to be included in developing a model for such predictions. Note here that bimodal filters are those made up of blends (intimately mixed) of fibers with two different

[♣] *Contents of this section have been published in an article entitled "Analytical Expressions for Predicting Capture Efficiency of Bimodal Fibrous Filters", by S. Fotovati, H. Vahedi Tafreshi, A. Ashari, S. A. Hosseini, and B. Pourdeyhimi. Journal of Aerosol Science, 41(3), 295–305, 2010.*

diameters, where multimodal or poly dispersed filters have a distribution of fibers with different diameters. This study is the first to develop a reliable expression for calculating permeability and collection efficiency of bimodal fibrous filters. Our simulations are devised to find a unimodal equivalent diameter for each bimodal filter medium thereby take advantage of the existing expressions of unimodal filter media (see Figure 2.1).

There are only a few studies dedicated to the development of predictive models for poly dispersed fibrous material. Almost all of these models deal only with permeability prediction for bimodal media (Lundstrom and Gebart 1995; Clague and Phillips 1997; Papathanasiou 2001; Brown and Thorpe 2001; Jaganathan et al. 2008; Mattern and Deen 2008; and Tafreshi et al. 2009). In this work, for the first time, bimodal filters will be considered for defining a unimodal equivalent diameter in such a way that it can be used with the existing unimodal expressions for collection efficiency prediction. We will expand the model to multimodal (poly dispersed) fibrous media.

2.2 Unimodal Equivalent Diameters of Bimodal Media

There are various expressions that have been developed for predicting pressure drop of unimodal filter media over the past decades (e.g., Drummond and Tahir 1984; Jackson and James 1986). In almost all these models, pressure drop across unimodal media is presented as a function of fiber diameter and Solid Volume Fraction (α) of the media and presented in equation (1.12). We repeat this equation in term of fiber diameter here:

$$\frac{\Delta p}{t} = f\ \alpha\ \frac{4\mu U}{d_f^2} \qquad (2.1)$$

Where μ and U are the fluid viscosity and flow face velocity, respectively, and t is the filter thickness. As mentioned earlier, there are different expressions for dimensionless pressure drop, $f(\alpha)$. In this part of the work, and based on the fiber sizes that we have chosen, the slip boundary conditions have to be considered. According to Table 1.1a, only one of the presented correlations include slip factor and therefore we use that expression for $f(\alpha)$ which was proposed by Brown (1993) (equation 1.17).

For the case of very small particles, capture is mainly due to the Brownian diffusion. As mentioned before Brownian diffusion takes place as a result of a non-uniform temperature field around a very small particle (smaller than about 100nm), which causes the particle to exhibit erratic random displacements with time even in quiescent air. The existence of the above non-uniform temperature field is due to the comparatively infrequent number of collisions between the gas molecules and a very small particle, as the particle is often smaller than the gas molecular mean free path. For this part of the study, single fiber capture efficiency due to Brownian diffusion is given by equation (1.22) in Table 1.2.

For larger particles, where the size and mass of the particles are not negligible, filtration is due to interception and inertial impaction as explained in Chapter 1. Large particles, however, do not exhibit Brownian diffusion. Collection efficiency due to interception is provided according to the work of Pich (1966) and presented in equation (1.28). In this

section, we also compare our results with the expression proposed by Liu and Rubow (1990) which was pointed in equation (1.29) in Table 1.3.

According to the range of particle diameters that we used, inertial impaction has to be added to our work as well. Collection efficiency due to inertial impaction is given by Stechkina *et al.* (1969) in equation (1.31) in Table 1.4. It should be noticed that in regards to the range of particle sizes considered in this part of the study (i.e. 10 nm $< d_p <$ 2 µm), the Stokes number is relatively low and equation (1.31) has been chosen properly.

The total filter efficiency can be approximated by implementing equation (1.16) into equation (1.15) and Particle penetration through a fibrous filter with a thickness of t can be obtained by the adding equation (1.4) in (1.15) which gives:

$$P = \exp\left(\frac{-4\alpha E t}{\pi d_f (1-\alpha)}\right) \qquad (2.2)$$

As mentioned earlier, there are very few studies dedicated to bimodal fibrous media, and all of them are focused on pressure drop predictions. To our knowledge, there is no study in which collection efficiency of a bimodal filter has been modeled for the purpose of developing a predictive correlation. In a recent study, we calculated the pressure drop of a series of bimodal fibrous media, and evaluated eight different methods of defining an equivalent diameter for bimodal media. It was shown that the *area-weighted average* diameter of Brown and Thorpe (2001), equation (2.3); *volume-weighted resistivity* model of Clague and Phillips (1997), equation (2.4); and the *cube root* relation of Tafreshi *et al.* (2009), equation (2.5), offer the best predictions over the entire range of mass (number)

fractions, $0 \le n_c \le 1$, with fiber diameter ratios of $1 \le R_{cf} = d_c / d_f \le 5$, and SVFs of $5\% \le \alpha \le 15\%$:

$$d_{eq}^{(2)} = 2\frac{n_c r_c^{\,2} + n_f r_f^{\,2}}{n_c r_c + n_f r_f} \tag{2.3}$$

$$d_{eq}^{vwr} = 2\sqrt{n_c r_f^2 + n_f r_c^2} \tag{2.4}$$

$$d_{eq}^{cr} = 2\sqrt[3]{n_c r_c^3 + n_f r_f^3} \tag{2.5}$$

Here, n_c, n_f, r_c, and r_f are the number fraction and radius of coarse and fine fibers, respectively. In the current study, we consider these established equivalent diameter definitions, and evaluate their suitability for predicting the particle capture efficiency using aforementioned equations proposed for SFE. Lastly, it is worth mentioning that a filter's pressure drop often increases as a result of an increase in its collection efficiency. This makes it difficult to judge whether or not the filter has been designed properly. To circumvent this problem, Figure of Merit (FOM), also referred to as Quality Factor, has been defined and is widely used in the literature:

$$FOM = -\frac{\ln(P)}{\Delta p} \tag{2.6}$$

2.3 Governing Equations

In this part, we present the governing equations for simulating air and particle flow in a 2-D model of aerosol fibrous filters. The air flow through the micro-structure of a filter is

believed to be governed by the Stokes equation, where the pressure drop is caused solely by viscous forces.

$$\frac{\partial u}{\partial x}+\frac{\partial v}{\partial y}=0 \tag{2.7}$$

$$\frac{\partial p}{\partial x}=\mu\left(\frac{\partial^2 u}{\partial x^2}+\frac{\partial^2 u}{\partial y^2}\right) \tag{2.8-1}$$

$$\frac{\partial p}{\partial y}=\mu\left(\frac{\partial^2 v}{\partial x^2}+\frac{\partial^2 v}{\partial y^2}\right) \tag{2.8-2}$$

For the case of small particles, we considered a convective-diffusive equation for the concentration of the particles based on the Eulerian approach (Friedlander 2000):

$$u\frac{\partial n}{\partial x}+v\frac{\partial n}{\partial y}=D\left(\frac{\partial^2 n}{\partial x^2}+\frac{\partial^2 n}{\partial y^2}\right) \tag{2.9}$$

where n is the nano-particle concentration. Equations (2.7), (2.8-1) and (2.8-2) are numerically solved in a series of bimodal 2-D geometries using the Computational Fluid Dynamics (CFD) code from ANSYS Inc. For larger particles ($d_p \geq 100\,\text{nm}$), we used a Lagrangian modeling approach where each individual particle is tracked throughout the solution domain. In the Lagrangian method, the force balance on a given particle is integrated to obtain the particle position in time. The dominant force acting on a particle is the air drag force. For $\text{Re}_p = \rho V d_p / \mu < 1$ (Li and Ahmadi 1992):

$$\frac{dv_{ip}}{dt}=\frac{18\mu}{d_p^2\rho_p C_c}\left(v_i - v_{ip}\right) \tag{2.10}$$

where v_i and v_{ip} are the respective field and particle velocity in the x or y direction.

When using a unit cell, one needs to use periodic boundary conditions in order for the unit cell to be representative of the whole domain. An alternative approach is to replicate the cells to obtain the required filter thickness (see Figure 2.2). This allows for considering a uniform flow at the inlet. The size of the unit cells depends on the solid volume fraction and diameter of the fibers. Here, we used a square unit cell with a dimension of $h = 0.5\alpha^{-0.5}\sqrt{\pi(n_c\, d_c^2 + (1-n_c)d_f^2)}$. The number of unit cells is not important, since the results are presented per unit thickness of the filter. Note that one of the unit cells is divided into two parts and has been added to the left and right sides of the whole geometry.

The SVF of the filters has been kept at 10% (a reasonable average SVF for filter media), while the fiber diameters, and therefore the cell sizes were varied. Here, the coarse fiber number fraction (n_c) can only be 0, 0.25, 0.50, 0.75, and 1, where the first and last numbers represent the number of coarse and fine fibers, respectively. We studied filters with fiber diameter ratios (R_{cf}) of 1, 2, 3, 5, and 7. The case of $n_c = 0.50$ represents three distinctive fiber arrangements depending on whether different fibers are placed in columns, rows, or staggered fashion (see Figure 2.2c). Here, we only consider the staggered configuration.

2.4 Numerical Approach

Boundary conditions are shown in Figure 2.2b. Uniform velocity and concentration profiles are assumed for the incoming airborne particles at the inlet. It is assumed here that

particles that come in contact with the fibers will be captured and vanished from the solution domain. Note that the inlet and outlet boundaries are placed far up and downstream, so that a uniform flow can be assumed to prevail at the inlet and outlet (Wang et al. 2006, Maze et al. 2007). We used an upstream distance of $L = 5d_c$ and $L = 10d_c$ for our small particle (Eulerian) and large particle (Lagrangian) flow simulations, respectively, to improve the calculation's accuracy. For the case of small particles (Equation 2.9), we assumed $n = 0$ at the fiber surface and $\partial n/\partial x = 0$ at the outlet (no change in the particle concentration flux at the outlet). The upper and lower boundaries are symmetry boundary condition, meaning that gradient of any flow property (velocity, particle concentration …) is zero at these boundaries. For the Lagrangian particle tracking, symmetry boundary conditions act like a perfectly reflecting wall, i.e., particles colliding with the symmetry boundaries will be reflected without any loss of momentum.

Standard Discrete Phase Model (DPM) in the ANSYS code treats the particles as point masses, and therefore cannot calculate particle deposition due to interception. In this work, we developed a UDF that modifies ANSYS's standard DPM to include the particle deposition via interception. This has been done by continuously monitoring the distance between the particles' centers and fibers' surface during the trajectory tracking. If the particle's center of mass reaches a distance of away from a fiber, it will be counted as deposited. Figure 2.3a shows the particle concentration contour plot throughout the domain for a typical bimodal medium considered in this work. Here red to blue represent normalized nano-particle concentration from one to zero. Note that the nano-particle

concentration close to the fibers is almost zero indicating the particle deposition. Figure 2.3b depicts the trajectory of particles' centers of mass for 2μm particles in the same solution domain. For the sake of clarity, only a few particle trajectories are shown. Particles' center of mass trajectories in the first unit cell are shown in Figure 2.3c with a higher magnification. Interception of the particle trajectories by the fibers is evident. Note that particles do not interact with each other. Therefore, one can (and must) release a large number of particles to correctly predict the particle capture via interception and impaction.

For the dimensions considered in this chapter, considerable slip velocity occurs at the fiber surface, as expected for flows with non-zero Knudsen numbers. To add this feature to the ANSYS code, we developed another UDF that enables ANSYS to accept slip velocity at the fiber surface (see Hosseini and Tafreshi 2010 for more details).

Our filter geometries were meshed with triangular cells in the filter zone and quadrilateral cells in the fluid entry and exit zones. Depending on the fiber diameter ratio R_{cf} , 50,000 to 400,000 cells were used in the simulations presented in this chapter. Larger numbers of cells are considered in simulations with greater dissimilar fiber diameters. To ensure that the simulation results are mesh-independent, one of our filter geometries was arbitrarily chosen and the effect of mesh density on its pressure drop and collection efficiency was calculated for different number of mesh points around the perimeter of the finer fiber. As it was shown in our previous work (Jaganathan et al. 2008), increasing the number of mesh points around the perimeter of the fine fibers beyond 40 does not influence the pressure

drop. We therefore used 40 mesh points around the fine fibers in our simulations, and adjusted the mesh in the rest of the domain accordingly.

Figure 2.4 shows the influence of a number of particles introduced at the inlet on the medium's collection efficiency using the Lagrangian method (equation 2.10). The horizontal axis here is the number of particles per unit of length at the inlet N_p / h. It can be seen that particle collection efficiency (due to interception and inertial impaction) is independent of the number density of the particles at the inlet beyond a value of about 2×10^7. It is worth mentioning that we also obtained similar results when injecting particles next to the symmetry boundaries to calculate the critical y-distance (the maximum distance above the fiber axis of symmetry at the inlet where a particle can be intercepted) and used it to calculate the percentage of intercepted fibers as suggested by Wang and Pui (2008).

Figure 2.5 shows a comparison between the results of ANSYS+UDFs and those obtained from the traditional analytical expressions. These results are obtained for a unimodal filter medium with an SVF of 10% and a fiber diameter of 3μm. Note that our large-particle collection efficiency calculations are in relatively good agreement with Equation 1.29 but somewhat differ from the efficiency calculated using Equation 1.28. We therefore used equation 1.29 in this part. Also note that since molecular thermal effects have not been defined for our simulations, no thermal rebound (if any) or any effect of that nature should

be expected from the simulations (thermal rebound has been widely discussed in the literature, see for instance Japuntich et al. 2007).

2.5 Results and Discussions

A series of bimodal media were considered here for the simulations. The fine fiber diameter was fixed at 1μm and the coarse fiber diameters were varied from 1 to 7 μm, while the SVF was kept constant at 10%. Pressure drop and particle penetration were calculated for the above filter media with different coarse fiber fractions $0 \le n_c \le 1$, and compared with each other. Simulations were carried out for particles with diameters in the range of $10 \le d_p \le 2\,\mu\text{m}$, and their penetrations were calculated and compared with the predictions of analytical models.

2.5.1 Equivalent Diameter for Mono-Dispersed Fibrous Media

In this subsection, we examine the accuracy of equations 2.3–2.5 in predicting the pressure drop and collection efficiency of bimodal filter media. Figure 2.6 shows the pressure drop per unit thickness of the a series of bimodal filters having different coarse-to-fine fiber diameter ratios, and over the entire range of coarse fiber number fractions $0 \le n_c \le 1$. It can be seen that the pressure drop decreases by increasing the percentage of coarse fibers. This is probably due to the fact that at a fixed SVF (10% here, for instance), the filter's available surface area decreases by increasing the percentage of coarse fibers, which leads

to fewer frictional effects, and consequently less pressure drops. A similar argument can describe the decrease of the pressure drop upon increasing the diameters' dissimilarity R_{cf} .

Predictions of unimodal equivalent area-weighted average diameter, volume-weighted resistivity model, and the cube root formula, when used for pressure drop calculation, are also shown in Figure 2.6 for comparison. It can be seen that all the three models can closely predict the results of the bimodal numerical simulations as expected.

To investigate the accuracy of these models in predicting particle collection efficiency of a filter medium, we computed the filters' particle penetration per unit thickness, and plotted the results in Figures 2.7 and 2.8 for different diameter dissimilarities (R_{cf}).

In Figure 2.7, we present the penetration of small particles in bimodal filter media, using the above-mentioned unimodal equivalent diameter models (equations 2.3, 2.4, and 2.5). Each diameter model is used in conjunction with equations that we mentioned, and compared with the results of our numerical simulations. The cases of $n_c = 0.25$ and $n_c = 0.75$ are shown here, while the case of $n_c = 0.5$ is combined with the results shown in Figure 2.8. It again can be seen that the area-weighted average diameter, volume-weighted resistivity model, and the cube root formula all provide closely matching predictions. Note in Figure 2.7 that penetration increases as the fiber diameter ratio increases. This is because the dominant collection mechanism for Brownian particles (case of Figure 2.7) is

diffusion, and the collection efficiency for such particles is directly proportional to the fibers' surface area, which decreases with increasing R_{cf} .

In Figure 2.8, we present particle penetration per unit thickness of the media for the entire range of particles considered in this study, $10 < d_p < 2000\,\text{nm}$. Without limiting the generality of the conclusions, here we continue our discussion, using $n_c = 0.5$ for the sake of simplicity of presentation. It can be seen that the *area-weighted average* diameter and the *cube root* formulas provide relatively good matching predictions, although the *cube root* formula seems to have slightly better predictions when the entire range of particles is considered.

To make this comparison more quantitative, we calculated the sum of the squares of the difference between $\ln(P)/t$ obtained from our bimodal CFD simulations, and those of the proposed equivalent diameter definitions for different R_{cf} values (see Table 2.1). It can be seen that the Cube Root average diameter has minimum error at each R_{cf} when compared with the results obtained from the two other average diameters definitions. In Figure 2.8, also note that particle penetration for the whole range of relevant particles, $10 < d_p < 2000$ nm, and increases by increasing the fiber diameter ratio.

The simulations presented here have no limitations with regard to the fiber or particle size. However, it should be noted that the conclusions drawn here are only valid for the range of

parameters considered in the simulations. For instance, the equivalent diameters discussed here may not necessarily be accurate in predicting performance of filters made up of fibers with very dissimilar diameters. Also, it should be noted that our conclusions are based on the assumption that the fibers are clean. Obviously, deposition of particles on the fibers, especially on the fine fibers, can drastically change the media's micro-structure, and renders the definition of an equivalent diameter ineffective.

2.5.2 Figure of Merit

In this section, we study the influence of n_c and R_{cf} on the Figure of Merit (equation 2.6) of bimodal filters. As was demonstrated in previous sections the cube root formula seems to be a suitable model to define an equivalent unimodal diameter for estimating the pressure drop and particle collection efficiency of most bimodal filters. We therefore used this formula, together with the analytical unimodal expressions presented earlier (equations presented in Tables 1–4 in Chapter 1), to study the FOM of bimodal filter media. Figure 2.9 shows the FOM of different bimodal filters having different fiber diameter ratios and coarse fiber number fractions, but a constant SVF of 10%. It can be seen that FOM of bimodal filters increases with increasing R_{cf} when challenged with Brownian particles $d_p < 100$ nm. An opposite trend, however, can be observed when the filter is challenged with larger particles. Comparing the results shown in Figure 2.9, it can also been seen that FOM increases with increasing n_c for Brownian particles ($d_p < 100$ nm) and decreases for larger particles.

2.5.3 Equivalent Diameter for Poly-Dispersed Fibrous Media

In previous sub-section, we demonstrated an efficient way of defining equivalent unimodal fiber diameter for bimodal fibrous media. It is of the interest to investigate the validity of these equivalent diameters for calculating the performance of the multimodal (poly-disperse) fibrous media. Our fiber diameter distribution spread from 2μm to 10μm with actual diameters of 2, 4, 6, 8 and 10 microns. We used equation (2.22) and (2.28) for collection efficiency values to compare with our simulation results (inertial impaction has been neglected here).

Figure 2.10 shows the air flow streamlines in one of our poly-disperse media. Comparison between our results and the above semi-empirical expressions are shown in Figures 2.11 and 2.12 for media with fiber diameters of 2μm and 10μm, respectively. It can be seen that our results are in good agreement with the results of Equation (2.26). We will then use this equation to check our modeling with poly-disperse media.

Figure 2.13a–c demonstrates particle collection efficiency for filters with three different SVFs. In each figure, the normalized error is presented for each equivalent diameter. It can be seen that, for most of particle diameters considered, cube root relation shows an acceptable agreement with least normalized error.

2.6 Experimental Validation

For validation purposes a wet-lay mixing tank was built to produce wet-laid filters using four different fibrous samples. Using an optical microscope, the diameters of the fibers have been measured as shown in Figure 2.14a–d. Also, presented in Table 2.3, is the average diameter and standard deviation of our measurements for each fiber type.

To experimentally verify the accuracy of our cube root formula, we produced series of bimodal filters and tested them in DuPont Richmond. Our bimodal filters were made up of fibers from groups labeled A, D, B, and D. In blending different fibers, we used mass fractions, and by knowing the length and density of each fiber type, the number fractions were calculated for the Equations 2.3–2.5. Filters were produced with a basis weight of 150 GSM. The filters were sandwiched between two mono-filament woven screens. We made three samples for each fraction ratios (three repetitions of each case). For the A-D filters (blends of A-fibers and D-fibers), the coarse mass fractions are: 0%, 57.1%, 80%, 92.3%, and 100%. For the B-D filters, the coarse mass fractions are: 0%, 40%, 66.8%, 85.8%, and 100%. The R_{cf} for blends of A and D fibers is 2.15 and for B and D fibers becomes 1.55.

The results for pressure drop (in the absence of dust loading) are presented in tables 2.2 and 2.3 for A-D blends and B-D blends, respectively. It has to be noticed that the above results are presenting the minimum error between analytical expressions and experiment. As can be seen, both Cube root and Area-weighted formula seem to have the least error

percentage, which indicates that our cube root formula is reliable. The results of this experiment for collection efficiency for both tested blends of fibers are presented in the Figure 2.15. Figures 2.15a–e give the comparison the collection efficiency for blends of A-fibers and D-fibers and their related predicted efficiency using analytical correlations with unimodal equivalent diameter. Note that in Figure 2.15 the difference between experiments and analytical results has been minimized based on unimodal results. Similarly the Cube-root formula (as well as Area-weighted average formula) gives the closes results when compare to experiment. The same trend has been observed for the B-D fiber blends.

2.7 Conclusions

While there are numerous analytical expressions available for predicting the performance of unimodal filter media, there are practically no simple relationships for bimodal filters. In this chapter, we examined three different criteria for defining an equivalent unimodal diameter to be used in the existing expressions for predicting the collection efficiency and pressure drop of bimodal filters. Among the definitions tested, the cube root relation seems to better predict the performance (pressure drop and collection efficiency) of bimodal filters with fiber diameter ratios of $1 \le R_{cf} \le 7$, and coarse fiber fractions of $0 < n_c < 1$, when challenged with particles in the range of 10 nm to 2000 nm. The SVF of the filter media simulated in this work was kept at 10% (a typical value for most air filters).

Simulating series of bimodal media with different properties, we showed that increasing the ratio of fiber diameters, R_{cf} , or number (mass) fraction of coarse fibers, n_c , in filters with constant SVF, leads to smaller pressure drops and greater particle penetrations. Our results revealed that FOM of bimodal filters increases with increasing of R_{cf} when challenged with Brownian particles, and decreases for larger aerosol particles. It has also been shown that FOM increases with increasing n_c for Brownian particles ($d_p < 100$ nm), and decreases for larger particles.

Table 2.1: Sum of the squares of differences between experiment and formulation for $\ln(P)/t$

R_{cf}	Cube Root Average Diameter	Area Weighted Average Diameter	Volume Weighted Resistivity Average Diameter
3	68.40×10^{7}	76.90×10^{7}	87.30×10^{7}
5	3.10×10^{7}	3.50×10^{7}	12.50×10^{7}
7	0.94×10^{7}	1.33×10^{7}	5.63×10^{7}

Table 2.2: Pressure drop results for blends of A-fibers and D-fibers.

Equivalent diameter	Error between simulation and experiment				
	100% c	75% c - 25% f	50% c - 50% f	25% c - 75% f	100% f
Area-weighted	2.3%	0.5%	6.3%	15.3%	5.3%
Volume-resistivity	2.3%	6.7%	6.2%	32.6%	5.3%
Cube-root	2.3%	1.5%	3.8%	15.4%	5.3%
Number-weighted	2.3%	14.3%	20.4%	52.4%	5.3%

Table 2.3: Pressure drop results for blends of B-fibers and D-fibers.

Equivalent diameter	Error between simulation and experiment				
	100% c	75% c - 25% f	50% c - 50% f	25% c - 75% f	100% f
Area-weighted	6.8%	8.5%	5.6%	14.2%	5.3%
Volume-resistivity	6.8%	13.8%	14.1%	18.7%	5.3%
Cube-root	6.8%	8.6%	5.7%	14.4%	5.3%
Number-weighted	6.8%	18.7%	22.3%	31.2%	5.3%

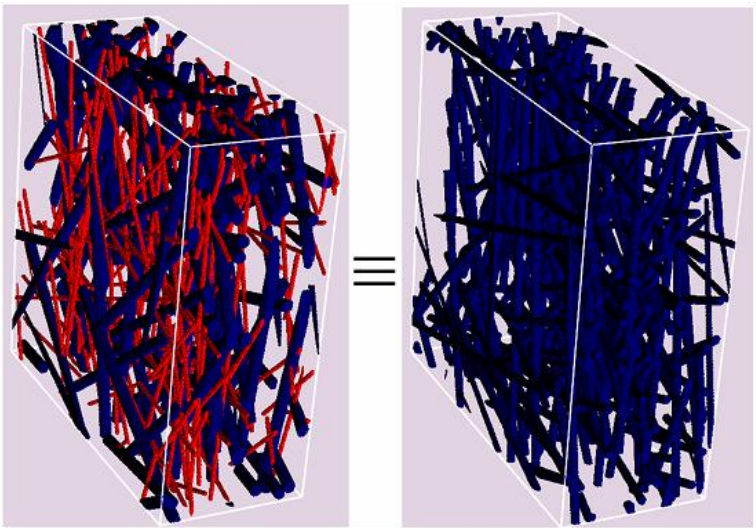

Figure 2.1: An equivalent unimodal fibrous structure (right figure) for each bimodal (poly dispersed) filter medium (left figure)

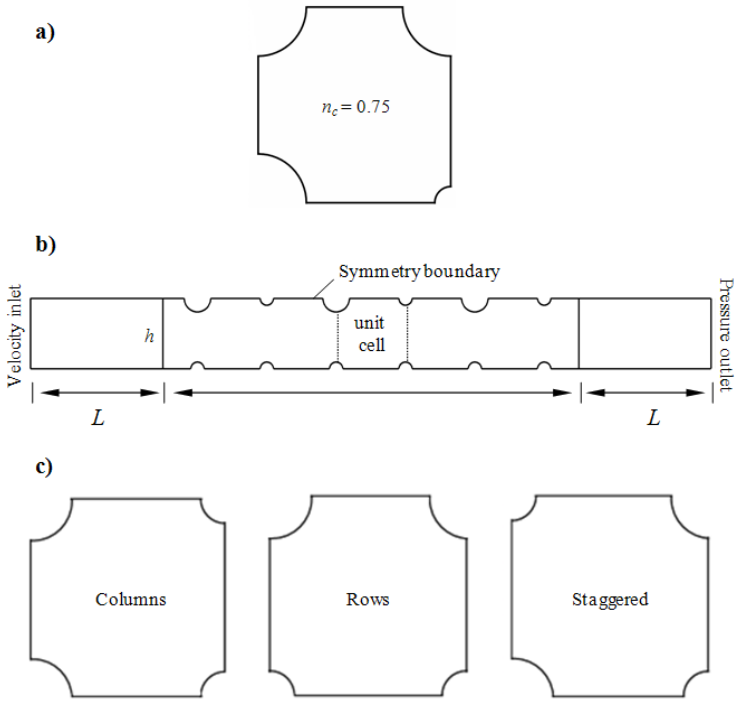

Figure 2.2: a) Square unit cell with one fine and three coarse fibers (n_c = 0.75); b) simulation domain and boundary conditions; c) three possible fiber arrangements of columns, rows and staggered configurations for the case of n_c = 0.5.

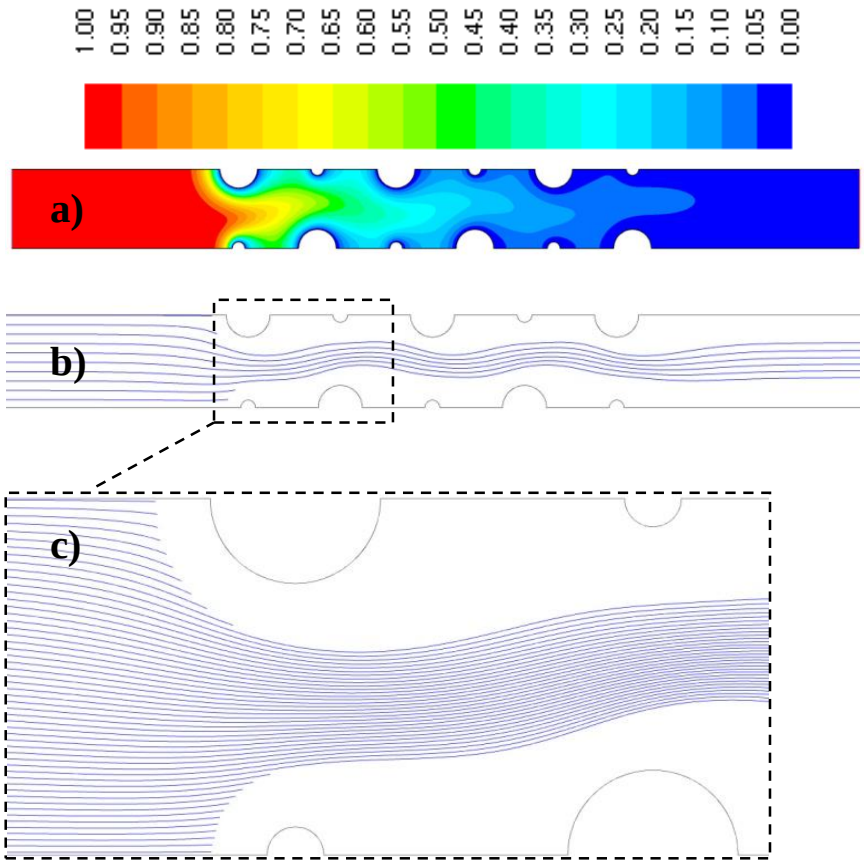

Figure 2.3: a) Contour plot of particle concentration (%) with $d_p = 10\,\text{nm}$; b) trajectories for 2 µm particles; c) particle trajectories in the first unit cell. The filter is made up of fibers of 1 and 3 micron diameter with an SVF of 10%.

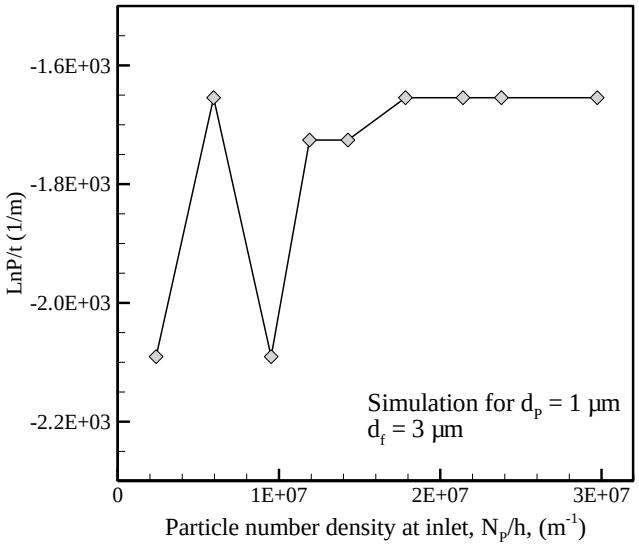

Figure 2.4: Effect of inlet particle number density (mesh density) on particle penetration calculated via Lagrangian Method.

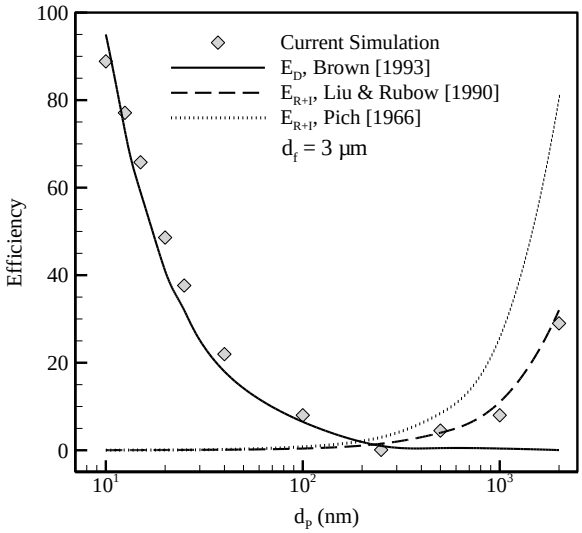

Figure 2.5: A comparison between the efficiency of unimodal medium and analytical expressions.

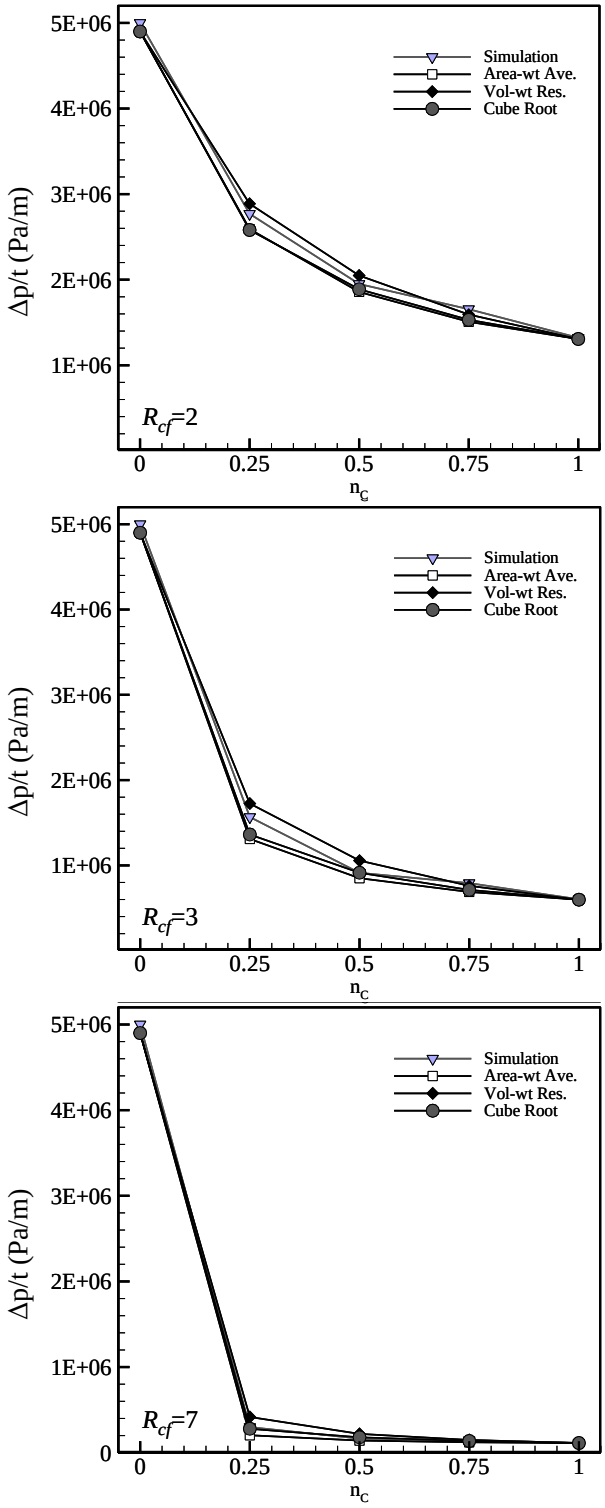

Figure 2.6: Pressure drop per unit thickness of bimodal media

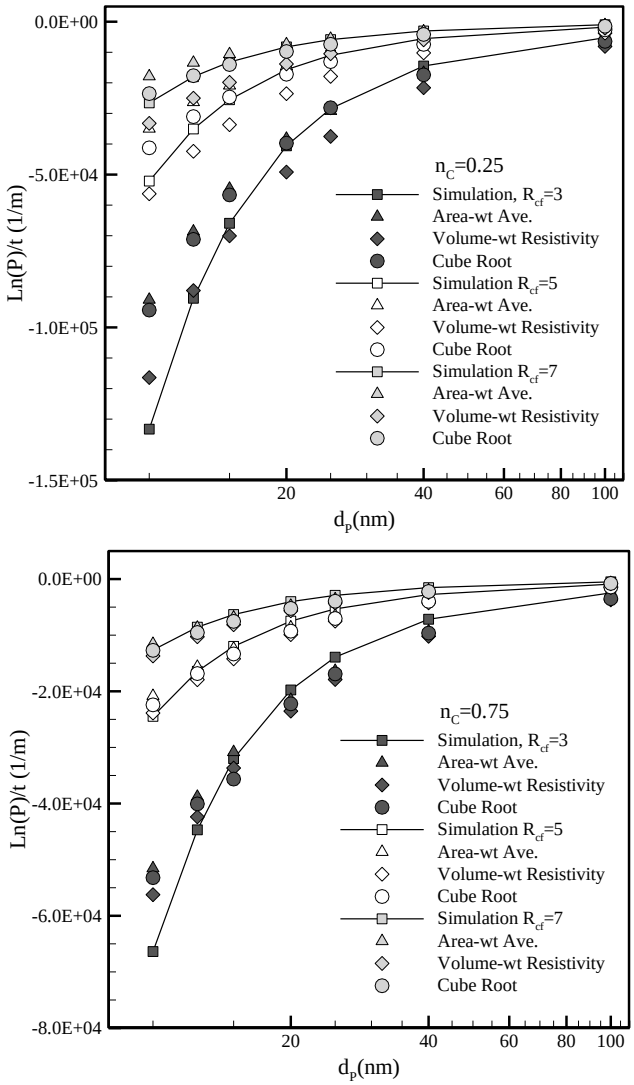

Figure 2.7: Penetration per unit thickness of different bimodal filters with different fiber diameter ratios and coarse fiber number (mass) fractions for Brownian particles.

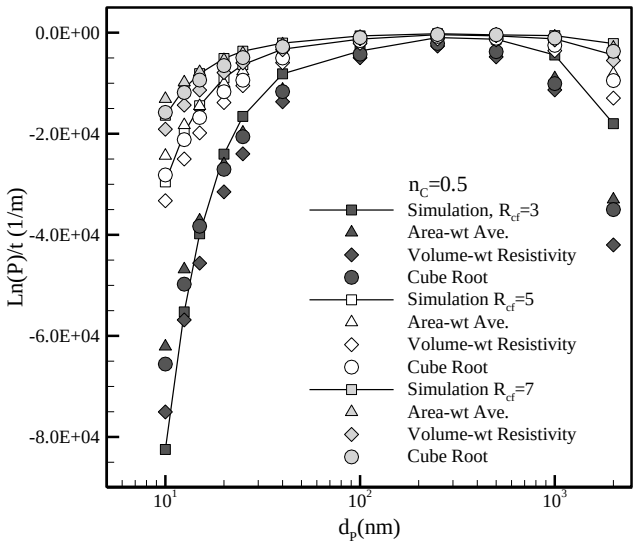

Figure 2.8: Penetration per unit thickness of different bimodal filters with different fiber diameter ratios and coarse fiber number (mass) fractions of $n_c = 0.5$.

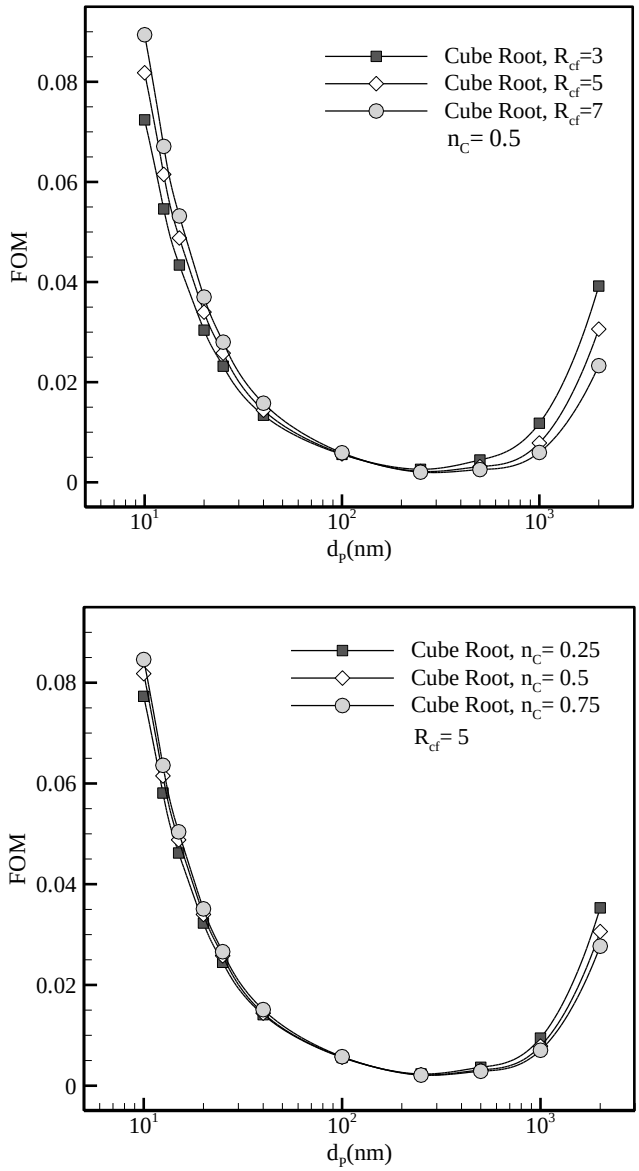

Figure 2.9: Figure of merit of different bimodal filters with different R_{cf} and n_c .

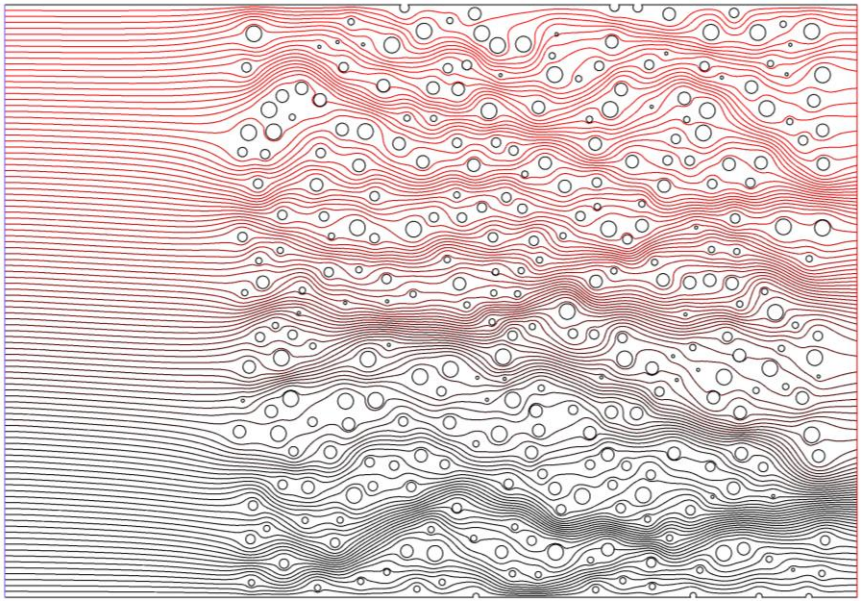

Figure 2.10: An example of our Poly-disperse fibrous medium with fiber diameters in the range of 2μm-10μm. Streamlines are shown to illustrate the flow.

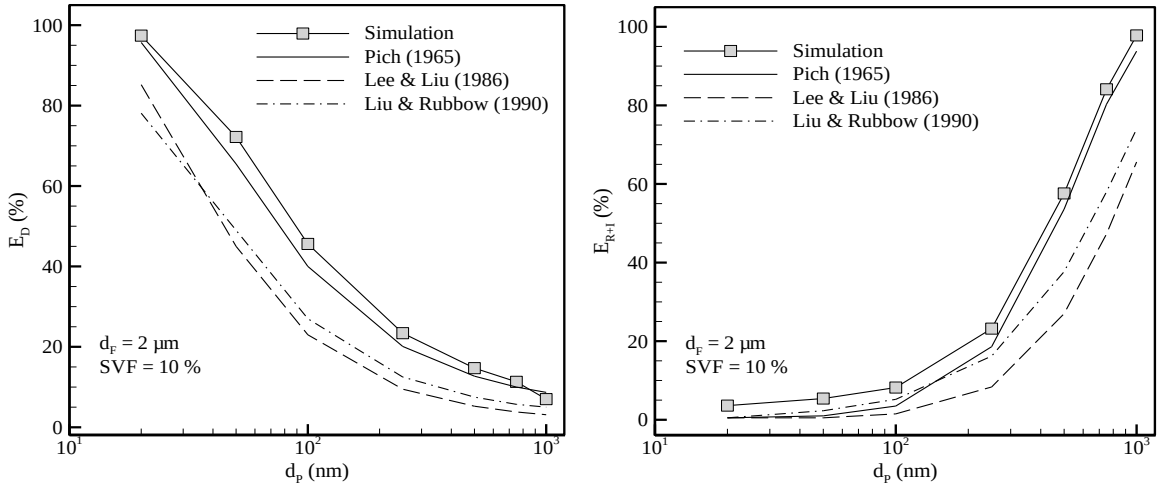

Figure 2.11: Diffusion (left) and interception (right) efficiency of mono-modal filters with $d_f = 2\,\mu m$ in comparison with existing semi-empirical expressions.

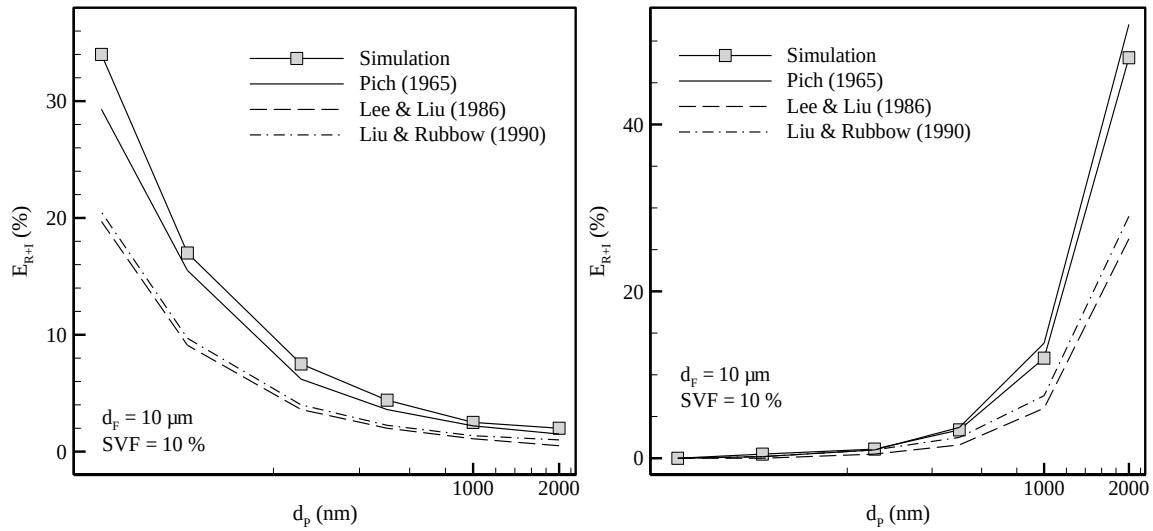

Figure 12: Diffusion (left) and interception (right) efficiency of mono-modal filters with $d_f = 10\,\mu m$ in comparison with existing semi-empirical expressions.

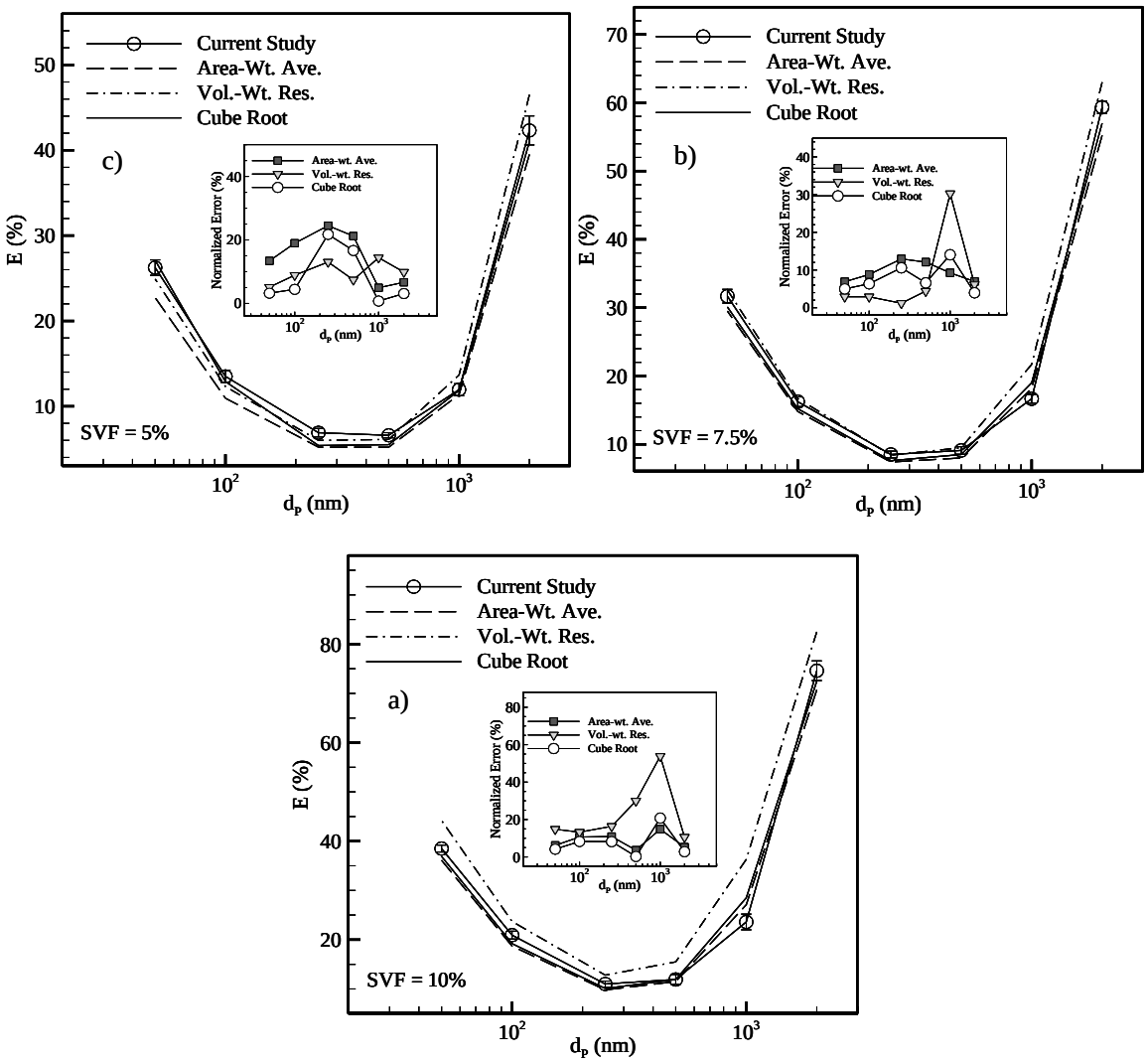

Figure 2.13: Particle collection efficiency for three different SVFs

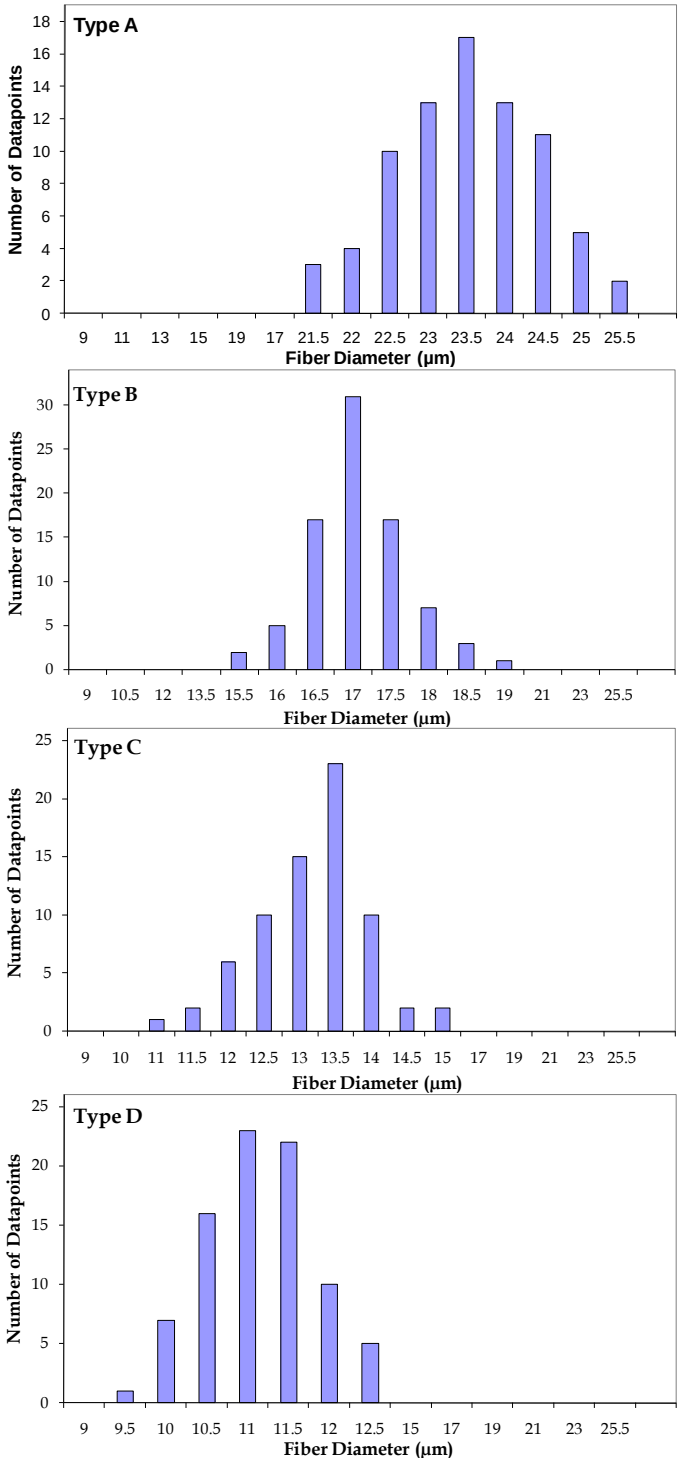

Figure 2.14: Results of fiber diameter measurements.

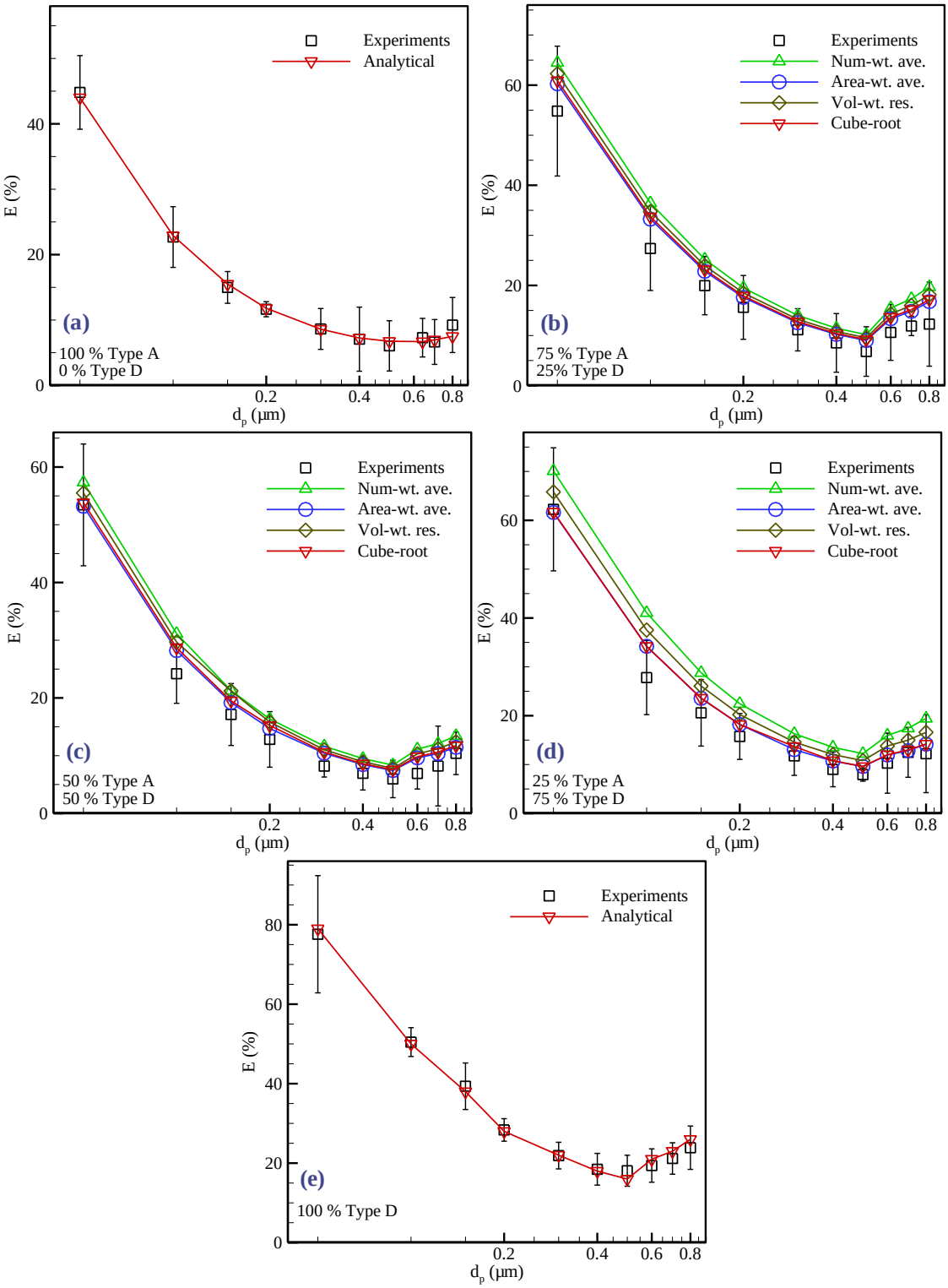

Figure 2.15: Comparison between experimental collection efficiency and predicted values using unimodal expressions with different equivalent definitions (Blends of A & D fibers).

CHAPTER 3 Micro-Scale Modeling of Filter Media with Different Fiber Orientations[♣]

3.1 Introduction

Fibrous filters are generally characterized by their collection efficiency and pressure drop. During the past 50 years, there have been many studies dedicated to the development of mathematical theories for predicting collection efficiency and pressure drop for fibrous media (see Brown 1993 and Spurny 1998 for a complete review). Developing a general filtration theory is computationally expensive, and consequently, almost all previous models were based on oversimplified 2-D geometries in which the fibers were placed in square or hexagonal arrangements perpendicular to flow. Results of such 2-D models were then modified with a variety of empirical correction factors to compensate for errors introduced to the models by unrealistic initial assumptions. The micro-structure of disordered fibrous materials can, in general, be classified in three major categories: unidirectional structures, where axes of all cylindrical fibers are parallel with one another (e.g., Spielman and Goren 1968) (see Figure 3.1a); random layered (planar) structures, where axes of cylindrical fibers lie randomly in parallel planes often perpendicular to the flow direction (e.g., Koponen et al. 1998; Dhaniyala and Liu 1999; Wang et al. 2007; and

[♣] *Contents of this section have been published in an article entitled "Influence of Fiber Orientation Distribution on Performance of Aerosol Filtration Media", by S. Fotovati, H. Vahedi Tafreshi, B. Pourdeyhimi, Chemical Engineering Science, 6(18), 5285–5293, 2010.*

Tahir and Tafreshi 2009; Hosseini and Tafreshi 2010a) (Figure 3.1b); and three-dimensionally isotropic structures, where fibers axes can be randomly oriented in any direction in 3-D space (e.g., Spielman and Goren 1968; Clague and Phillips 1997; Tahir and Tafreshi 2009) (Figure 3.1c).

Even though numerous analytical and experimental investigations have been devised to study fibrous filters, influence of fiber orientation on filtration efficiency of a fibrous medium has not been sufficiently explored. For instance, effects of fibers' in-plane orientation in Figure 3.1b or through-plane orientation in Figure 3.1c have not been well documented. Banks and his co-workers were the first to develop a single-fiber model to study the effects of through-plane fiber orientation on pressure drop and particle collection filtration due to Brownian diffusion (see Banks 1987 and Banks et al. 1990). Schweers and Loffler (1994) contributed to this field by publishing an expression for predicting the role of through-plane fiber orientation in particle capture due to interception. These authors developed a macro-scale model for predicting the filtration efficiency of a non-homogenous filter medium. To our knowledge, no published study has been dedicated to investigate the role of fiber in-plane orientation. This is because studying the effect of in-plane fiber orientation cannot be conducted with either a single-fiber model or with 2-D fibrous geometries. Our objective in this task is to study the effect of both in-plane and through-plane fiber orientations on pressure drop and collection efficiency of fibrous filters.

3.2 Numerical Simulation

3.2.1 Virtual 3-D Micro-Structures

To study the influence of fiber orientation on the filtration efficiency of a fibrous medium, we generated a series of 3-D virtual media using an in-house FORTRAN program (see Tahir and Tafreshi 2009). Unlike our previous micro-scale simulations, here we restrict the in-plane (or through-plane) fiber orientations, when the focus of our study is the effect of through-plane (or in-plane) fiber orientation. This limitation is considered to better isolate the effect of different in-plane or through-plane orientations. Figures 3.2a–c show isometric and top views of media with different in-plane fiber orientations of 15, 30, and 45 degrees, all having a through-plane fiber orientation of zero. Similarly, media shown in Figures 3.2d–f are comprised of fibers having different through-plane orientations of 15, 30, and 45 degrees, but an identical in-plane orientation of zero degree. As can be seen in these figures, while the orientation of the fibers is fixed, their position within the domain is allowed to be random. In order to minimize any flow in the lateral directions, and so better isolate the effect of fiber orientation, we made sure that the number of fibers having an angle of, say 30 degrees, is equal to the number of fibers having an angle of -30 degrees.

3.2.2 Flow Field Calculations

Once the virtual media are generated, Stokes flow equations are numerically solved in the void space between the fibers using the ANSYS CFD code. The Stokes equations are given as:

$$\frac{\partial u}{\partial x}+\frac{\partial v}{\partial y}+\frac{\partial w}{\partial z}=0 \tag{3.1}$$

$$\frac{\partial p}{\partial x}=\mu\left(\frac{\partial^2 u}{\partial x^2}+\frac{\partial^2 u}{\partial y^2}+\frac{\partial^2 u}{\partial z^2}\right) \tag{3.2-1}$$

$$\frac{\partial p}{\partial y}=\mu\left(\frac{\partial^2 v}{\partial x^2}+\frac{\partial^2 v}{\partial y^2}+\frac{\partial^2 v}{\partial z^2}\right) \tag{3.2-2}$$

$$\frac{\partial p}{\partial z}=\mu\left(\frac{\partial^2 w}{\partial x^2}+\frac{\partial^2 w}{\partial y^2}+\frac{\partial^2 w}{\partial z^2}\right) \tag{3.2-3}$$

Our simulation strategy here is based on specifying an inlet face velocity of 0.1 m/s (resulting in a Reynolds number on the order of unity) to obtain the media's pressure drop. For the air flow at the fiber surface, we assumed the no-slip boundary condition. This is because for the air thermal condition and the fiber diameters considered in this chapter, the continuum flow is dominant. We used a SIMPLE algorithm for pressure-velocity coupling along with a second order upwind scheme for the momentum equation discretization. Our criterion for convergence was at least four orders of magnitude reduction in the residuals for the continuity and momentum equations in the x, y, and z-directions. More importantly, we monitored the pressure drop across the media during the iterations to ensure that no significant changes occur in the flow field calculations upon performing further iterations before a simulation is considered to be converged.

Figure 3.3 shows an example of the simulating domains and boundary conditions considered here (flow is in the y-direction). We have used symmetry boundary conditions for the sides of the computational box. The choice of the symmetry boundary condition is

justified considering the fact that no net flows in the lateral directions are expected, as mentioned earlier in this section. The xyz dimensions of the filter media considered in the simulations were kept at 280×290×280 μm^3 (media thickness is 290μm). It is important to ensure that the size of simulation domain is sufficiently large such that the pressure drop values are not dependent on domain size. Here we used the Brinkman screening length criterion, which is given by $\sqrt{k}$, where k is permeability of the medium. According to (Clague and Phillips 1997), a box size of about 14 times larger than the Brinkman's length is sufficient to smooth out the local heterogeneities. Here we used the expression of Davies (1973) (see Section 3.3) to obtain an estimate of the relevant domain size, prior to the simulations (see Tafreshi *et al.* (2009) for more information).

3.2.3 Particle Phase

In this part of the study, again, we considered three basic mechanisms that lead to the capture of an aerosol particle in a neutral filter medium: interception, inertial impaction, and Brownian diffusion. Brownian diffusion is important only for small particles. Interception is important when the size of the particles and fibers are comparable, and inertial impaction becomes considerable only when the particle's momentum is not negligible, either because of its large mass or velocity. The total particle collection efficiency of a filter is the result of a combination of all the above mechanisms.

For the case of small particles, we considered a convective-diffusive equation (Eulerian approach) for the concentration of the particles based on the Eulerian approach:

$$u\frac{\partial n}{\partial x}+v\frac{\partial n}{\partial y}+w\frac{\partial n}{\partial z}=D\left(\frac{\partial^2 n}{\partial x^2}+\frac{\partial^2 n}{\partial y^2}+\frac{\partial^2 n}{\partial z^2}\right) \quad (3.3)$$

To define this equation for ANSYS's PDE solver, we developed a special User-Defined Function (UDF) that was simultaneously executed during the computations. It is assumed that particles which come in contact with the fibers will be captured, and vanish from the solution domain. Note that the inlet and outlet boundaries are placed far up and downstream from the media, so that a uniform flow can be assumed to prevail at the inlet and outlet (Fotovati *et al*. 2010). For the case of small particles (equation 3.3), we assumed $n=0$ at the fiber surface, and $\frac{\partial n}{\partial x}=0$ at the outlet (more completed discussion on these UDF can be found on Chapter 2).

For larger particles ($d_P \geq 100\,nm$), we used a Lagrangian modeling approach, in which each individual particle is tracked throughout the solution domain. In the Lagrangian method (as mentioned in previous chapter for 2-D case), the force balance on a given particle is integrated to obtain the particle's position in time, where, the dominant force acting on a particle is the air drag force. For $\mathrm{Re}_p = \rho V d_p / \mu < 1$ (Li and Ahmadi 1992):

$$\frac{du_p}{dt}=\frac{18\mu}{d_p^2\rho_p C_c}(u-u_p) \quad (3.4\text{-}1)$$

$$\frac{dv_p}{dt}=\frac{18\mu}{d_p^2\rho_p C_c}(v-v_p) \quad (3.4\text{-}2)$$

$$\frac{dw_p}{dt}=\frac{18\mu}{d_p^2\rho_p C_c}(w-w_p) \quad (3.4\text{-}3)$$

Note, that interception and inertial impaction play negligible roles in capturing very small particles. On the other hand, for particles larger than 500 nm at normal temperatures and pressures, Brownian diffusion is practically non-existent, and collection efficiency is due solely to interception and inertial impaction. In this work, we consider Brownian diffusion for particles up to 500 nm in diameter.

As discussed in Chapter 2, standard Discrete Phase Model (DPM) in the ANSYS code treats the particles as point masses. We have, therefore, developed a UDF that modifies ANSYS's standard DPM to include the particle deposition via interception. We did not include the Brownian forces in our Lagrangian trajectory calculation, as the effect of Brownian diffusion in the ANSYS environment can be calculated more accurately by using the aforementioned Eulerian method. Our filter geometries were meshed with triangular cells ranging in number from 7,000,000 to 8,000,000. This was obtained by considering about 50 grid points around the circular perimeter of a fiber.

3.3 Analytical Expressions for Filter Performance

Kuwabara (1959) was the first to develop a mathematical theory (cell model) for predicting performance of fibrous filters with an ordered 2-D cell model. A filter's pressure drop depends on the air viscosity, filter thickness, flow face velocity (here 0.1m/s unless otherwise stated), fiber diameter, and SVF, as mentioned in Equation 1.7. The correlation of Davies (1973), on the other hand, is proven to be accurate for media with random layered media (planar) - media with almost zero through-plane and random in-plane fiber

orientations (see Equation 1.11). For the case of collection efficiency predictions due to mechanical capturing mechanisms, we used Equation 2.26 for collection due to Brownian diffusion, with $Kn = 0$. To predict interception efficiency, we used Equation 1.30 and for the inertial impactions capture prediction, Equation 1.32 has been applied. Note that slip boundary condition is neglected due the fibrous size ($d_f = 10\,\mu m$) consideration in this part of the study.

3.4 Results and Discussions

In this section, we present the results of our 3-D numerical simulations. The results presented here are aimed at studying the effect of in-plane and through-plane fiber orientation on pressure drop and collection efficiency of fibrous media.

3.4.1 Influence of In-Plane Fiber Orientation

To study the influence of fibers' in-plane orientation on the performance of a fibrous filtration medium, we developed a series of 3-D fibrous geometries with zero through-plane fiber orientations (random layered media). The in-plane fiber orientation in these media was varied from zero to 45 degrees. The SVF and fiber diameter of these media were fixed at 7.5% and 10 μm, respectively (see Figure 3.2a-c).

Results of our CFD simulations conducted using these micro-structures are shown in Figure 3.4a, where particle collection efficiency is plotted versus particle diameter. We chose an SVF of 7.5% for the simulations presented here, as it is more or less close to the

SVF of most fibrous media used in air filtration. From Figure 3.4, it can be seen that the in-plane fiber orientation distribution shows little or no influence on capture efficiency of submicron particles (i.e., 50nm to 1µm, which is the most practical range of particles of concern in aerosol filtration). For larger particles, however, our results indicate that the role of fibers' in-plane fiber orientation becomes important. Collection efficiency of large particles (3 to 5 µm) is shown in a separate figure for better comparison. It can be seen that collection efficiency increases with increasing the fibers' directionality.

It is worth noting that while the collection efficiency increases as a result of a decrease in the fibers' in-plane orientation, pressure drop seems to remain almost unaffected (see Table 3.1). This indicates that performance of a filter can be improved by changing the in-plane orientation of the fibers, if the particles sizes are comparable relative to the fibers size.

To further illustrate the influence of in-plane fiber orientation, we show our unidirectional media in Figure 3.5. Here, the in-plane and through-plane fiber orientations are set equal to zero. As can be seen in Table 3.1, the calculated pressure drops are between the pressure drop values obtained from the Kuwabara cell model (ordered 2-D model) and Davies' empirical correlation. Producing such media for filtration applications, of course, is not practical, and we included them in our discussion here only for the completeness of the study. For such micro-structures, pressure drop is slightly higher than what one may obtain from a random layered medium, perhaps due to the shape of the "openings" between the

fibers. For the same reason, we also observe that collection efficiency of unidirectional media immediately increases with increasing the particle diameter beyond 1 μm (see Figure 3.4). In summary, one can conclude that the in-plane fiber orientation has no significant influence on the pressure drop or collection efficiency of common fibrous filters, having a fiber diameter of about 10 μm, when challenged with submicron aerosol particles. More generally, one can conclude that as long as the diameter of the particles is much smaller than that of the fibers (e.g., one order of magnitude), fibers' in-plane orientation has no influence on filter's performance. Obviously, if the filter is made of nanofibers, for instance, the influence of fibers' in-plane orientation is always important. In case of nanofiber filter media, collection efficiency increases by decreasing the fibers' in-plane orientation.

3.4.2 Influence of Through-Plane Fiber Orientation

To study the influence of fibers' through-plane orientation on performance of a filter medium, we developed 3-D fibrous geometries with different through-plane fiber orientations (see Figure 3.2d-f). Here we set the fibers' in-plane orientation equal to zero to better isolate the effect. Results of our CFD simulations conducted using these micro-structures are shown in Figure 3.6, where particle collection efficiency is plotted versus particle diameter at fixed SVF and fiber diameter of 7.5% and 10μm, respectively. It can be seen that nano-particle capture efficiency is almost independent of through-plane orientation of the fibers. However, for larger particles, collection efficiency decreases by increasing the fibers through-plane orientation.

In Table 3.2, we compare the pressure drop values obtained from simulations reported in Figure 3.6 for efficiency. It can be seen that pressure drop decreases with increasing through-plane fiber orientation. These results are also compared with the predictions of Davies' empirical correlation (1973). Obviously, as the experiments of Davies were conducted using flat sheet media, his correlation is accurate only for media with negligible through-plane orientations.

It is well known that increasing collection efficiency of a filter often comes at the cost of additional pressure drops. As mentioned before, collection efficiency of a fibrous medium decreases by increasing the fibers' through-plane orientation (especially for larger particles). This, however, is associated with a decrease in the medium's pressure drop. To judge if such a modification can help to produce better media, Figure of Merit (FOM, also referred to as Quality Factor) has been defined (see Equation 2.6). Figures 3.7a–c show the FOM of the media discussed in Figures 3.4 and 3.6. Increasing the in-plane orientation of the fibers does not seem to have any clear influence on the FOM if the particles are at least an order of magnitude smaller than the fibers (see Figure 3.7a). FOM of media with different in-plane fiber orientations increases rapidly by decreasing the fibers' in-plane orientation, if the particles are comparable to fibers in size (see Figure 3.7b). It can be seen in Figure 3.7c that increasing the fibers through-plane orientation increases the FOM for nano-particles, but decreases it for larger particles (micron-size particles). This allows us to recommend media with higher through-plane fiber orientation for filtering nano-particles,

but media with random layered (planar) micro-structure (minimum through-plane orientation) for filtering larger particles.

As mentioned earlier, Banks (1987) and Banks *et al.* (1990) developed a single-fiber analytical model to study the influence of through-plane fiber orientation on pressure drop and collection efficiency. According to those authors, if a fiber's axis forms an angle θ with the air flow direction (is the complement angle of the through-plane angle discussed here), then the permeability and collection efficiency due to diffusion can be calculated in terms of θ. Recall that equations presented in section 3, are all obtained for media in which fibers are arranged perpendicular to the direction of air flow (i.e., zero through-plane angle). According to Banks (1987), the permeability of a fiber with an angle θ with respect to flow direction (complement angle of the fibers through-plane angle) is:

$$f_d^{\angle}(\theta) = (\sin^2\theta + \frac{1}{2}\cos^2\theta) f_d \qquad (3.5)$$

where $f_d^{\angle}$ denotes the dimensionless pressure drop of a medium with a non-zero through-plane fiber orientation. Banks *et al.* (1990) also proposed a single-fiber relationship for collection efficiency due to diffusion for fibers oriented with non-zero through-plane orientation:

$$E_D^{\angle}(\theta) = E_D \sin^{1/3}\theta \qquad (3.6)$$

To calculate the interception collection efficiency of fibers oriented with non-zero through-plane orientation, Schweers and Löffler (1994) adopted a single-fiber expression given as:

$$E_R^{\angle}(\theta) = E_R \frac{1+\sin(2\theta - \pi/2)}{2} \qquad (3.7)$$

These equations are used in our study to predict the collection efficiency and pressure drop of media with different through-plane fiber orientations. Note that we neglected the collection efficiency due to inertial impaction if the particles are less than 2μm.

We calculated the Figure of Merit using the above equations and added them to Figure 3.7c. It can be seen that there is good agreement between the predictions of the above semi-analytical models and our 3-D simulations.

3.4.3 Influence of Air Face Velocity

To explore whether or not the conclusions drawn so far are also valid for air filtration applications at lower and higher face velocities, we repeated our simulations of zero through-plane media with two alternatively face velocities (0.01 and 1 m/s). It was found that even a tenfold increase or decrease does not result in any specific relationship between the Figure of Merit and fibers' in-plane orientation (see Figure 3.8). For the sake of brevity, we only considered the in-plane fiber orientations of 15 and 45 degrees (SVF and fiber diameters are not varied). The results indicate that regardless of the media's face velocity, in-plane fiber orientation has no effect on the FOM for most common filters (i.e., fiber diameter around 10μm) challenged with submicron aerosol particles. As mentioned before, if the particles are comparable in size with the fibers (e.g., nanofiber media), then the fibers' in-plane orientation is no longer negligible.

For the case of media with different through-plane fiber orientations, we used the expressions of Banks and his co-workers, along with the cell model equations presented in previous subsection. Our results for face velocities of 0.01 and 1 m/s are given in Figure 3.9a and 3.9b. These results confirm that the conclusions made from Figure 3.7c are also applicable to higher and lower face velocities.

3.5 Conclusions

We solved the air flow field in the void space between fibers in a series of 3-D fibrous geometries with a fiber diameter of 10μm, SVF of 7.5% (a value close to that of most common aerosol filters), and different in-plane and through-plane orientations. Extreme care was taken to isolate the effect of fiber orientation from other parameters without restricting the randomness of fiber positions. We studied the influence of fibers' in-plane and through-plane orientations on the pressure drop and capture efficiency of fibrous media when challenged with submicron aerosol particles. Our results indicate that pressure drop and submicron particle capture efficiency of a fibrous medium are independent of the in-plane orientation of its fibers, but decrease when increasing the fibers' through-plane orientation. Calculating media's Figure of Merit, we found that increasing the fibers' through-plane orientation improves the performance of a filter medium when challenged with nano-particle aerosols. The trend, however, reverses if the particles are large.

It was also shown that fibers' in-plane orientation becomes important when the size of the particles is comparable to that of the fibers. For fibers with a diameter of 10μm, the

influence of fibers' in-plane orientation can be observed when the particles are greater than 1 μm. This brings us to the conclusion that the fibers' in-plane orientation is important even for submicron particles, if the media is made of nanofibers.

Table 3.1: Pressure drop per thickness (kPa/m) of media with different in-plane fiber orientations. Fiber diameter, and SVF, and face velocity are 10 µm, 7.5%, and 0.1 m/s, respectively.

Pressure drop per thickness (kPa/m) Media with varying in-plane fiber orientations						
Kuwabara (1959)	**Angle = 0º**	**Angle = 10º**	**Angle = 15º**	**Angle = 30º**	**Angle = 45º**	**Davies (1973)**
37.6	33.1	26.9	25.9	26.1	23.6	25.9
N/A	Std. Dev. = 4.57	Std. Dev. = 3.5	Std. Dev. = 1.15	Std. Dev. = 1.77	Std. Dev. = 0.27	N/A

Table 3.2: Pressure drop per thickness (kPa/m) of media with different through-plane fiber orientations. Fiber diameter, and SVF, and face velocity are 10 µm, 7.5%, and 0.1 m/s, respectively.

Pressure drop per thickness (kPa/m) Media with varying through-plane fiber orientations				
Davies (1973)	**Angle = 0º**	**Angle = 15º**	**Angle = 30º**	**Angle = 45º**
25.9	33.1	31.4	18.1	16.9
N/A	Std. Dev. = 4.57	Std. Dev. = 1.61	Std. Dev. = 0.84	Std. Dev. = 0.87

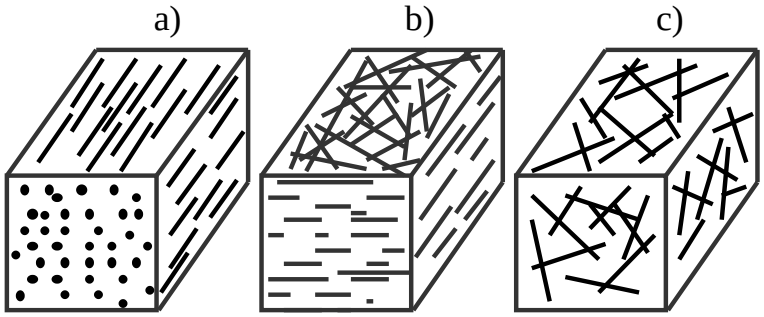

Figure 3.1: Fibrous structures (a) Parallel (b) Layered (c) 3-D random arrangement

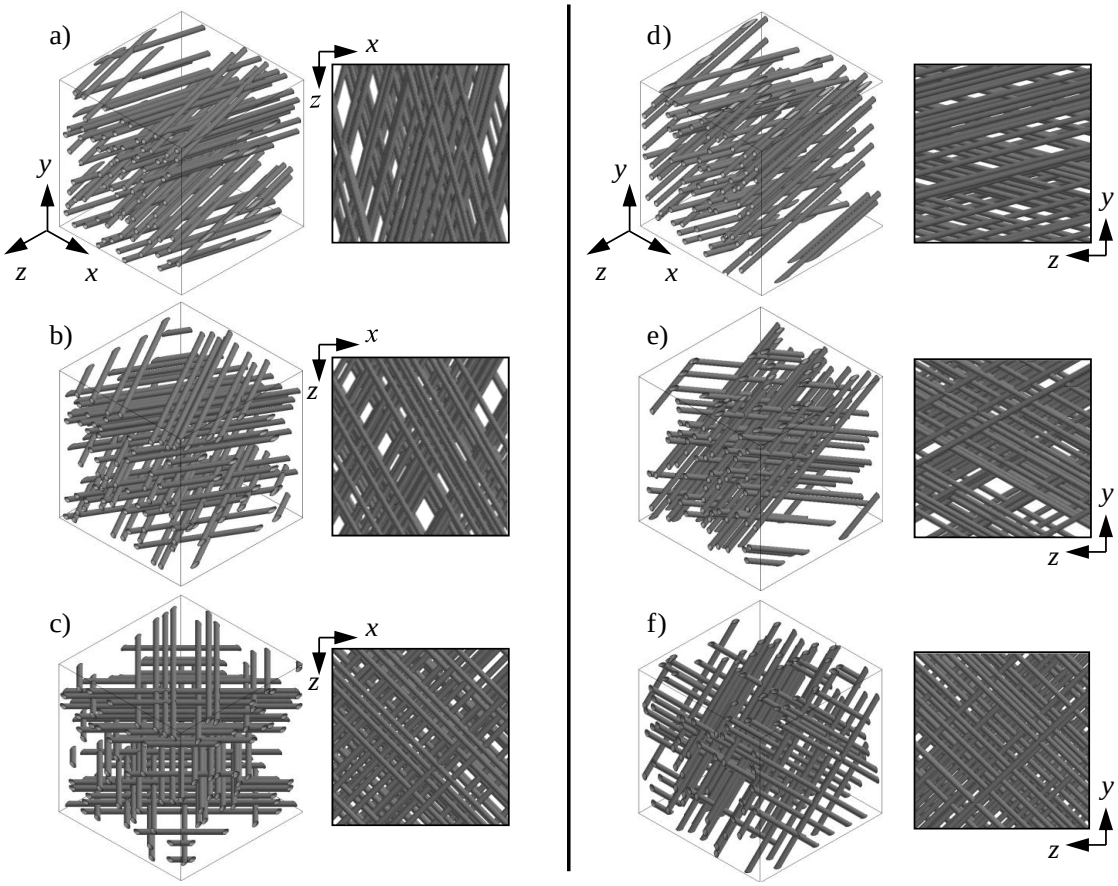

Figure 3.2: Three-D fibrous structures with (a) 15^{o} (b) 30^{o} (c) 45^{o} in-plane and (d) 15^{o} (e) 30^{o} (f) 45^{o} through-plane fiber orientations

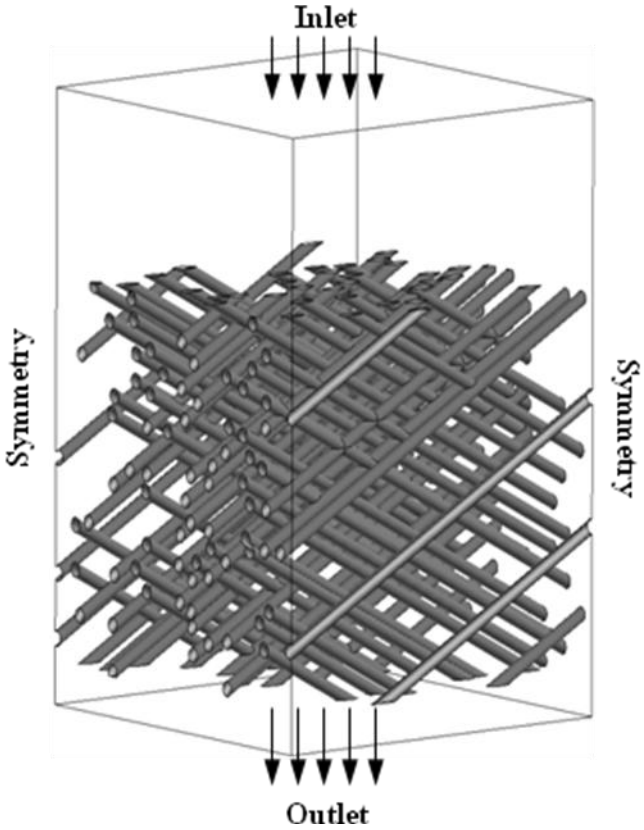

Figure 3.3: An example of the computational domains considered in this work along with the boundary conditions.

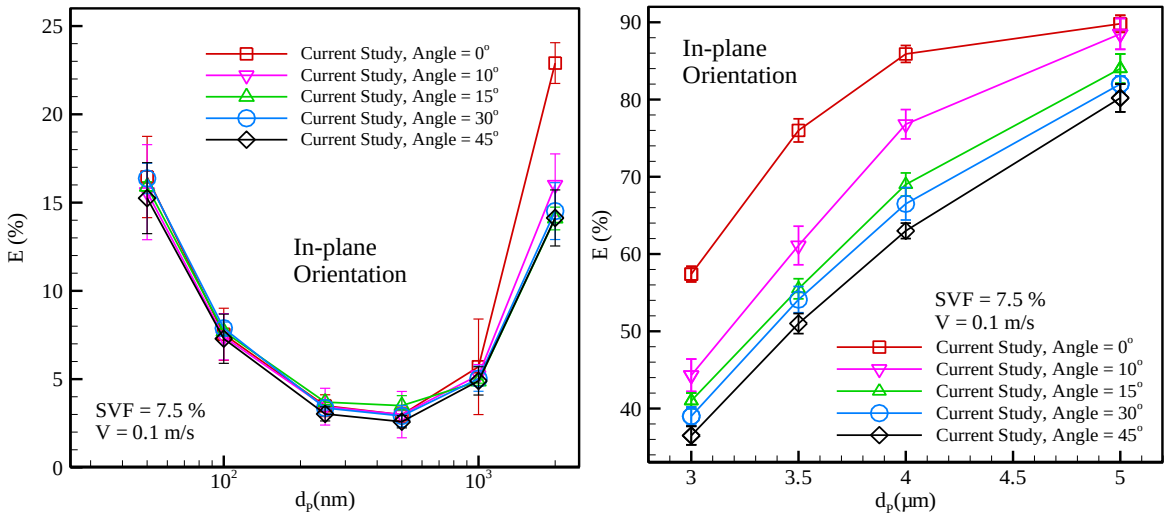

Figure 3.4: Effects of fibers' in-plane orientation on the collection efficiency of media with zero Through-plane orientation for (a) nano particles, (b) micron-size particles.

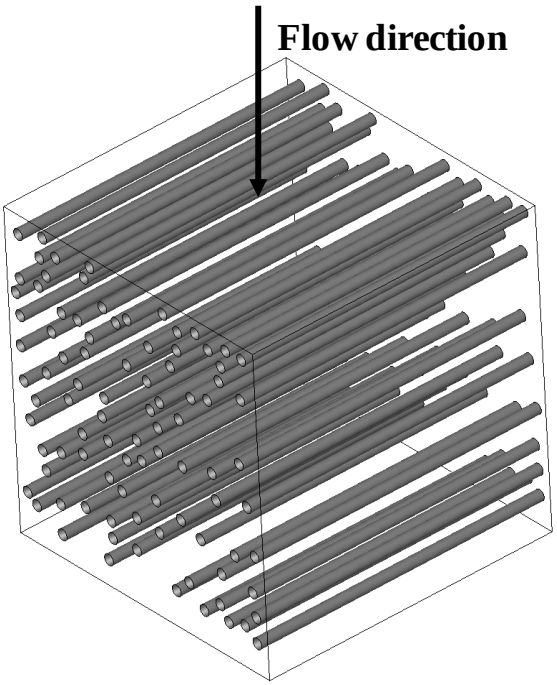

Figure 3.5: An example of unidirectional fibrous strictures (flow perpendicular to the fibers axis)

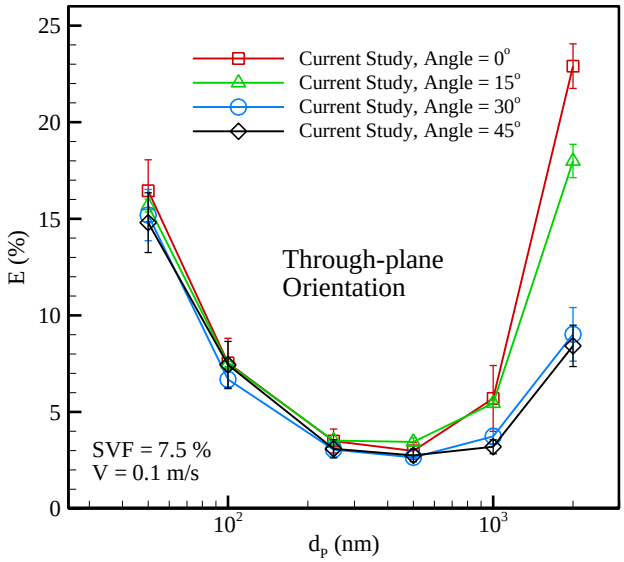

Figure 3.6: Effects of fibers' through-plane orientation on the particle collection efficiency of media with zero in-plane fiber orientation.

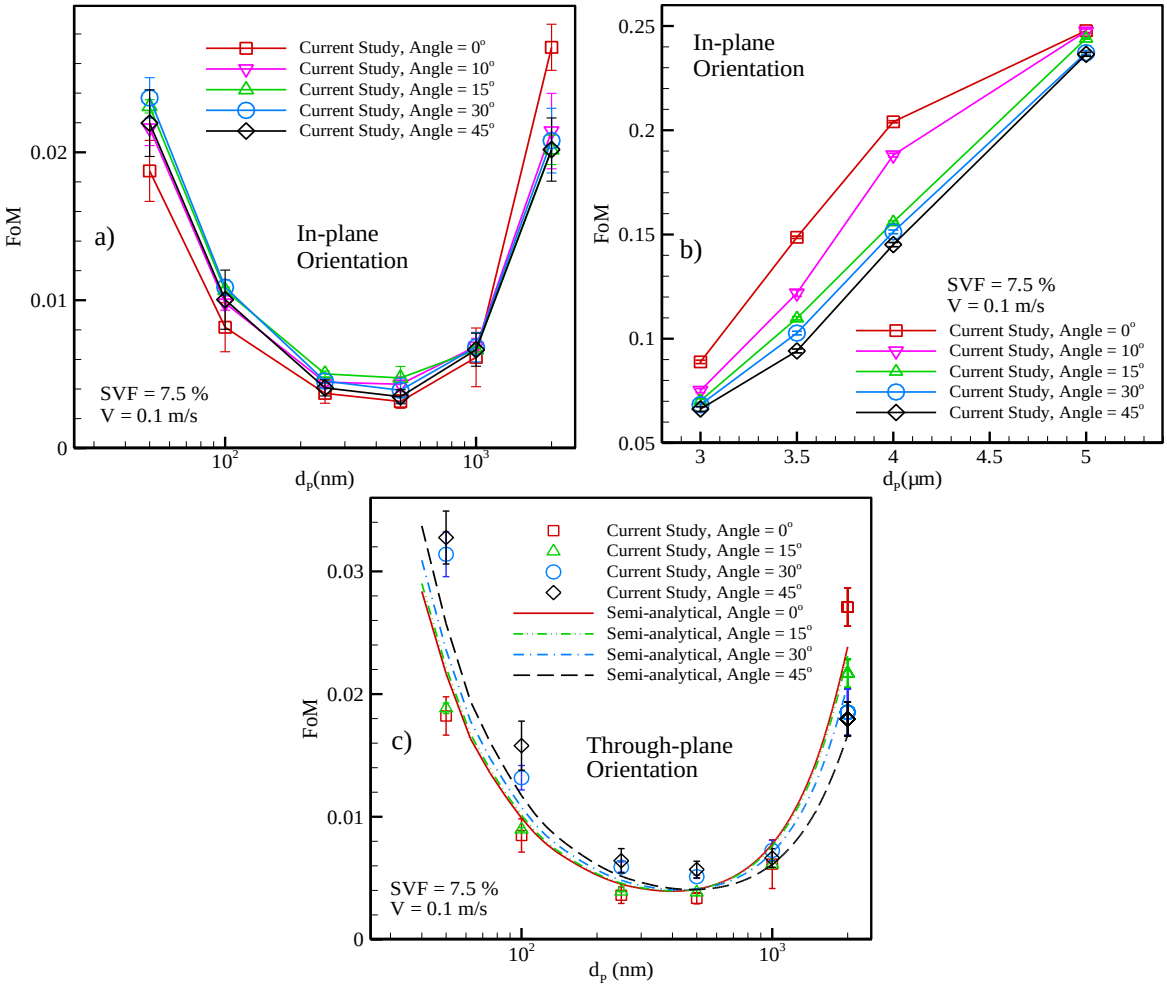

Figure 3.7: Figure of Merit (FOM) of media with different in-plane (a & b) and through-plane (c) fiber orientations. Fiber diameter, and SVF, and face velocity are 10 μm, 7.5%, and 0.1 m/s, respectively.

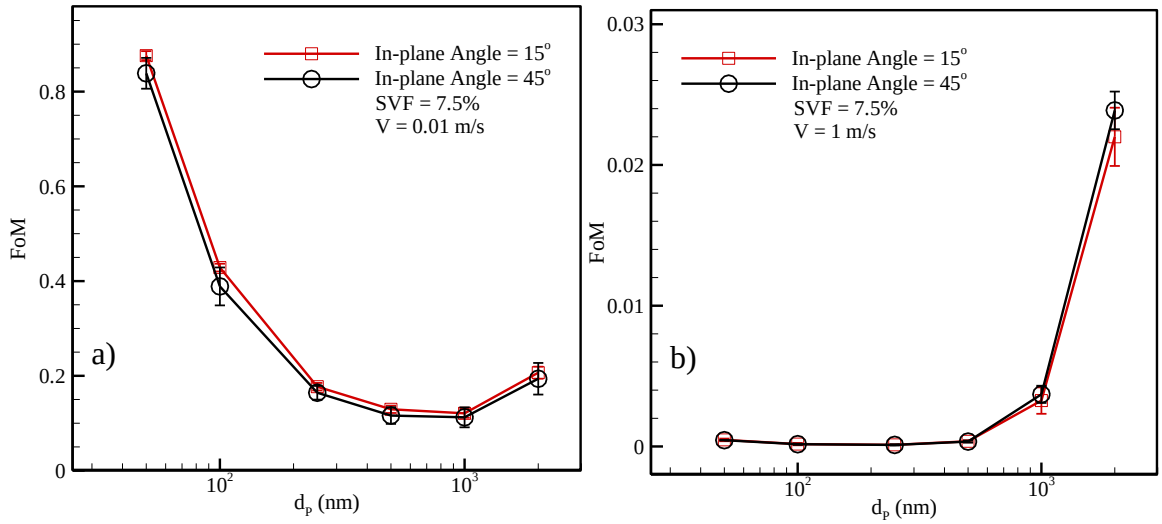

Figure 3.8: Figure of Merit (FOM) of media with different in-plane fiber orientations, at two different face velocities of 0.01 and 1 m/s, respectively.

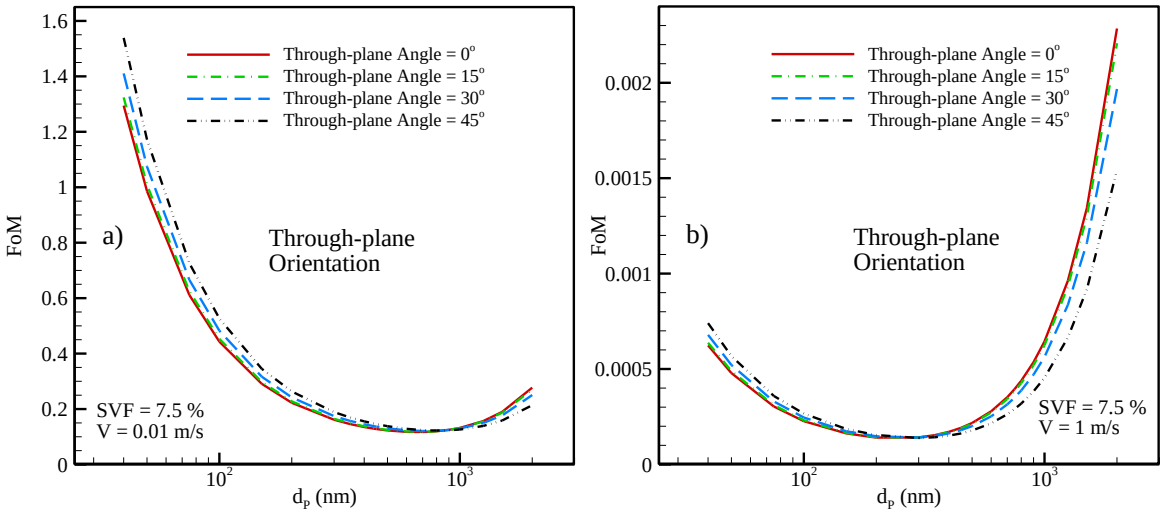

Figure 3.9: Figure of Merit (FOM) of media with different through-plane fiber orientations, at two different face velocities of 0.01 and 1 m/s, respectively. Fiber diameter and SVF are 10 µm and 7.5%, respectively.

CHAPTER 4 Micro-Scale Modeling of Media Made of Multi-Lobal Fibers[♣]

4.1 Introduction

Fibers with trilobal cross-sections are currently used for air and water filtration in variety of applications (Watanabe *et al*. 2009, Lamb and Costanza, 1980, Sanchez *et al*., 2007). An example of such media is a family of Spun-bonded Polyester fibers produced by BBA Fiberweb and sold under the brand name REEMAY. Since the infancy of filtration theory, about fifty years ago, fibers have been assumed to have circular cross-sections. There are many analytical, numerical, and empirical correlations available for predicting the collection efficiency and pressure drop of fibrous media made of fibers with circular cross-sections (referred to as circular media here for brevity). Our extensive literature search resulted only in a very few studies reporting filtration performance of media with trilobal fibers (referred to as trilobal media here for brevity). This includes the experimental studies of Lamb and Costanze (1980), and Sanches et al. (2007), as well as the numerical simulations of Raynor and Kim (2004). To the knowledge of the authors, however, no analytical expressions have yet been proposed for predicting performance of filters with trilobal fibers. Our objective in this part of the study is to establish simple analytical

[♣] *Contents of this section have been published in an article entitled "Analytical Expressions for Predicting Performance of Aerosol Filtration Media Made up of Trilobal Fibers" by S. Fotovati, H. Vahedi Tafreshi, B. Pourdeyhimi, Journal of Hazardous Materials, 186 (2-3), 1503–1512, 2011.*

expressions that allow investigators predict collection efficiency and pressured drop of their trilobal fibrous filters. We will also discuss and compare performance of filters made of trilobal fibers with their equivalent media made of circular fibers. In particular, we conduct a series of computational fluid dynamics (CFD) simulations to determine an equivalent circular fiber diameter, thereby take advantage of the existing expressions developed in the past for filters with circular fibers.

In this chapter, analytical expressions will be used for filter performance predictions and also validation purposes. For the case of pressure drop, we will use the work of Drummond & Tahir (1984), as it has been introduced in Table 1.1a by Equation 1.18. In addition, to predict collection efficiency, Equation 1.22 is used for capture due to Brownian motion. For the cases of interception and inertial impaction Equations 1.30 and 1.31are implemented, respectively.

4.2 Equivalent Circular Fiber Diameter for Trilobal Fibers

Expressions given in Chapter 1 are defined for medium with circular fibers. There are no such relationships for trilobal media; trial-and-error has been the only possible method for developing trilobal media. A widely accepted, but not documented, notion among the practitioners has been to consider an equivalent circular fiber that has the same cross-sectional area as the trilobal fibers, and use it in the equations given in Chapter 1. Our objective here is to firstly determine whether or not such an area-based equivalent fiber diameter definition is accurate, and if not, propose an alternative definition.

Figure 4.1a shows an example of a fibrous filter with trilobal fibers used for particle filtration. Trilobal fibers are often produced by forcing a polymer through Y- shaped slots (Xue *et al*., 2005) and the final geometry of the fiber does not have a specific mathematical descriptions. Therefore, we approximated these geometries with three overlapping ellipses (see Figure 4.1b). To generate a trilobal cross-section, we rotated an ellipse about its antipodal point by 120 and 240 degrees and united the resulting ellipses with one another. Considering an ellipse along the x-axis, we have:

$$b^2(x-x_0)^2 + a^2y^2 = a^2b^2 \qquad (4.1)$$

where a and b are lengths of the ellipse's major and minor axes, respectively, $x_0 = e.a$ is the x-coordinate of the ellipse's center, and $e^2 = 1-(b/a)^2$ is its eccentricity. After a θ-degree rotation about the left antipodal point, we obtain:

$$b^2(x\cos\theta - x_0 + y\sin\theta)^2 + a^2(y\cos\theta - x\sin\theta)^2 = a^2b^2 \qquad (4.2)$$

It is now easy to find the coordinates of the intersection points between the above ellipses and use them to calculate the perimeter of the trilobal cross-section. For the perimeter calculations, we represent the original ellipse in parametric form, i.e., $\vec{r}(\theta) = a\cos\theta, b\sin\theta$ and calculated the length of the arc from point D to point A (corresponding to θ_D and θ_A, respectively). The perimeter, p, of the trilobal geometry is then:

$$p = 6\int_{\theta_D}^{\theta_A} \sqrt{\vec{r}'(\theta)\cdot\vec{r}'(\theta)}\, d\theta \qquad (4.3)$$

where $\vec{r}'(\theta) = d\vec{r} / d\theta$. To find the surface area of the trilobal cross-sections, we considered the original ellipse and calculated the surface area under the arc from point *D* to point *A* (corresponding to x_D and x_A, respectively). Therefore,

$$s - s_t = 6\int_{x_D}^{x_A} b\sqrt{1-(x-x_0)^2/a^2}\,dx \qquad (4.4)$$

where s and s_t are the surface area of the trilobal cross-sections and the triangular area formed between the three intersection points (shown in grey in Figure 4.1b), respectively. Knowing the coordinates of the intersection points *A*, *B*, and *C*, the surface area of this equilateral triangle can easily be calculated:

$$s_t = 1/2\,sin\pi/3\;(x_A - x_B)^2 + (y_A - y_B)^2 \qquad (4.5)$$

Knowing s and p, we can then define equivalent circular geometries having identical areas or perimeters as the trilobal cross-sections and determine the accuracy of such equivalent diameter definitions in predicting pressure drop and collection efficiency of trilobal media. Here, we also define an equivalent diameter based on the trilobal cross-section's circumscribed circle and used it in performance prediction.

Figure 4.2 compares equivalent circular diameters obtained for trilobal cross-sections having different size and aspect ratios ($\zeta = a/b$). These calculations indicate that equivalent diameters based on the perimeter and circumscribed circle are almost identical. Therefore, we only use circumscribed circles in the rest of this chapter and compare them with the area-based diameter definition.

4.3 CFD Simulations

The governing equations are the same as what we presented in third section of Chapter 2. To generate 2-D random fibrous geometries, a FORTRAN computer program is developed to produce fibrous structures of different porosities and thicknesses. The media generation process is explained in the flow chart shown in Figure 4.3. Trilobal fibers are treated as circles with a diameter equal to that of their circumscribed circle and randomly placed in a square domain. The media generation starts by sequentially adding the fibers into a square domain with a size obtained from SVF and the number of fibers considered for the simulations. Distance between a new fiber and the existing ones are continuously monitored to avoid fiber-fiber overlaps. Moreover, to ensure that a high-quality mesh can be generated inside the domain, fibers were not permitted to touch one another. Therefore, a minimum gap of $1.2d_{cc}$ was enforced between the fibers' center-to-center distance (d_{cc} is the diameter of the circumscribed circle). Note that this is just a simplification considered in this study, as the fibers do touch one another in a real filter medium. However, the impact of crossover points (fiber-to-fiber contact points) on the pressure drop and collection efficiency of a filter medium is quite negligible at porosities as high as those considered in this part of the study (more than 90%) and in the absence of particle caking. At the end of the media generation process, the geometry is exported to Gambit software (a preprocessor for ANSYS CFD code) via a script file for meshing. The mesh files were then exported to ANSYS for finite volume calculations. Figure 4.4 shows an example of a 2-D random fibrous medium with a thickness of 380μm and a SVF of 10% consisting of 300 trilobal fibers having a minor axis of 2μm, and an aspect ratio of 1.5. Simulation boundary

conditions are shown in Figure 4.4. Uniform velocity and concentration profiles are assumed for the incoming airborne particles at the inlet. It is assumed here that particles that come in contact with the fibers will be captured and vanished from the solution domain. Note that the inlet and outlet boundaries are placed far up and downstream, so that a uniform flow can be assumed to prevail at the inlet and outlet. We used an upstream distance of $L = 35(a+b)$ for our small particle (Eulerian) and large particle (Lagrangian) flow simulations, respectively, to improve the calculation's accuracy. Our outlet boundary is placed at a distance of $4\ a+b$ downstream of the filter. We did not observe any significant errors caused by the above $4\ a+b$ distance. However, it is advisable to place such zero-streamwise gradient boundaries far downstream of the filter to ensure that the simulations converge to accurate values.

As the fibers are randomly distributed in the simulation domain, it is always necessary to repeat each simulation a number of times and average the results. It is also important to ensure that the domain size considered for the simulations is large enough so that the results are not affected by any size-related artifact. The larger the domain size, the fewer the number of required repetitions for smoothing out the statistical fluctuation of the results. In this study, we considered 300 fibers in our simulations domains and repeated each simulation 3 to 5 times.

Symmetry boundary conditions are considered for the upper and lower boundaries of the domain, i.e., the gradient of flow properties (velocity, particle concentration …) is zero at these boundaries. The general problem with symmetry boundary condition is that it does not allow lateral flow to take place. However, for large simulation domains, like those considered here, this should not be a concern as the net flow in the lateral directions will average to zero.

Standard Discrete Phase Model (DPM) in the ANSYS code ignores the dimensions of the particle during trajectory tracking. Collision between a particle and a wall boundary is considered to be the moment that the particle center of mass touches the wall boundary, which obviously is not realistic. In this work, we developed a UDF to instruct ANSYS to stop the particle if it comes in one radius distance from the wall boundary, as mentioned previously. This has been done by continuously monitoring the distance between the particles' centers and fibers' surface during the trajectory tracking. If the particle's center of mass reaches a distance of away from a fiber, it will be counted as deposited. Note that for the Lagrangian particle tracking, symmetry boundary conditions act like a perfectly reflecting wall, i.e., particles colliding with the symmetry boundaries will be reflected without any loss of momentum.

Figure 4.5a shows the particle concentration contour plot throughout the domain for a typical trilobal medium considered in this work. Red to blue represents normalized nano-particle concentration from 1 to zero. Figure 4.5b depicts the trajectory of particles' centers

of mass for 0.5μm particles in the same solution domain. For the sake of clarity, only a few particle trajectories are shown. Our filter geometries were meshed with triangular cells in the filter zone and quadrilateral cells in the fluid entry zones. Depending on the fiber aspect ratio, 3,000,000 to 7,000,000 cells were used in the simulations presented in this section. Larger numbers of cells are considered in simulations with greater aspect ratios to correctly resolve the flow field at shaper corners of high aspect ratio fibers. To find out the minimum number of mesh points needed to conduct mesh-independent simulations, a single trilobal fiber was placed in the middle of a square 2-D domain. The sides of the square were chosen such an SVF of 10% was achieved (see Figure 4.6). The pressure drop caused by this single fiber was monitored as the number of mesh points per each lobe of the fiber was increase from 10 to 100. It can be seen that grid density has negligible effect on the pressure drop prediction for more than 80 grids per lobe.

To correctly predict the particle capture efficiency via interception and impaction, one must release a large number of particles in the flow domain to ensure that the results are independent of number of particles at inlet. Figure 4.7 shows the influence of number of particles introduced at the inlet on the medium's collection efficiency using the Lagrangian method (equation 2.10). The horizontal axis here is the number of particles per unit of length at the inlet (N_p / h). It can be seen that particle collection efficiency (due to interception and inertial impaction) is independent of the number density of the particles at the inlet beyond a value of about 2×10^6, and so we used this density for the particle injection at the inlet.

4.4 Results and Discussions

4.4.1 Performance of 2-D Micro-Structure

As mentioned before, despite their wide spread applications, trilobal media have not been systematically studied in the literature. Unfortunately, there are no reliable experimental studies available in the literature that could be used here for our model validation. Therefore, we validate our simulation methodology by presenting a comparison between results of our simulations of circular media with the predictions of some of the available empirical/semi-empirical models that have been developed for media with circular fibers (see Section 4.1). Figure 4.8 shows penetration per thickness through filter media with a SVF of 10% made up of circular fibers with a diameter of 14.9 μm along with the predictions of the expressions developed by Stechkina and Fucks (1966) and Lee and Liu (1982). Good agreement between our modeling results and these empirical correlations is evident especially for particles greater than 200 nm. In this figure, we also included our simulation results obtained for trilobal media with fibers having an aspect ratio of $\zeta = 2$ and a minor axis of $b = 2$ μm (resulting in a circumscribed diameter of 14.9 9 μm).

The idea of using the circumscribed circle was inspired by the fact that the flow inside a fibrous medium is highly viscous ($\mathrm{Re} < 1$) (i.e., Stokes flow regime), and the presence of an obstacle (whether trilobal or circular) is sensed by the fluid particles (as well as the solid nano-particles) far upstream of the fiber (see Figure 4.9). Therefore, streamlines are deflected far before they are close to the fiber. Deflection of the streamlines is mostly caused by the projected area of the fibers on a plane normal to the flow direction, rather

than the exact shape of the fiber cross-section, and so is not very sensitive to the height or width of the lobes (note that the inertial effects are negligible for submicron particles, and they tend to follow their streamlines). Therefore, a fiber's collection efficiency is also not very sensitive to the lobe's geometry as the air in the grooves between the lobes seems to remain almost motionless, i.e., acting like a solid object against the flow.

Figure 4.10a–c show influence of the fiber's aspect ratio on penetration per thickness, $Ln(P)/t$ through trilobal media with a SVF of 10%. It can be seen that filters' penetration per thickness (for the range of particles considered) increases by increasing aspect ratio. Note that minor diameter of the fibers' elliptical lobes is kept constant (2μm) in the simulations reported in this section. Unlike the experimental work of Lamb and Costanza (1980), the fibers' cross-sectional area is not kept constant in our study.

In Figure 4.10d–f, one can see that penetration per thickness decreases by increasing the SVF, as expected. It can also be seen that there is good agreement between the results generated with circular fibers having a diameter obtained by using the trilobals' circumscribed diameter. In this figure, we also added the predictions obtained by using the aforementioned area-based equivalent circular diameters. It can be seen that the area-based equivalent diameter tend to overestimate particle penetration through the media, while the definition based on the circumscribed circle closely agree with the direct simulations of trilobal media.

The results shown in Figure 4.10 indicate that diameter of the circumscribed circle of a trilobal fiber can effectively be used to predict collection efficiency of trilobal filters. It should be noted, however, that using this diameter, SVF of the media increases drastically. The new SVF helps achieving good predictions for collection efficiency; however, it results in wrong pressure drop estimates. To solve this problem, we simulated series of trilobal single fibers in domains similar to the one shown in Figure 4.6, and calculated the their pressure drops for different SVFs of 5, 6, 7.5, 9 and 10 percent and different aspect ratios of 1.5, 2, 2.5 and 3. These simulations were then repeated for the circumscribed equivalent fiber of each trilobal fiber for comparison purposes (see Figure 4.11). In this figure, each line represents the relationship between pressure drop per thickness of trilobal filters and their equivalent circumscribed media. Figure 4.11 can be used to predict the pressure drop of a trilobal medium, $\Delta p/t_{tri}$, using the pressure drop value of its equivalent circumscribed medium, $\Delta p/t_{cc}$, obtained with equations given in section 4.1. For the sake of convenience, we also presented an equation for each line shown in Figure 4.11. Note that to calculate $\Delta p/t_{cc}$, one needs to know the SVF of the equivalent circumscribed media. Assuming K_t to be the ratio of the SVF of the equivalent medium to that of the original trilobal media, we have:

$$K_t = \alpha_{cc} / \alpha_{tri} \qquad (4.6)$$

where α_{tri} and α_{cc} are the SVF of media made of trilobal and circumscribed circles, respectively. In general, $K_t = K_t(\zeta, b)$, where $\zeta = a/b$ is the fiber aspect ratio. We calculated K_t for different values of $1 < b < 5$ micron and $1 < \zeta < 5$, and plotted the results in

Figure 4.12. It can be seen that dependence on b is quite negligible in comparison to that on the aspect ratio. This allows us to neglect the dependence on b and develop an easy expression for $K_t = K_t(\zeta)$, as follows:

$$K_t = 1.4\zeta - 0.36 \qquad (4.7)$$

This equation can be used to calculate SVF of the circumscribed circle equivalent media of each trilobal filter.

In Figure 4.13, we compare pressure drop per thickness of trilobal media and their equivalent circumscribed media as they were obtained from our CFD simulations. The media considered here have an aspect ratio of 2, a minor elliptical axis of $b = 2$ μm, and three different SVFs of 5, 7.5, and 10 percent. As explained earlier, pressure drop of the equivalent media is much higher than that of the actual trilobal filters. These pressure drop values are then corrected using the relationships given in Figure 4.11 and added to Figure 4.13. It can be seen that corrected the pressure drop values are in good agreement can be expected values. In this figure we also included the predictions of the analytical model of Drummond and Tahir (1984) for the equivalent circumscribed media. The good agreement between our simulation results and the well-known model of Drummond and Tahir (1984) validates the accuracy of the simulations.

4.4.2 Test Case: Performance of 3-D Micro-Structure

This section is intended to examine whether or not equations and conclusions obtained from our 2-D simulations are valid for real 3-D filters. In the absence of reliable experimental data, we use 3-D virtual fibrous structures, as they more realistically

represent the micro-structure of a real filter medium Three-dimensional simulations require extensive computing resources, and so are not suitable for an extensive parameter study. Here, we use 3-D simulations for validation purposes only. To do so, we generate a few 3-D fibrous media with trilobal fibers having $\zeta = a/b = 1.5$ using the Geodict code, and calculate their pressure drop and collection efficiencies. We then use our circumscribed equivalent media to predict these results. GeoDict is a voxel-based code developed by Math and Market, and is validated in many recent publications by other studies (e.g. see Schulz *et al*., 2007). To generate the trilobal-shaped fibers, Geodict software uses a special mathematical formulation for trilobal fibers as presented in Equation 4.8:

$$\begin{cases} x = r_0\ \ 1 - r_1.\sin\ \ 3\theta\ \ \cos\theta \\ y = r_0\ \ 1 - r_1.\sin\ \ 3\theta\ \ \sin\theta \end{cases} \qquad (4.8)$$

Where, r_0 and r_1 are the constant and θ varies between 0 to 360 degrees. Figure 4.14 shows three trilobal cross sections with different values of 0.95, 0.35 and 0.2 for r_1. It is obvious that using the Geodict software is not helpful if one wants to study the effects of lobes' aspect ratio. Therefore, we only picked the geometry with $r_0 = 7.8$ and the amplitude of $r_1 = 0.35$, which gives the trilobal cross section with identical cross sectional area and perimeter as our generated geometry. Our voxel size independence has revealed that consistent results can be obtained from Geodict by using 0.3 µm as the voxel size. Here, we compare the performance of trilobal media with that of their circumscribed and area-based equivalent structures (see Figure 4.15). Collection efficiencies of these media are compared with one another in Figure 4.16. It can be seen that circumscribed equivalent

media, unlike the area-based model, can be used to predict the efficiency of trilobal media with acceptable accuracy. Table 4.1 presents pressure drop per thickness of media shown in Figure 4.16. We also added the empirical correlation of Davies (1973) for comparison. It can again be seen that our circumscribed-circle-equivalent model together with its correction factor can be used to predict the pressure drop of a trilobal medium.

4.4.3 Filters with Star-Shaped Fibers

Here we considered 8-lobe star-shaped fibers. We rotated an ellipse for 45, 90, 135, 180, 225, 270 and 315 degrees around its antipodal point and result is a star-shaped fiber as it can be seen in Figure 4.17. In this figure, both area-based equivalent circle and circumscribed circle are shown. Figure 4.18 shows the effect of different aspect ratios on the performance of star-shaped fibers. In this figure different aspect ratios of 2.5, 3 and 4 with constant SVF of 10% have been considered and the results for penetration per thickness of media are presented. These results prove that the circumscribed equivalent diameter is also applicable to star-shaped fibers, as they result in good prediction for the collection efficiency of star-shaped fibers. More importantly, results of Figure 4.18 also indicate that smaller aspect ratios lead to better collection efficiencies. In Figure 4.18, we can also see a comparison between two filters with different SVFs of 5 and 10%, while the aspect ratio is kept constant at 2.5. In Figure 4.19, each line represents the relationship between pressure drop per thickness of star-shaped filters and that of their equivalent circumscribed media. Figure 4.19 can be used to predict the pressure drop of a star-shaped medium, $\Delta p/t_{star}$, using the pressure drop values of its equivalent circumscribed

medium, $\Delta p/t_{cc}$. We also obtained curve fitting equations for lines shown in Figure 4.19. Note that to calculate $\Delta p/t_{cc}$, one needs to know the SVF of the equivalent circumscribed media.

4.5 Conclusion

In this part of the study, for the first time we established a definition for an equivalent circular fiber that can be used with the traditional filtration correlations (developed for filters with circular fibers) for predicting collection efficiency of filters made of trilobal fibers. Our study was conducted in 2-D simulation domains, and due to the lack of suitable experimental data, validated via 3-D realistic simulations in which fibers random orientations were taken into account. We demonstrated that the circumscribed circle of trilobal fibers can be used with the existing traditional empirical/semi-empirical correlations to predict the performance of a trilobal filter medium. We believe that the information presented in this chapter can be used by the manufacturers to predict and optimize performance of their media, and help in reducing the experimental trials before the actual production process.

Table 4.1: Pressure drop of the media shown in Figure 4.15. Prediction of the empirical correlation of Davies (1973), obtained for media with circular fibers, is also added.

3-D SVF=10%	**Trilobal**	**Circum-scribed**	**Area-based**	**Davies (1973)**	**Eqs. in Figure 4.11**
$\Delta P_{ave.}/t$ (kPa/m)	**84.33**	**109.55**	**81.11**	**106.55**	**78**
Std. dev.	**6.67**	**16.67**	**2.78**	**-**	**-**

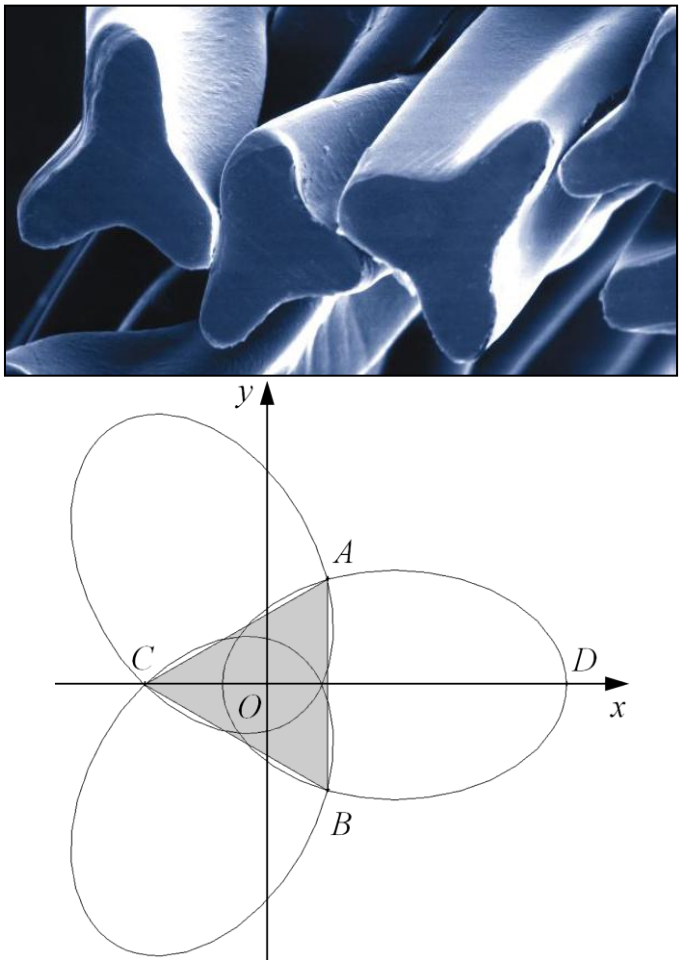

Figure 4.1: a) trilobal fiber, source: http://www.fiberwebfiltration.com/Reemay.cfm, b) overlapping ellipses forming a trilobal cross-section.

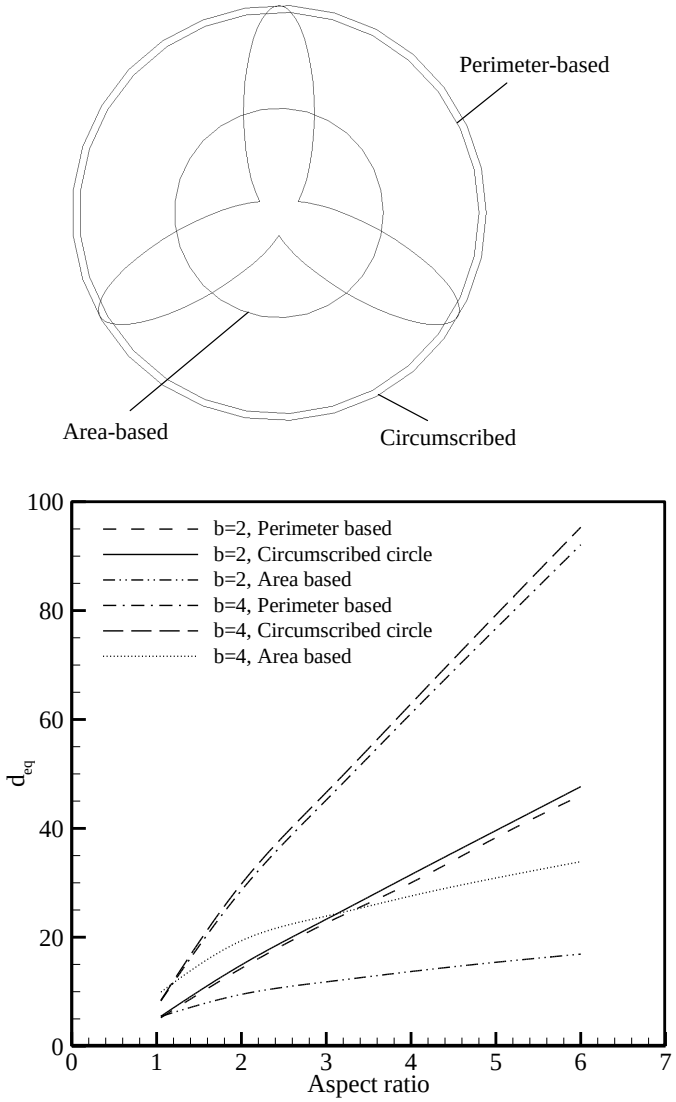

Figure 4.2: Equivalent circular diameters obtained based on equal surface area and equal perimeter are compared with the diameter of the circumscribed circle for trilobal fibers with different aspect ratios and two different minor axes of b=2 and 4 micrometer. It can be seen that equivalent diameter based on equal perimeter is very close to the diameter of the circumscribed circle.

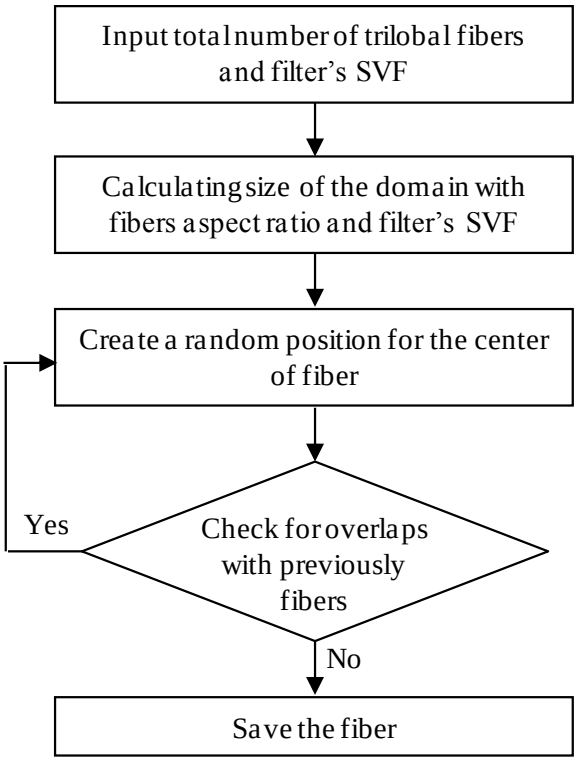

Figure 4.3: Our program's flowchart for generating media with random trilobal fibers.

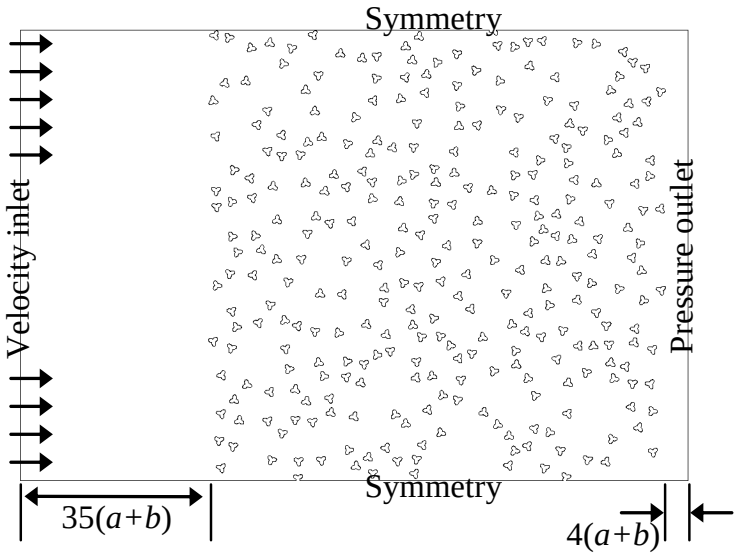

Figure 4: An example of our simulation domains consisting of 300 trilobal fibers with an aspect ratio of 1.5 randomly placed in square domain resulting in an SVF of 10%.

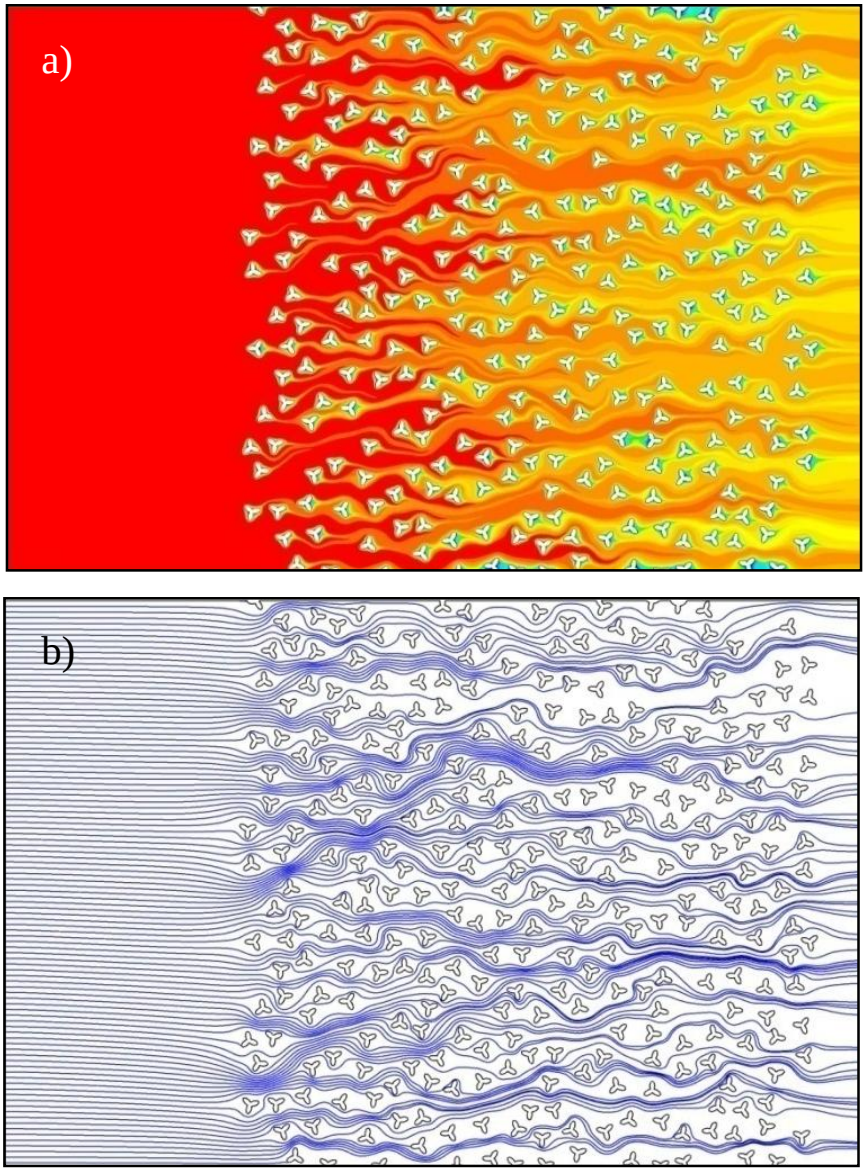

Figure 4.5: Contours of nano-particle concentration are shown in a trilobal medium with an SVF of 10% consisting of fibers with an aspect ratio of 2 (a). Few particle trajectories are shown to demonstrate particle collection due to interception (b).

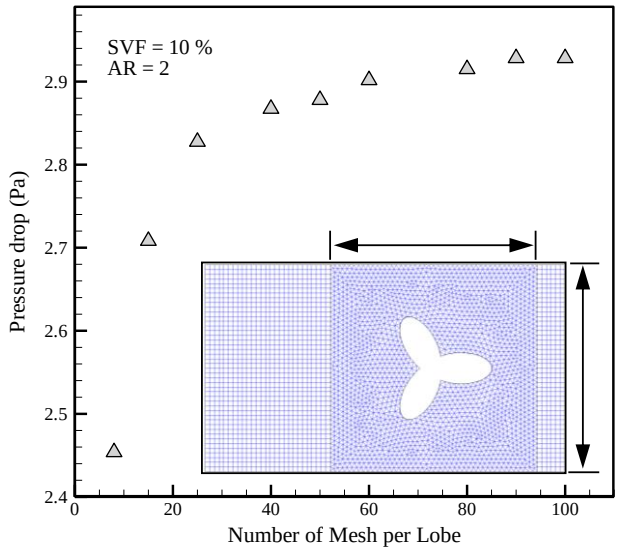

Figure 4.6: Influence of grid density on the pressure drop cause by a single fiber placed in a domain with an SVF of 10% as shown in the inset.

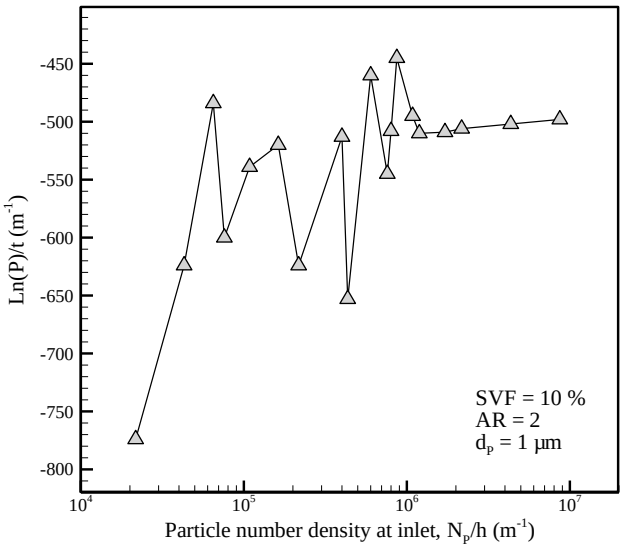

Figure 4.7: Influence of number of particles injected at the inlet on the penetration prediction of a typical trilobal media simulated in this study (SVF of 10% and aspect ratio of 2).

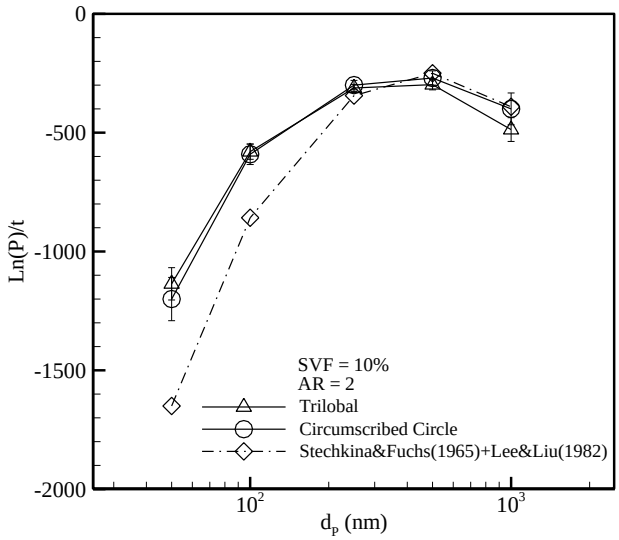

Figure 4.8: Comparison between simulation results obtained for trilobal filters with SVF of 10% and aspect ratio of 2 and their equivalent circumscribed media. Predictions of the semi-empirical expressions of Stechkina and Fuchs (1965) and Lee and Liu (1982) are added for comparison.

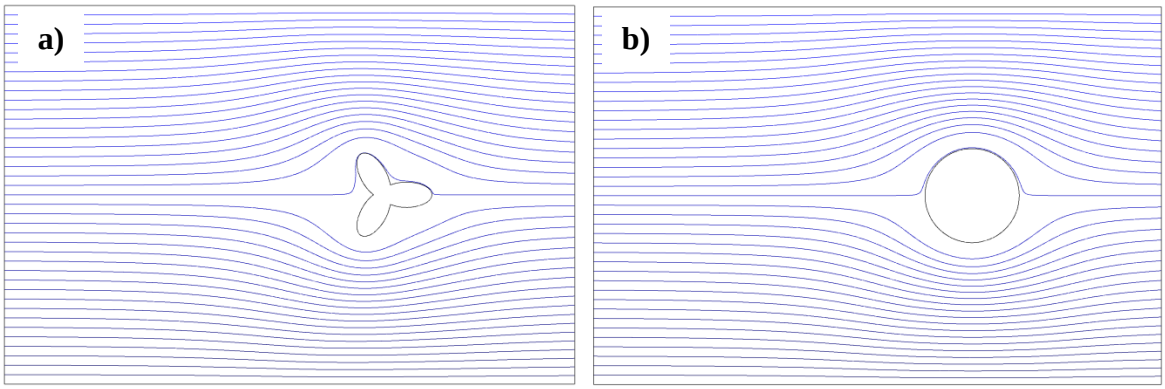

Figure 4.9: Deflection of the streamlines is mostly caused by the projected area of the fibers on a plane normal to the flow direction. It can be seen that the flow pattern around a trilobal fiber (a) and its circumscribed circle (b) are quite similar.

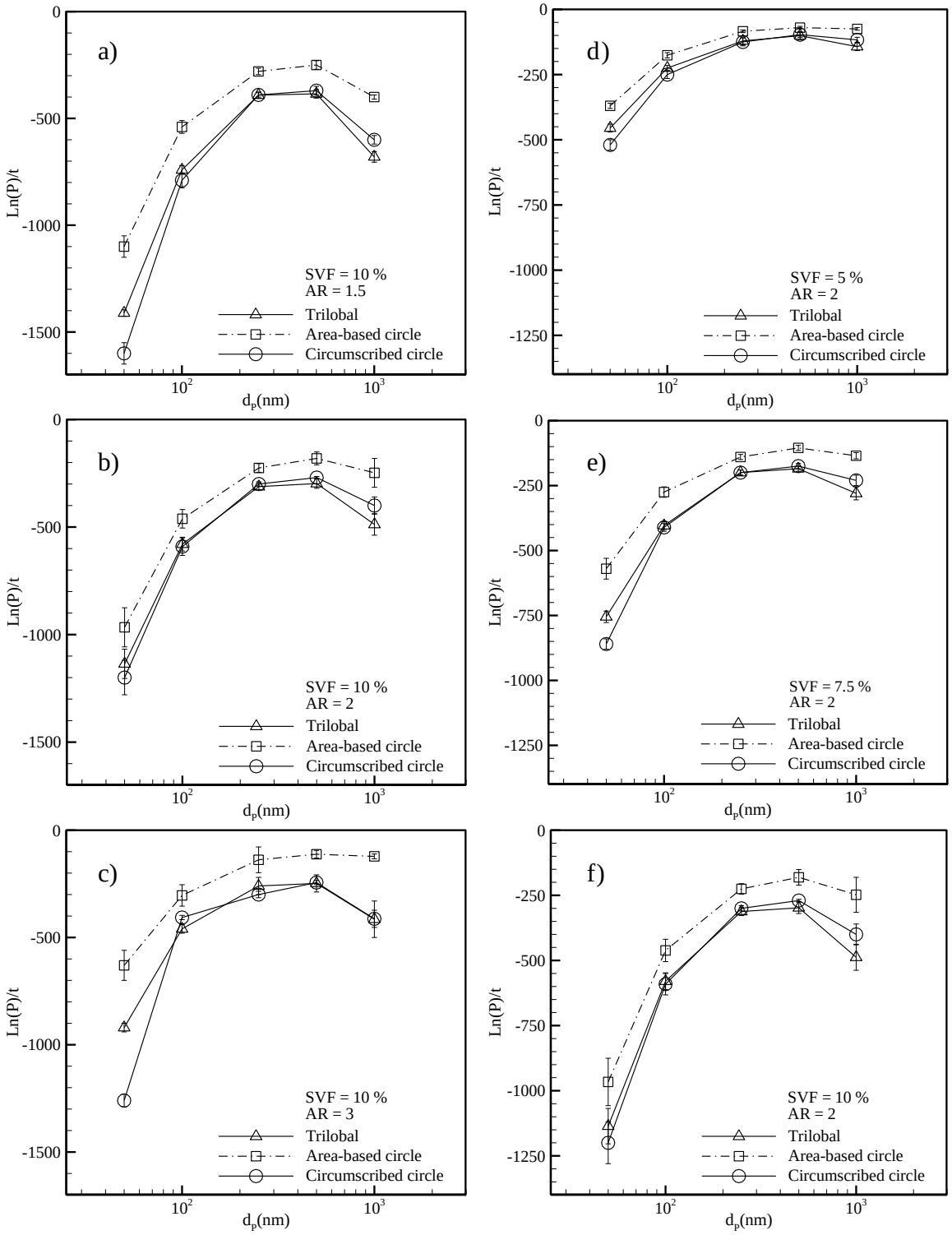

Figure 4.10: Penetration per thickness for trilobal media and their equivalent area-based and circumscribed media at a constant SVF of 10% (figures a–c), and at a constant aspect ratio of 2 (figures d–f).

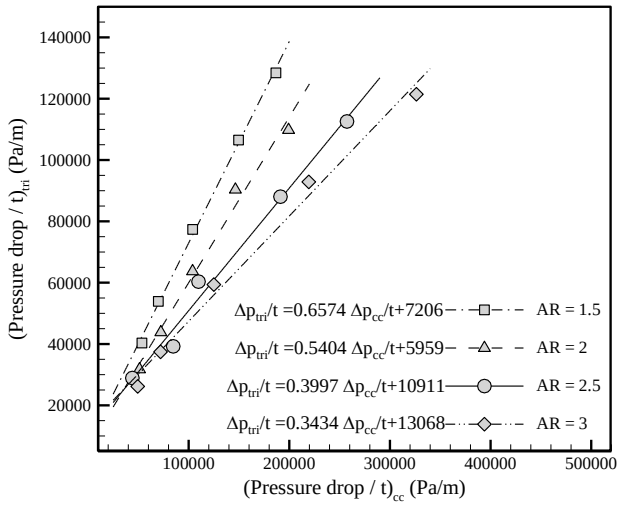

Figure 4.11: Relationship between pressure drop of trilobal media and their equivalent circumscribed equivalents for a SVF of 10% and different aspect ratios of 1.5, 2, 2.5 and 3. Curve fitting equations are given for each case for convenience.

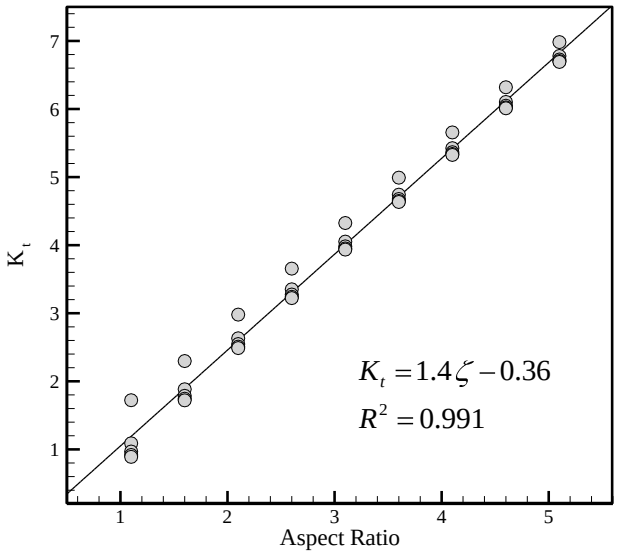

Figure 4.12: Relationship between SVF of trilobal filters with different aspect ratios and different minor axis diameter, and those of their circumscribed equivalent media.

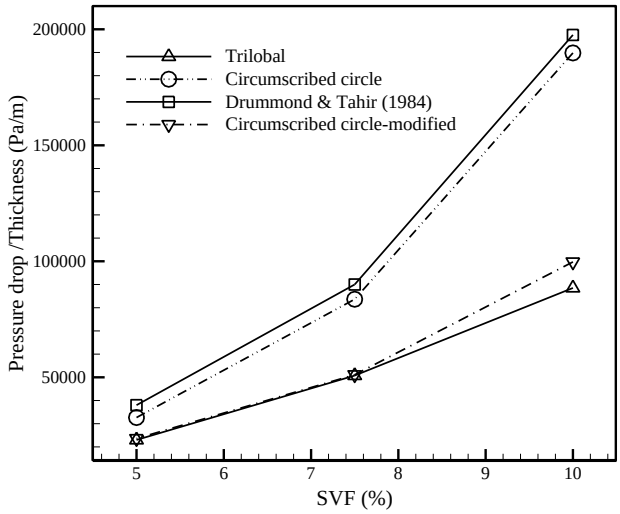

Figure 4.13: Pressure drop per thickness for trilobal filters and their circumscribed equivalent media before and after pressure correction.

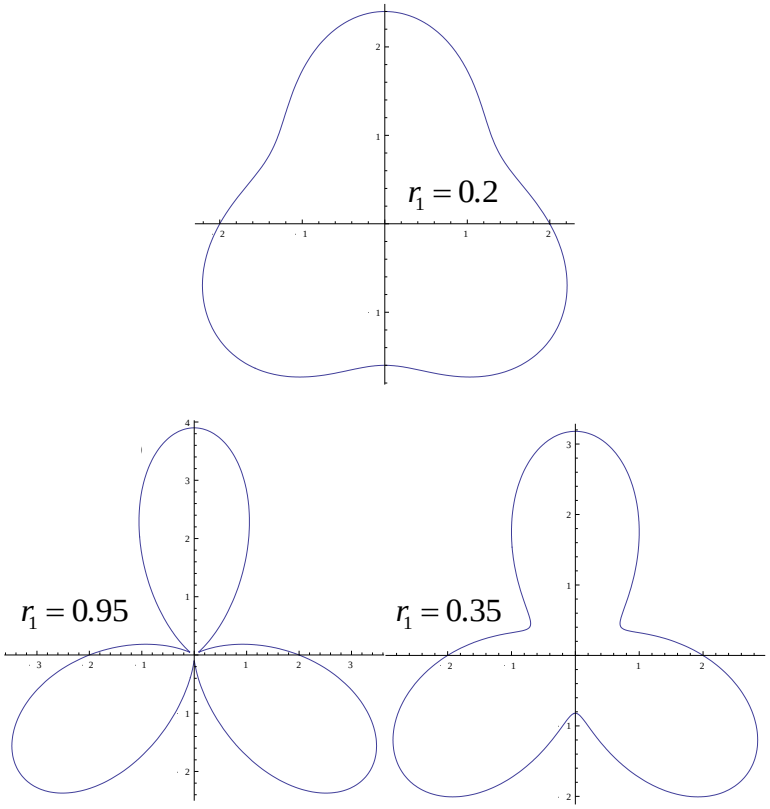

Figure 4.14: Trilobal fibers with different r_1 values created with the mathematical formulation which is used by Geodict software.

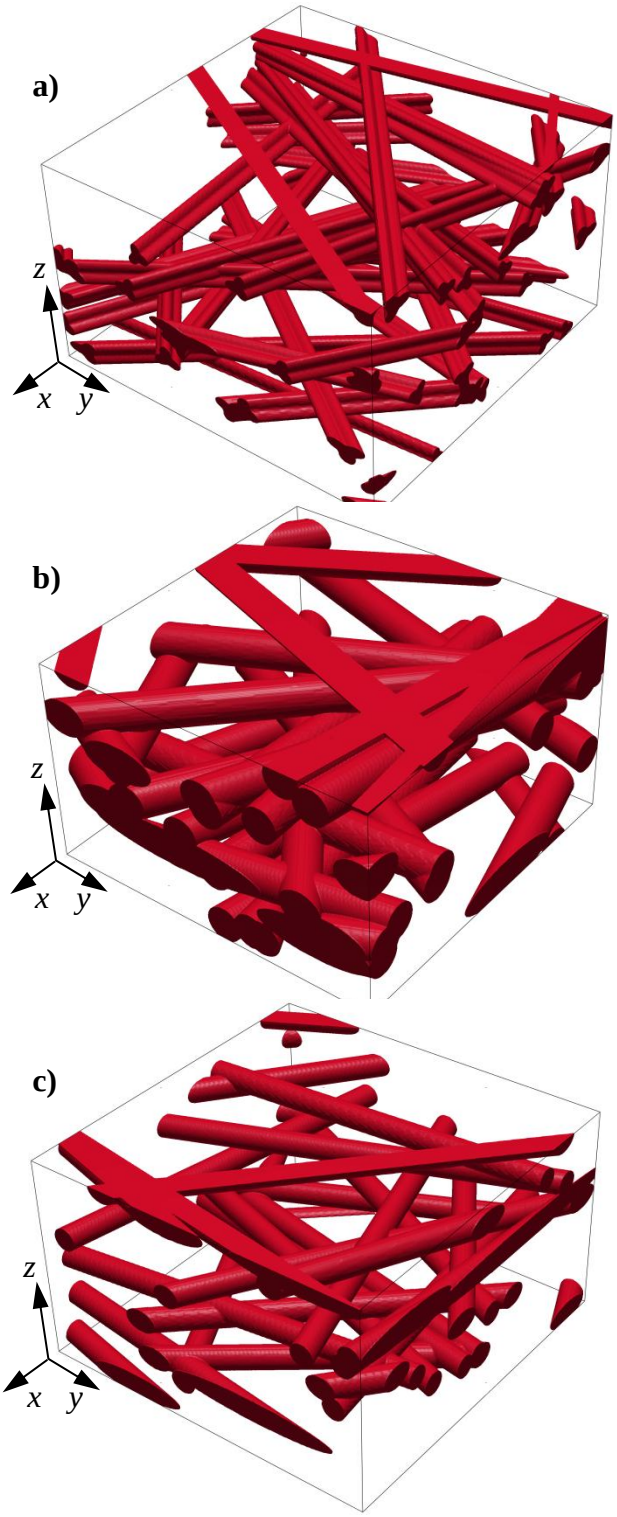

Figure 4.15: Three dimensional fibrous media with trilobal fibers having an aspect ratio of 1.5 and an SVF of 10% (a) and, circumscribed (b) and area-based equivalent media (c).

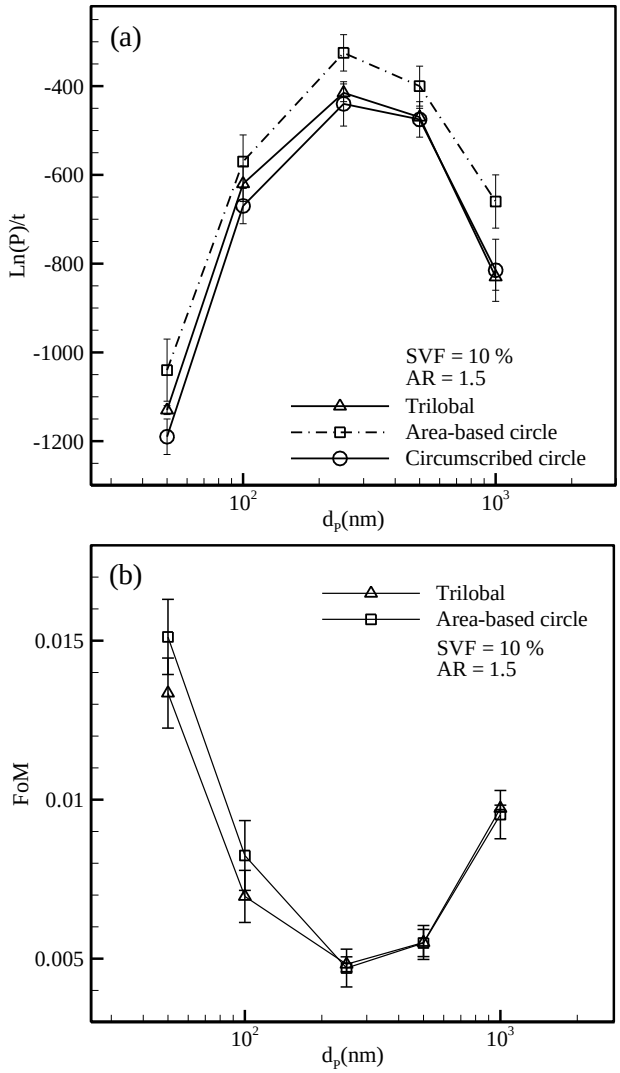

Figure 4.16: (a) Penetration per thickness and, (b) FOM calculated for the media shown in the previous figure.

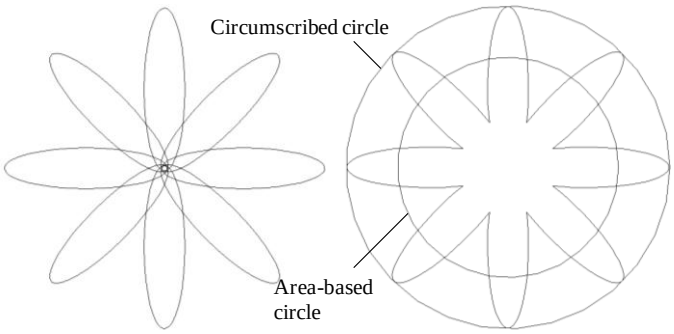

Figure 4.17: Star-shape fibers

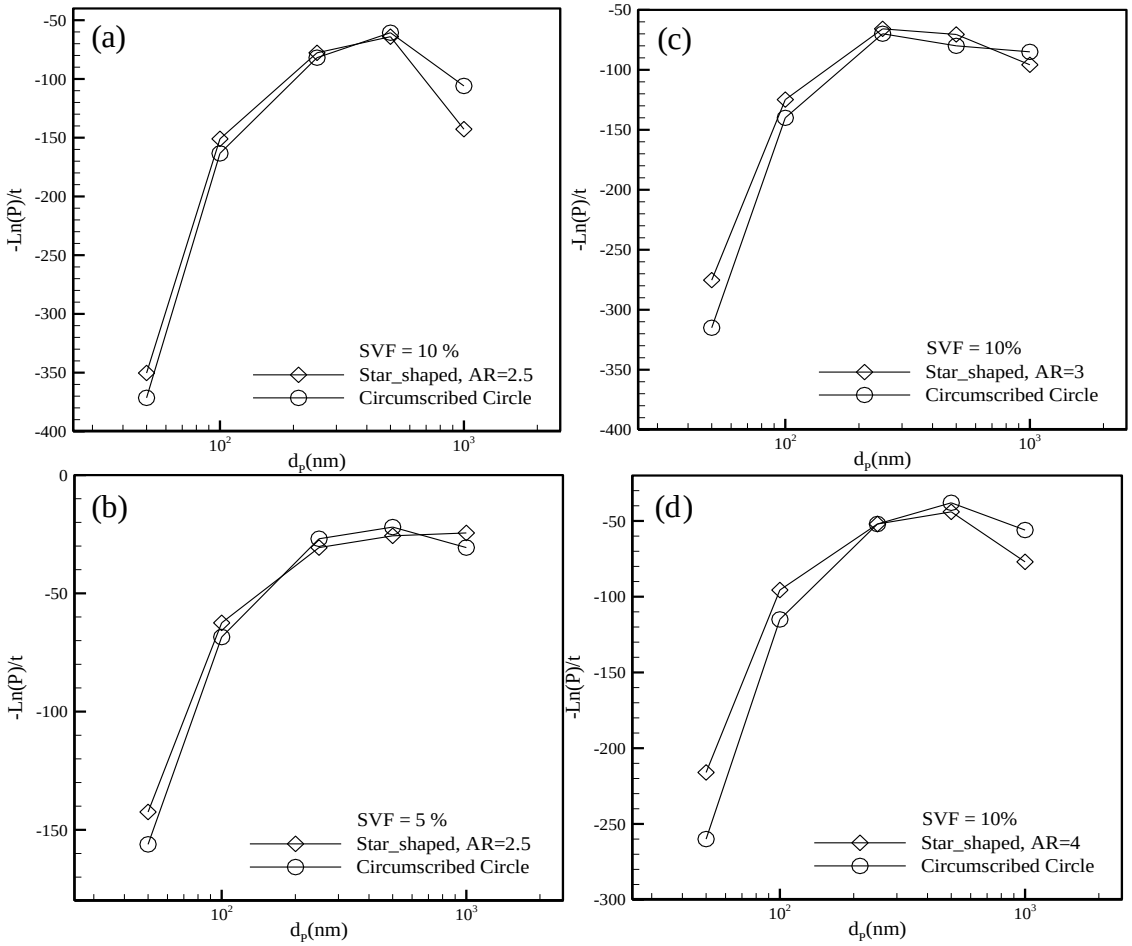

Figure 4.18: Penetration of star-shaped fibers and their equivalent circumscribed.

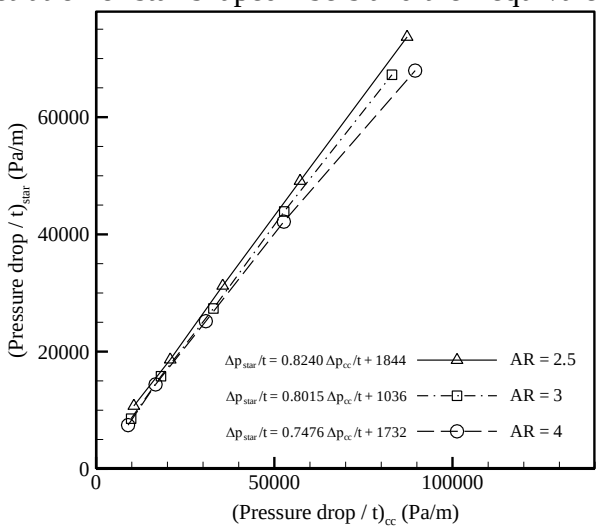

Figure 4.19: Relationship between pressure drop of star-shaped media and their equivalent circumscribed.

CHAPTER 5 Macro-Scale Modeling of Pleated Surface Filters[♣]

5.1 Introduction

Almost all existing theories of aerosol filtration are developed for flat media placed perpendicular to the air flow direction. These theories have resulted in a series of semi-analytical expressions derived for calculating filter collection efficiency and pressure drop, which have been widely used to design flat panel air filters. Most filters, however, are made of pleated media. Expressions for flat filters do not provide any information directly useful for designing pleated ones. Most of the progress made in developing pleated media has therefore been based on empiricism.

Pressure drop across a pleated filter is caused by two equally important factors. The first and most obvious contributor in the filter's pressure drop is the fibrous medium. The second contributing factor is the pleat geometry. In a pioneering work, Chen et al. (1995) modeled the pressure drop across clean filters with rectangular pleats using a finite element method and discussed the influence of the above factors in a filter's total pressure drop. These authors also showed that increasing the pleat count increases the pressure drop due

[♣] *Contents of this section have been published in an article entitled "Modeling Instantaneous Pressure Drop of Pleated Thin Filter Media during Dust Loading" by S. Fotovati, S.A. Hosseini, H. Vahedi Tafreshi, and B. Pourdeyhimi, Chemical Engineering Science, 66 (18), 4036–4046, 2011.*

to the geometry but decreases that caused by the fibrous media. Therefore, there exists an optimum pleat count at which the total pressure drop of a clean pleated filter is a minimum. To the knowledge of the authors, there are only very few studies in the literature dedicated to studying the influence of pleat geometry, and almost all of them neglect the effects of dust deposition on pressure drop (Chen et al., 1995; Lucke and Fissan, 1996; Del Fabbro et al., 2002; Caesar and Schroth, 2002; Subernat et al., 2003; Tronville and Sala, 2003; Wakeman et al., 2005; Waghode et al., 2007; Lo et al., 2010; and Rebai et al., 2010). Dust deposition can adversely affect the performance of a filter over time, and surprisingly, it has not yet been included in the theories developed for filter design. Therefore, the objective of our current study is to investigate the influence of particle deposition on the rate of pressure drop increase in filters with different pleat geometries.

5.2 Pleated Geometry and Flow Field

In this study, we assume the fibrous media to be highly efficient like those used in HEPA filters. Such media usually have a layered micro-structure with relatively low permeability. Normally, dust particles (i.e., large particles with a diameter greater than 2-3 microns) cannot penetrate through such filters. Consequentially, most of the particles deposit on the surface of the fibrous media leading to the formation of a surface cake. Our study here is aimed at modeling such filters. We performed a series of simulations to model filters having rectangular (U-shaped) or triangular (V-shaped) pleats with different widths or angles, respectively (see Figure 5.1). The geometric parameters are the pleat height L and pleat width d (or pleat angle 2θ). Another important parameter is the face velocity, which

is the flow velocity when it enters the fibrous media, medium and should not be confused with inlet velocity, which is the flow velocity as it inters the filter (see Figure 5.1).

Unlike previous chapters, in this part of the study we are dealing with Navier-Stokes equation and the convective terms are not negligible anymore. The governing equations for the flow of air a pleated geometry are:

$$\frac{\partial u}{\partial x}+\frac{\partial v}{\partial y}=0 \tag{5.1}$$

and

$$\rho\left(u\frac{\partial u}{\partial x}+v\frac{\partial u}{\partial y}\right)+\frac{\partial p}{\partial x}=\mu\left(\frac{\partial^2 u}{\partial x^2}+\frac{\partial^2 u}{\partial y^2}\right) \tag{5.2-1}$$

$$\rho\left(u\frac{\partial v}{\partial x}+v\frac{\partial v}{\partial y}\right)+\frac{\partial p}{\partial y}=\mu\left(\frac{\partial^2 v}{\partial x^2}+\frac{\partial^2 v}{\partial y^2}\right) \tag{5.2-2}$$

Governing equations for the air flow inside the fibrous media is the same as those shown in Equations 5.1–5.2, except for the convective terms on the left hand side of the equations, which will be negligible for flow in dense porous medium. In fact the filter media in our work is modeled like a porous material with a given permeability tensor. As mentioned earlier, most high-efficiency filter media have layered micro-structures, i.e., fibers that do not have any significant through-plane orientations. In such media, the in-plane and through-plane permeability constants are quite different from one another (see Tahir and Tafreshi, 2009 and Fotovati et al., 2010 for more information). Spielman and Goren (1968) proposed the following expressions for the in-plane and through-plane permeability of layered media as we presented them in Table 1.1b (Equations 1.19 and 1.20). For

completeness of the study, we have also modeled pleated filters with three-dimensionally isotropic fibrous structures. The expression of Spielman and Goren (1968) for 3-D isotropic fibrous media is given as Equation 1.21 in Table 1.1b. This information is fed into the ANSYS CFD code for simulating the pressure drop across pleated media. Due to the inherent symmetry of the pleated geometries, we only considered one pair of pleats bounded by symmetry boundary conditions (see Figure 5.1).

5.3 Modeling Dust Deposition

Unlike previous studies reported in the literature, our objective here is to simulate the effects of pleat geometry on the dust cake formation and its effects on the pressure drop. As dust particles are a few micrometers in diameter, they cannot normally penetrate a high-efficiency filter. Therefore, it is reasonable to assume that dust particles will only deposit on the surface of filter media. To model the deposition of dust particles on a filter surface, we used the Lagrangian particle tracking method. In this method, each individual particle is tracked throughout the simulation domain, and their positions are recorded once they are deposited. In the Lagrangian method, the force balance on a given particle is integrated to obtain the particle position at a given time. The dominant force acting on a particle is the air drag force and it can be modeled with the equation we introduced in previous chapters (Equation 2.10).

Previously, it has been mentioned that ANSYS treats a particle as a point mass and therefore cannot calculate the particle deposition due to interception. We have addressed

this problem by defining a User Defined Function (UDF) that modifies ANSYS's standard particle tracking scheme to include the particle deposition via interception. In fact, if a particle's center of mass reaches a distance from the filter surface equal to its radius, it will be counted as deposited. We created another UDF to make ANSYS recognize any particle whose center reaches one diameter away from the center of any deposited particle, and considers it to be captured as well. To simulate caking, we repeatedly injected batches of randomly positioned particles from the inlet until a dust cake was formed. In our simulations, we injected 160 batches of particles (each batch representing a pseudo time step). To ensure the realistic randomness of the cakes, particles should be injected from random positions on the inlet. This was accomplished by developing a UDF to enhance ANSYS's standard discrete phase module.

A User Defined Memory (UDM) value has been assigned to each marked cell (i.e., the cell containing one or more deposited particles) in order to calculate its solid volume fraction. If the solid volume fraction of a cell increased to a certain value, then the cell was considered full and no other particle was allowed to enter that cell. In addition, the permeability of that cell was decreased, which meant that this cell was a part of the dust cake medium. An additional UDF has been developed to check the UDM value of each and every cell in the domain, and to assign a permeability value (the cake's permeability constant) to them, if considered fully occupied. The cake permeability value was approximated using the Kozeny- Carman expression (Dullien, 1991):

$$k_{KC} = \frac{d_p^2 \varepsilon^3}{180\ (1-\varepsilon)^2} \qquad (5.3)$$

As it can be seen in the above equation, permeability of a granular cake strongly depends on its porosity. Determining porosity of the cakes formed by deposition of dust particles on the surface of a filter is a challenging task. However, there are a few studies in the literature that report estimated values for porosity of cakes made up of different particle diameters (Hoffmann and Finkers, 1995, Yu et al., 1997, Thomas et al., 2001, Kasper et al., 2010). Here, we used the porosity values reported by Kasper et al (2010). As will be discussed in the next section, porosity values of 65% and 85% have been considered for cakes made of particles with diameters of 10μm and 3μm, respectively. With these cell permeability values, the flow field was recalculated and the pressure drop values were reported after each particle deposition.

5.4 Results and Discussions

As mentioned earlier, we considered rectangular (U-shaped) and triangular (V-shaped) pleat shapes with different dimensions, and simulated their pressure drop with and without dust load. We assumed a constant pleat height of 25.4 mm (1 in.), and the medium thickness of 0.38 mm. For the rectangular and triangular pleats, we considered pleat counts of 3, 4, 5, 7, 10, 15 and 20 pleats per inch and pleat angles of (in Figure 5.1) 2, 4, 5, 8, 10, 15 and 20 degrees, respectively. We also used two inlet velocities of 0.2 m/s and 1.0 m/s, and two dust particle diameters of 3μm and 10μm. With a constant thickness, we arbitrarily chose different fiber diameters, porosities, and fiber orientations to simulate

different filter media with low (F1 and F4), medium (F2 and F5), and high (F3 and F6) permeability constants (see Table 5.1).

5.4.1 Pressure Drop across Clean Pleated Filters

In this section, we discuss the effect of pleat count on pressure drop in the absence of dust particle deposition (clean filters). As mentioned earlier, the total pressure drop across a pleated filter can be attributed to the pressure drop caused by the fibrous media and that brought about by the pleat geometry. For instance, increasing the pleat count (decreasing the pleat width or angle) increases the geometry-induce pressure drop, while it reduces the media-induced pressure drop. The latter is due to the fact that increasing the number of pleats increases the total filtration surface, and so decreases the face velocity. A decreased face velocity obviously results in a lower media-induced pressure drop. Similarly, decreasing the number of pleats reduces the geometry-induced pressure drop and lead to higher media-induced resistivity.

Figures 5.2a–b show the predicted pressure drop values for different U-shaped pleats at two different air speeds of 0.2 and 1 m/s, respectively. Figure 5.2c– d show similar results for V-shaped pleats. The filter media considered for these simulations are those shown in Table 5.1 (F1, F2, and F3). The optimum pleat count for our U-shaped pleats seems to be around 5 pleats per inch for the filter media with high permeability. The optimum pleat count tends to shift towards larger values when the filter media is less permeable. Similarly with the V-shaped pleats, our results indicate that with the highly permeable media, the

minimum pressure drop occurs at a pleat angle of about 10 to 15 degrees, and it moves towards smaller pleat angles (larger pleat counts) by decreasing the medium's permeability. For the range of air velocities considered in this study, the influence of inlet velocity on the optimum pleat count seems to be minor.

For the completeness of our study, we have also simulated the pressure drop for pleated filters with three-dimensionally isotropic fibrous structure (F4, F5, and F6). Note that most high-efficiency filter media have layered micro-structures similar to those of F1, F2, and F3. Three-dimensionally isotropic media are only considered here to investigate whether or not the fiber orientation and the media's anisotropy have any significant influence on the pressure drop of pleated filters or their optimum pleat counts. Interestingly, our results indicate that isotropic media produce smaller pressure drop values compared with their layered counterparts (see Figure 5.3). This is believed to be due to the fact that, for the same fiber diameter and solid volume fraction, permeability of a layered media in the through-plane direction is lower than that of a three-dimensionally isotropic media. Note that, as will be discussed in the next subsections, air enters the media at a normal angle, regardless of the pleat count (or angle) or flow velocity, and so the only component of the permeability tensor that plays a dominant role becomes the through-plane component (see Figures 5.4–5.6).

5.4.2 Dust Particle Deposition Pattern

To simulate deposition of dust particles, batches of particles were injected from the inlet over the course of several "time steps". Aerosol concentration was assumed to be 2×10^{13} particles per cubic meter. Flow field throughout the domain was recalculated after deposition of each batch of particles (each time step), and pressure drop was recorded. As dust load simulations are CPU intensive in nature, we only considered the second fibrous medium from Table 1, i.e., F2, for our dust-loaded filter simulations.

Figure 5.4 shows the dust distribution and flow streamlines inside different rectangular and triangular pleats. Particle diameter and flow velocity at the inlet are 3μm and 0.2 m/s, respectively. Figures 5.4a and 5.4c show that the dust cake covers all available filtration surfaces quite uniformly for the geometries with small pleat counts. With higher pleat counts (Figures 5.4b and 5.4d), some small dendrites are formed inside the pleats, especially with the U-shaped pleats.

Figure 5.5a and 5.5b show the dust pattern and flow streamlines inside the U-shaped pleats with 4 and 20 pleats per inch, respectively. In these simulations particle size to 10μm but the flow velocity is the same as that of Figure 5.4. Simulations for the V-shaped pleats for pleat angles of 15^{o} and 4^{o} are shown in Figure 5.5c and 5.5d, respectively. These results indicate that while the dust distribution is still somewhat uniform for wide pleats (low pleat counts either rectangular or triangular), increasing the pleat count increases the chance of tall dendrite growth, which is the case with the geometry shown in Figure 5.5b. Also, note

that in the case shown in Figure 5.5b, particles tend to travel deeper inside the pleat channels due to their considerable mass, leaving a noticeably clean surface near the pleat entrance. This happens because larger particles cannot perfectly follow their streamlines at the sharp 90-degree turn at the pleat entrance, and migrate to the center of the channel. Obviously, this effect is less pronounced with triangular pleats as the turn at the pleat inlet is milder.

The same simulations as discussed above are repeated with particles having a diameter of 10μm and the flow having a speed of 1.0 m/s (see Figure 5.6). Particles with a diameter of 10μm and a speed of 1.0 m/s have considerable inertia and tend to travel on straight lines, rather than following their streamlines when encountering a deposited particle (or a sudden turn). Consequently, if they come in contact with any deposited particle, the contact point is most probably on the upstream side of the previously deposited particles. It is interesting to note that, especially in Figure 5.6(a–b), dendrites tend to grow upstream against the flow direction, and even formed a "bridge" over some part of the filter media near the inlet (Figure 5.6a). Note also that for the pleat shown in Figure 5.6b the cake has moved deep inside the pleat. Results of Figure 5.6 reveals that with high-inertia particles, even in the case of small number of pleats one can observe non-uniform dust cake formation. Note again that the dust deposition pattern in the V-shaped pleats is more uniform than that in the U-shape pleats.

A higher pleat count results in a lower face velocity for a constant pleat height (Chen et al., 2008, and Chen et al., 1995). This is due to the fact that with higher number of pleats the filtration surface is larger, and for a constant flow rate through the filter, the face velocity is inversely proportional to surface area. However, more pleat count leads to the formation of narrower channels for the flow. The streamwise velocity through a pleat must be higher when less mass is leaving the channel walls as a result of a higher pleat count inducing a lower face velocity. Flow velocity averaged over the pleat's centerline path is reported in Figures 5.7a and 5.7b for rectangular and triangular pleats, respectively. As expected, centerline velocity increases with increasing the pleat count or decreasing the pleat angle. Because of this effect with higher pleat counts, i.e., higher streamwise and lower lateral velocities, particles tend to travel on straight line and deposit deeper inside the pleat.

For further analysis, we provided the particles' mass distribution along the x-direction over the pleats. Figure 5.8 shows the deposited mass along the x-coordinate inside U-shaped and V-shaped pleats for different flow velocities of 0.2 and 1 m/s and particle diameters of 3 and 10 μm. Mass of the deposited particles is give in an arbitrary unit as it is simply the number of cells in the domain which are occupied with particles. As can be seen, with lower pleat counts and at lower flow velocities, particles tend to cover the entire surface of the pleats. Figures 5.8c and 5.8f quantitatively show the above observation that high-inertia particles tend to deposit deep inside the pleats when the pleat count is high.

5.4.3 Effects of Dust Deposition on Pressure Drop

In the previous subsections we showed how different particle sizes and different flow speeds come into account and discussed how they may affect dust deposition for different pleat geometries. In this section we investigate the resultant effects on a filter pressure drop. In particular, here we discuss how a filter pressure drop changes with respect to its unloaded pressure drop. To minimize the statistical errors associated with random particle injection and therefore random cake formation, we repeated each of our simulations up to three times and averaged the results.

Figure 5.9 shows the pressure drop increase during particle loading in different rectangular and triangular pleats at different air inlet speeds of 0.2 and 1 m/s. It can be seen that except for the very early stages of loading, pressure drop increases almost linearly with increasing the number of deposited particles (or time), especially when the air velocity is relatively slow (i.e., 0.2 m/s). Obviously, the non-linearity in the pressure drop increase shown in Figures 5.9e and 5.9f must be attributed to the non-uniform dust deposition inside the pleats at an air velocity of 1 m/s, as discussed earlier. Interestingly, the rate of pressure drop increase is higher with low pleat counts. In other words, increasing the number of pleats greatly helps lowering the rate of increase of pressure drop during particle loading. This is in contrast to the case of clean filters where there exists an optimum pleat count at which the pressure drop is a minimum. Note that the final pressure drop is higher for larger particles when the air velocity is kept constant (see Figures 5.9a–d). This is because porosity of a cake made up of 10μm particles is less than the cake made of 3μm particles,

which leads to a lower permeability for former. When the air velocity is higher pressure drop increase is less (see Figures 9c–f), which is most probably due to the non-uniformity of the dust load. When the dust cake is not distributed uniformly over the filter media, there are places where cake thickness is very thin or there is no dust at all. This allows air to find the path of minimum resistance and flow through the filter with minimum pressure drop.

5.4.4 Effects of Cake Permeability on the Optimal Pleat Count

The results discussed so far indicated that for the range of particle diameters and air velocities considered, a higher pleat count results in a smaller rate of pressure drop increase caused by particle loading. It should be noted that this conclusion depends on the cake permeability relative to the filter media. Permeability of a granular medium (i.e., dust cake) is normally one or two orders of magnitude lower than that of a fibrous medium. This is mostly because granular beds pack denser than fibrous beds. It is informative here to investigate if a higher pleat count still causes a smaller rate of pressure drop increase if the dust cake is more permeable than the filter media. To do so, we assumed a highly porous dust cake with a porosity of 92.5% made up of particles with a diameter of 10μm. This cake is three times more permeable than the fibrous medium of the filter. Results of these simulations, conducted with an air velocity of 0.2m/s, are given in Figure 5.10. It can be seen that increasing the number of pleats does not result in lowering the rate of pressure drop increase. As the fibrous medium is the most resistive element in such a condition, non-uniform dust deposition does not necessary help with lowering the pressure drop. As

shown in the latter figure, one may still be able to find an optimum pleat count if the cake permeability is higher than the filer media.

5.4.5 A Comparison between Rectangular and Triangular Pleats

The rectangular and triangular pleat geometries discussed in the past sections did not necessarily have identical pleat counts, and so it was not accurately comment on the performance of one versus the other. In this section we intend to compare filters having rectangular and triangular pleats with identical pleat counts. Here we compare performance of a filter with 15 rectangular pleats per inch with that of a filter with 15 triangular pleats per inch (pleat angle of 4^{o}). Since both geometries have the same pleat width (d) hence each injected batch of particles in their corresponding simulation domains includes the same number of particles. Note that even though both geometries have the same pleat count, the U-shaped geometry has a slightly more filtration surface area (see Figure 5.1). The dust distribution and air streamlines inside the above rectangular and triangular pleats are shown in Figure 5.11 for different air flow velocities of 0.2 and 1 m/s and different particle diameters of 3 and 10 μm. As can be seen, a uniform dust deposition covers almost the entire filter surface when the particles are small and the air flow is relatively slow. As we increase the particle size, non-uniform dendrites begin growing inside the rectangular pleat (see Figure 5.11b). Eventually, with the large particles and fast air flow, particles travel deeper inside the channel leaving part of the filtration surface near the pleat entrance almost clean. This effect is more pronounced with the rectangular pleats. Results of Figures 5.11 clearly show that dust deposition is more uniform in triangular pleats.

Figure 5.12 shows pressure drop increase for U-shaped and V-shaped pleats for different air flow velocities of 0.2 and 1 m/s, and different particle diameters of 3 and 10 µm. These results indicate that a dust-loaded filter with rectangular pleats generate significantly higher pressure drops when compared to its counterpart having triangular pleats, if the particles are small and air flow is relatively slow (see Figure 5.12a). As the dust particle diameter increases from 3µm to 10µm, the difference between the above pressure drop values starts to vanish (see Figure 5.12b). This is believed to be due to the non-uniform dust distribution in the rectangular pleats as discussed earlier. Surprisingly, by increasing the air velocity to 1 m/s, an effect opposite of that shown in Figure 5.12a is observed (see Figure 5.12c). For the high air velocity of 1m/s and the larger particles (10µm), our simulations indicate a greater rate of pressure drop increase for the triangular pleats.

5.4.6 Effects of Pleat Height on the Performance of the Pleated Filters

It is important to investigate if the effect of pleat height can contribute to dust deposition pattern. To study this, different triangular geometries with different pleat angles have been chosen. For each pleat angle, the pleat channel with four different pleat heights has been considered. In this study only triangular pleats were considered. Six different pleat angles are considered as 15^o, 10^o, 8^o, 5^o, 4^o and 3^o where, pleat heights are equal to 25.4 mm, 20.32 mm, 12.70 mm, and 7.62 mm. The fibrous medium thickness has been kept constant and the fibrous structure inside the pleated filter for all of simulations is the same as geometry F2 in Table 5.1. The inlet velocity for all simulations is again a constant value of 0.2 m/s. Dust particles with diameter of 10 µm has been considered.

Figure 5.13 shows the clean filter pressure drop for different pleat angles and pleat heights. As can be seen, with constant angle, shorter pleat height causes more pressure drop. For larger angles, the flow field is affected mostly because of the medium and because the pleat angles become smaller.

Figure 5.14a–f shows the velocity profile along the center line of the pleated channels for all six modeled pleat angles. As can be noticed, with large pleat angle and with longest pleat height of 25.4 mm, the velocity over the centerline of the channel increases with a smooth slope and remain almost uniform in most part of the channels. By reducing the pleat height, the slope increases with faster rate and the maximum velocity happens to be at the inlet part of the channel. The smallest pleat height of 7.62 mm causes a maximum velocity at the channel inlet. Moreover, the maximum velocity over the centerline increases as we decrease the pleat angle when the pleat height is constant. This confirms that pressure drop due to geometrical effects increases when the pleat height is shorter or pleat angle is smaller.

The pressure drop due to medium depends only on the face velocity. Face velocity is the velocity which flow enters the fibrous medium. Figure 5.15(a–f) presents the face velocity over the filtration surfaces for different pleat angles and heights. For the pleat angle of 15^{o} (Figure 5.15a), and for the constant pleat height, it can be seen that the face velocity increases slightly as the flow goes deeper inside the pleated channel. In addition, by decreasing the pleat height with constant angle, the face velocity increases. The reason is

that when the pleat angle is kept constant, the flow rate at the inlet is constant and with shorter pleat height, the flow has to pass across reduced surface area and hence this causes more face velocity.

The face velocity profile does not show the uniformity that was observed for large angles as we decrease the pleat angle and as the pleat angle is reduced, the maximum of face velocity magnitude shifts toward the beginning parts of the channel (see Figure 5.15f), while it shows a slight reduction in magnitude as well. The latter perfectly explains why with smaller pleat heights, large particles tend to deposit deeper inside the pleated channels. The velocity increase causes inertial particles to move deeper and deposited near the end of the channels (see Figure 5.16).

Figure 5.17 shows similar results for the smallest pleat angle. A comparison between these two figures shows that, with larger angle and height, more uniform dust deposition has been achieved. With the smaller angle, the uniformity is less pronounced in comparison with other larger angles when the pleat height is 25.40 mm. However, this small uniformity is somehow lost when the pleat height is getting shorter and shorter. Dust particles are traveling deeper inside the pleated channel and as can be seen in Figure 5.17d, an unloaded portion of the filter surface can be observed. Larger dendrites are formed and flow inside the channel has been affected. In addition, at the site of initial entry into the filter, the streamlines are no longer perpendicular to the surface of the medium when the either pleat

height or pleat angle is reduced. All these effects confirm the fact that shorter pleat heights increase the geometrical effects.

Pressure drop ratios for different pleat angles and pleat heights are presented in Figure 5.18 (a–f). For relatively large pleat angles (Figures 5.18a–d), it seems that reducing the pleat height causes a decrease in pressure drop increase ratio, and that the minimum pressure drop increase happens to be at L= 7.62 mm with the 10 μm dust particles. In contrast, for very small pleat angles, as can be seen in Figures 5.18e–f, the trend starts to change and the minimum rate of increase in pressure drop ratio occurs at L= 12.70 mm. This clearly indicates that, unlike what our previous study showed, for constant pleat height, with various pleat heights and pleat angles there would be an optimum pleat height at which the minimum pressure drop increase is the minimum.

5.5 Conclusions

Our simulations, developed for modeling the effects of dust-load on performance of pleated filters demonstrate that there exists an optimum pleat count for clean filters at which pressure drop reaches a minimum regardless of the in-plane or through-plane orientation of the fibers. With the particle deposition included in the analysis, our results indicated that the rate of increase of pressure drop decreases with increasing the pleat count. We demonstrated that a higher pleat count results in a higher flow velocity inside the pleat channels causing more non-uniformity in the dust deposition across the pleat. Especially when particles are sufficiently large, the dust cake tends to form deeper inside

the pleated channel when the pleat count is high. This effect is observed to be less pronounced when the pleats have a triangular shape. We also showed that if the dust cake permeability is higher than that of the filters fibrous media, the rate of increase of pressure drop does not always decrease with increasing the pleat count. Finally, by comparing filters having 15 pleats per inch, we observed that rectangular pleats are preferred over the triangular pleats when the particles are highly inertial, i.e., filtering high-speed large particles. When particle's inertia is small, our results indicate that triangular pleats cause less pressure drop, and so are recommended.

Table 5.1: Different fibrous media considered for this study.

Filter media	Fiber diameter (µm)	Solid Volume Fraction (%)	In-plane Permeability (m^2)	Through-plane Permeability (m^2)	Isotropic Permeability (m^2)
F1	6	10	$2.78\ 10^{-11}$	$1.51\ 10^{-11}$	not applicable
F2	10	7.5	$1.22\ 10^{-10}$	$7.10\ 10^{-11}$	not applicable
F3	15	4	$6.92\ 10^{-10}$	$4.40\ 10^{-10}$	not applicable
F4	6	10	not applicable	not applicable	$2.25\ 10^{-11}$
F5	10	7.5	not applicable	not applicable	$1.01\ 10^{-10}$
F6	15	4	not applicable	not applicable	$5.88\ 10^{-10}$

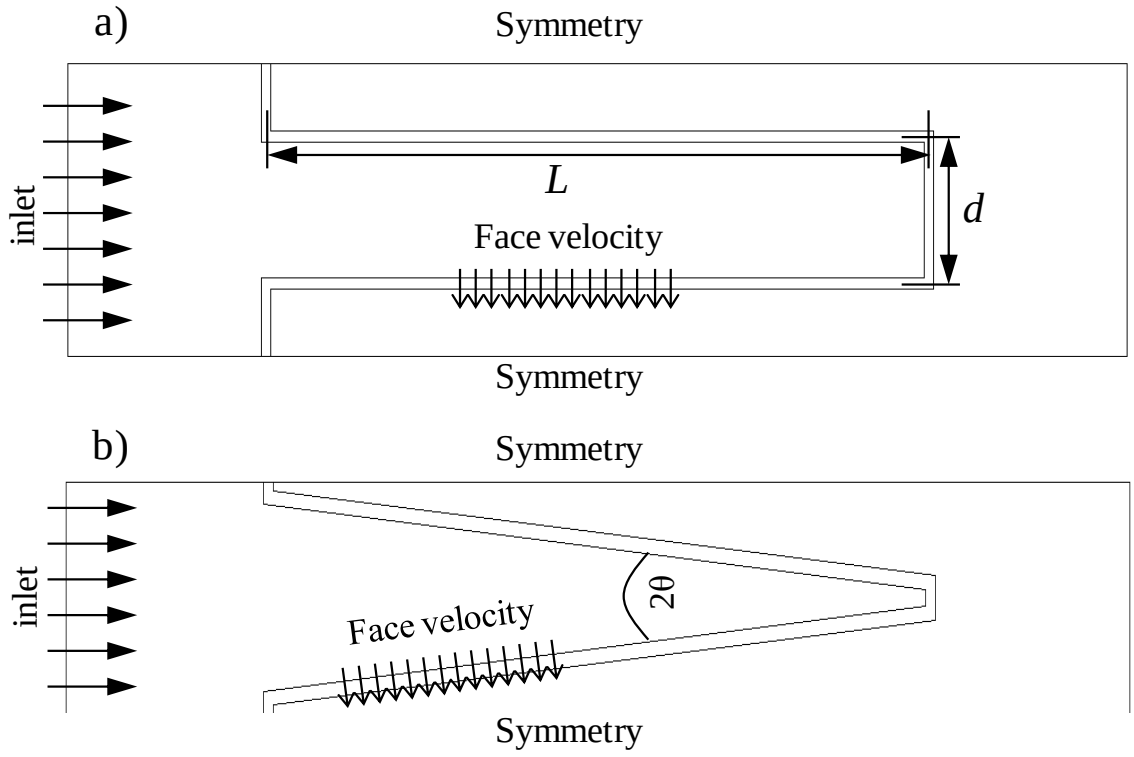

Figure 5.1: Simulation domain for a) rectangular pleats, and b) triangular pleats

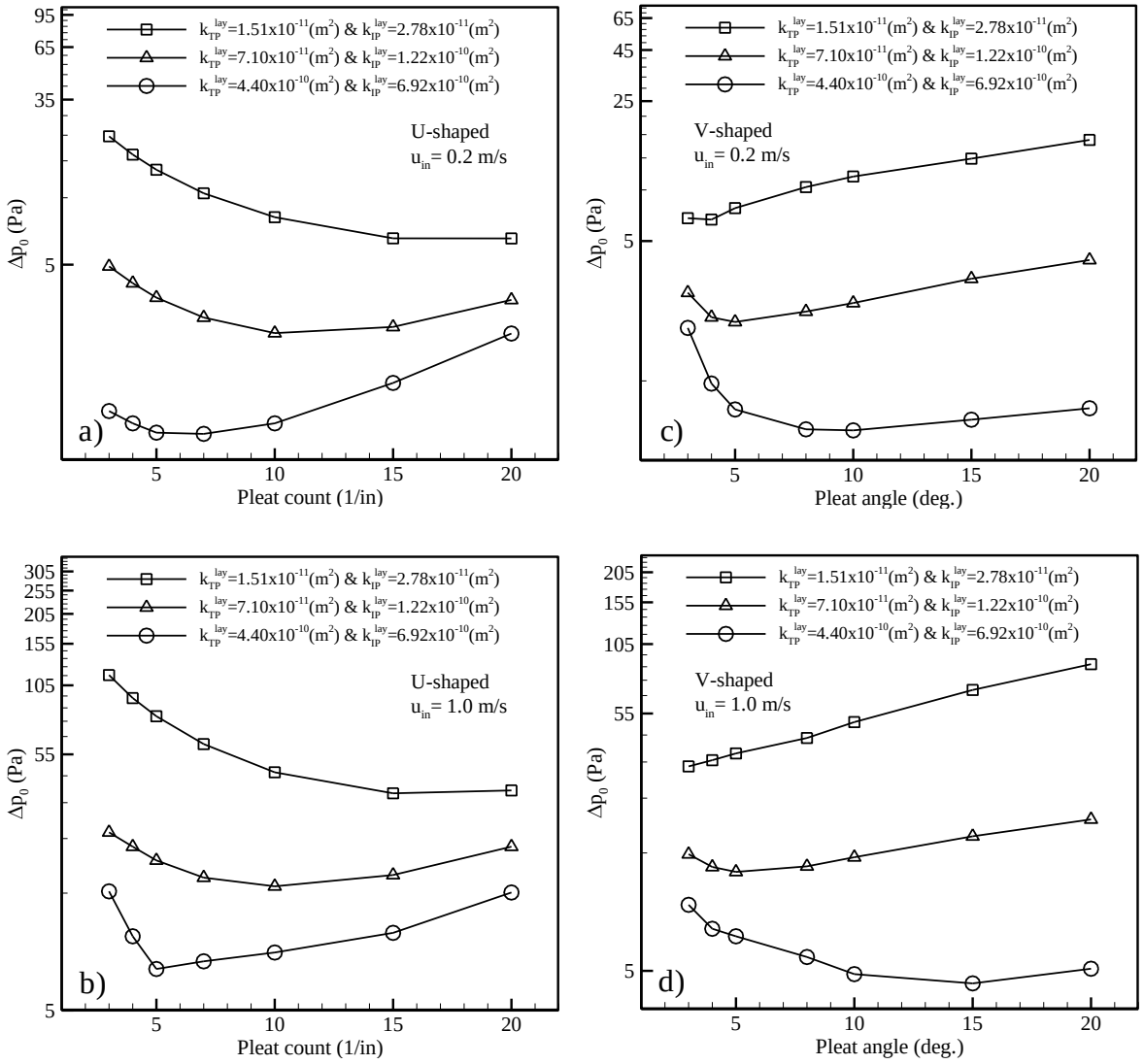

Figure 5.2: Pressure drop of clean filters with U-shaped and V-shaped pleats with different pleat counts at two different air inlet velocities of 0.2 and 1 m/s. The filter media considered here have layered micro-structures (see Table 5.1).

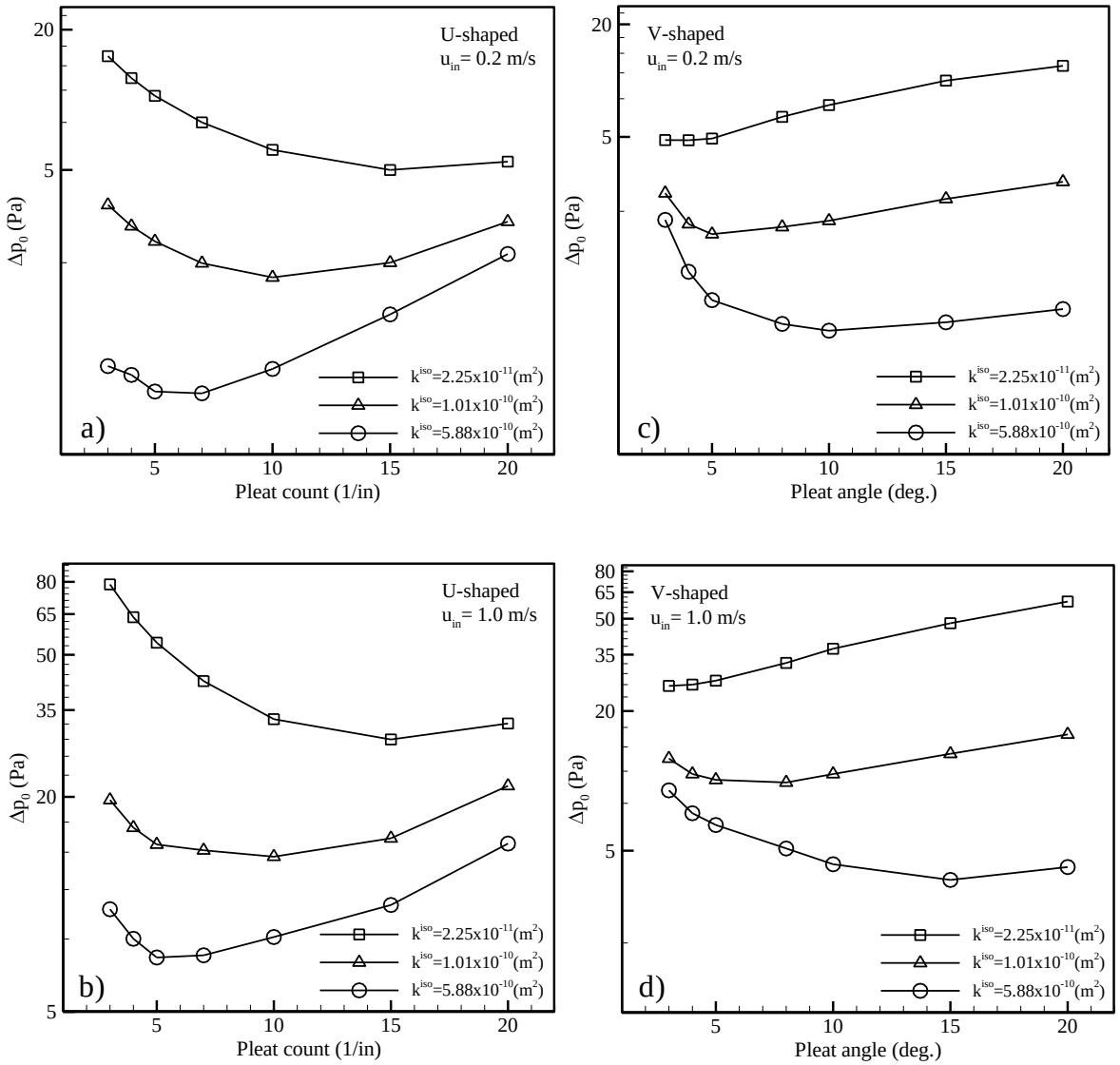

Figure 5.3: Pressure drop of clean filters with U-shaped and V-shaped pleats with different pleat counts at two different air inlet velocities of 0.2 and 1 m/s. The filter media considered here have three-dimensionally isotropic micro-structures (see Table 5.1).

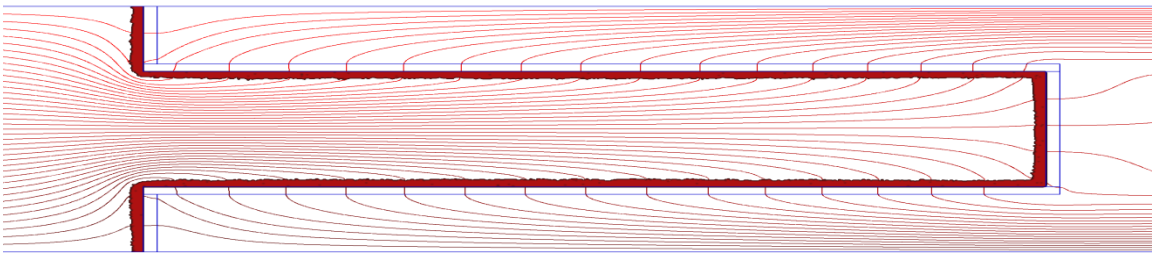

a) pleat count =4 plt/in

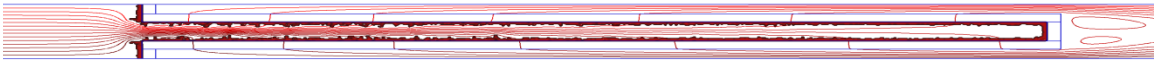

b) pleat count =20 plt/in

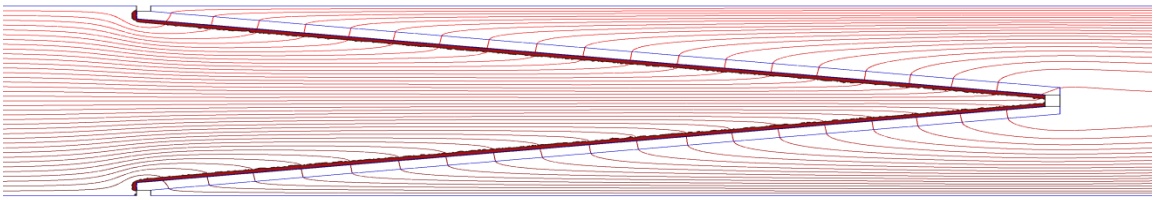

c) pleat count =6 plt/in ($2\theta = 15^o$)

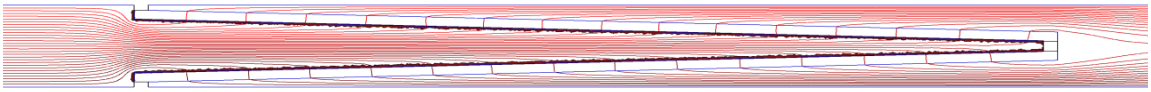

d) pleat count =15 plt/in ($2\theta = 4^o$)

Figure 5.4: Dust cake deposition pattern and air streamlines inside rectangular and triangular pleats with a) 4 pleats/ inch, b) 20 pleats/ inch, c) 15^o pleat angle, and d) 4^o pleat angle. Particle diameter and flow velocity are 3μm and 0.2 m/s, respectively.

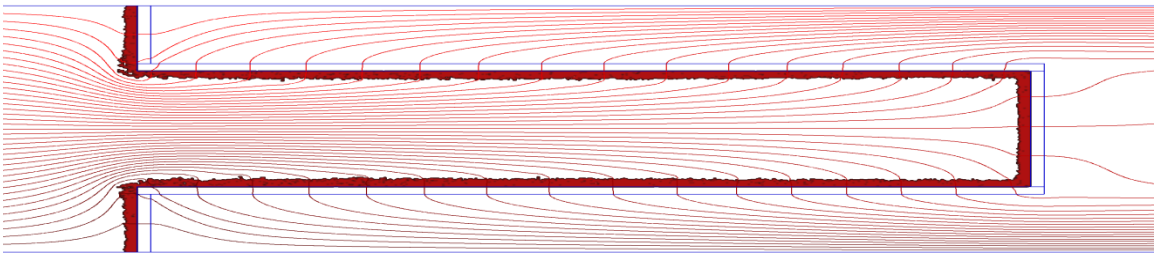

a) pleat count =4 plt/in

b) pleat count =20 plt/in

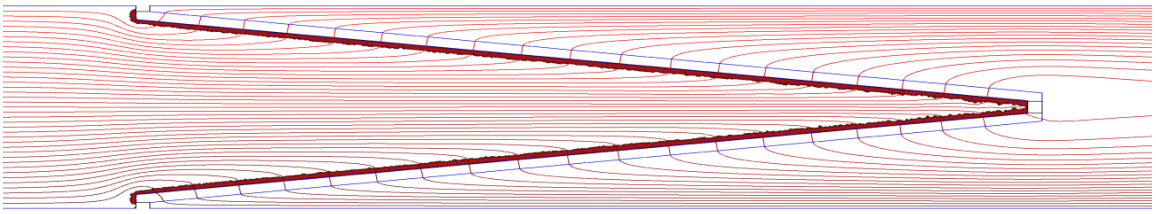

c) pleat count =6 plt/in ($2\theta = 15^o$)

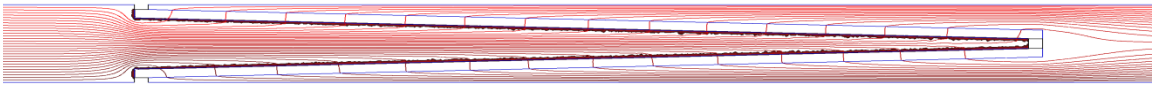

d) pleat count =15 plt/in ($2\theta = 4^o$)

Figure 5.5: Dust cake deposition pattern and air streamlines inside rectangular and triangular pleats with a) 4 pleats/ inch, b) 20 pleats/ inch, c) 15^o pleat angle, and d) 4^o pleat angle. Particle diameter and flow velocity are 10μm and 0.2 m/s, respectively.

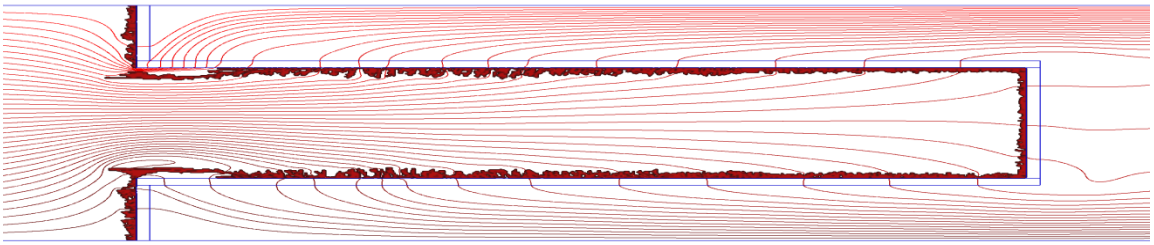

a) pleat count =4 plt/in

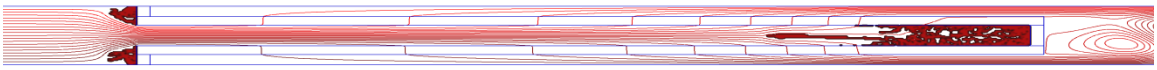

b) pleat count =20 plt/in

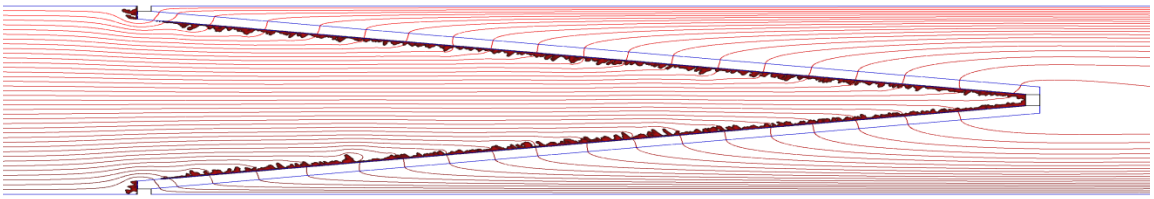

c) pleat count =6 plt/in ($2\theta = 15^o$)

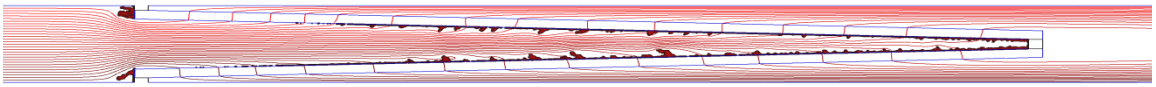

d) pleat count =5 plt/in ($2\theta = 4^o$)

Figure 5.6: Dust cake deposition pattern and air streamlines inside rectangular and triangular pleats with a) 4 pleats/ inch, b) 20 pleats/ inch, c) 15^o pleat angle, and d) 4^o pleat angle. Particle diameter and flow velocity are 10µm and 1 m/s, respectively.

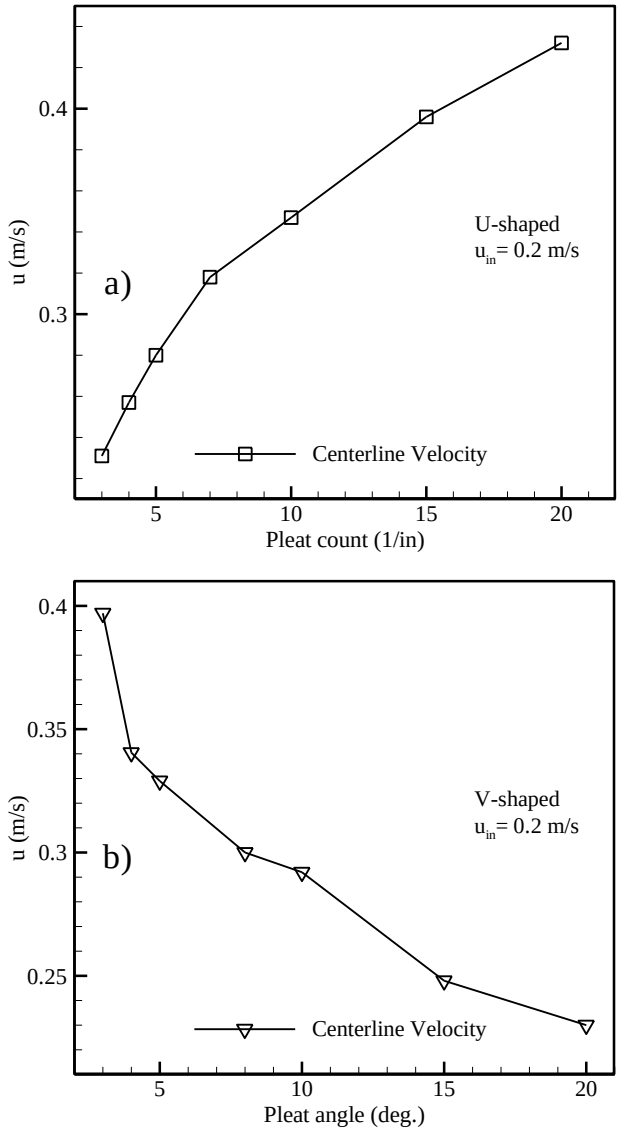

Figure 5.7: Streamwise velocity magnitude on the centerline of pleat channels for a) rectangular pleats, b) triangular pleats. The inlet velocity is 0.2 m/s.

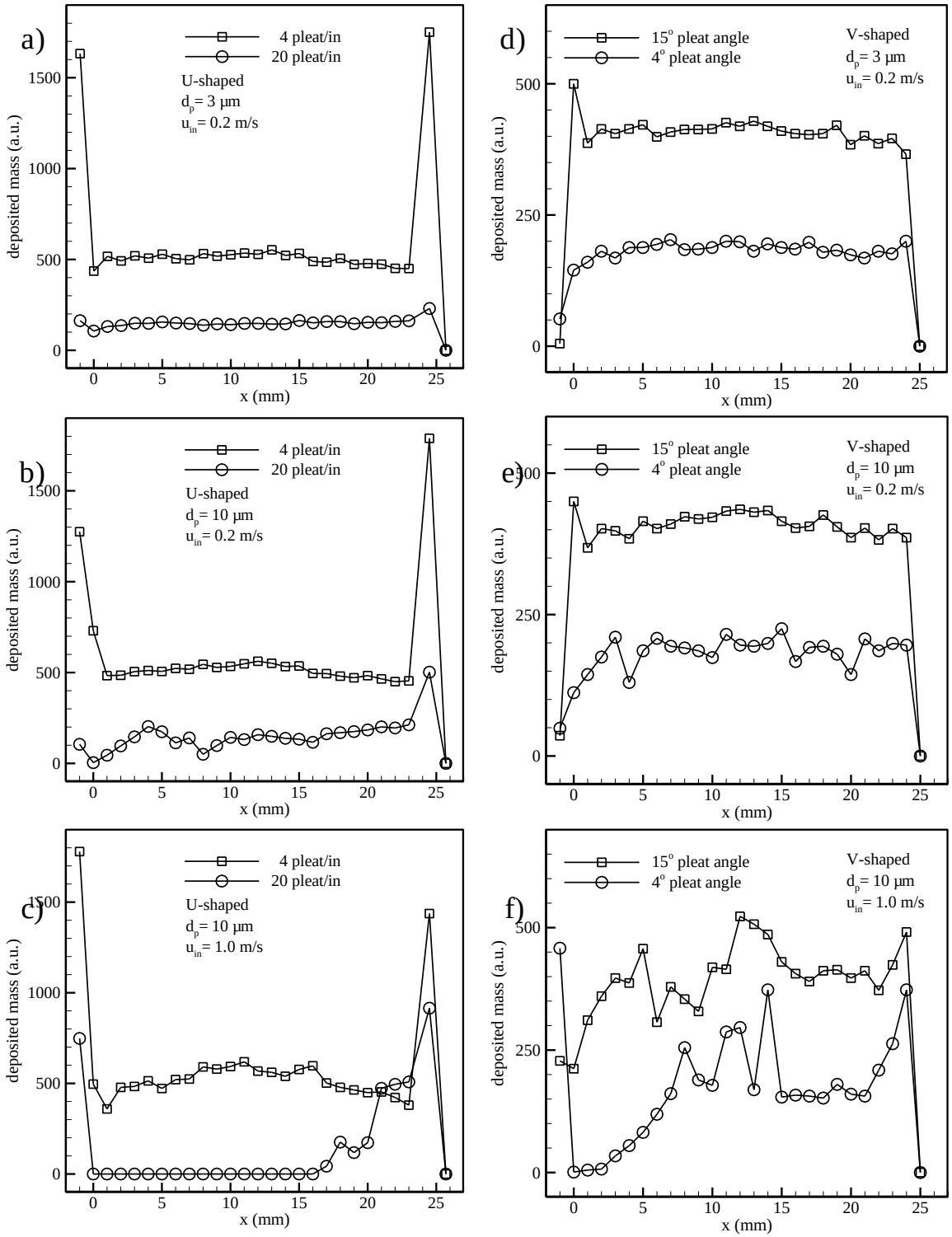

Figure 5.8: Dust cake distribution along the x-direction inside rectangular and triangular pleat geometries.

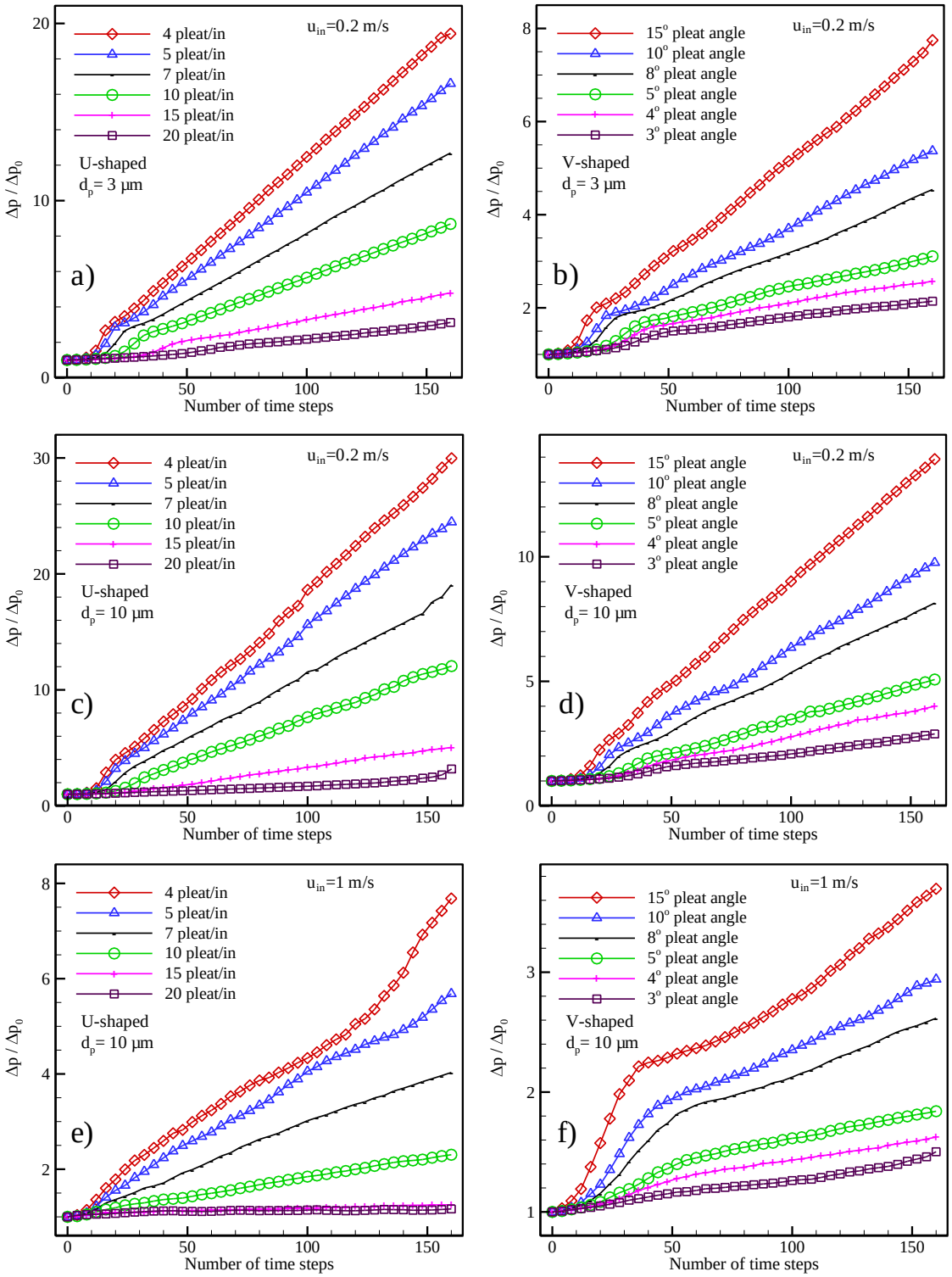

Figure 5.9: Pressure drop increase during particle loading with rectangular and triangular pleats for particles with d_p of 3 and 10μm and inlet velocities of 0.2 and 1m/s.

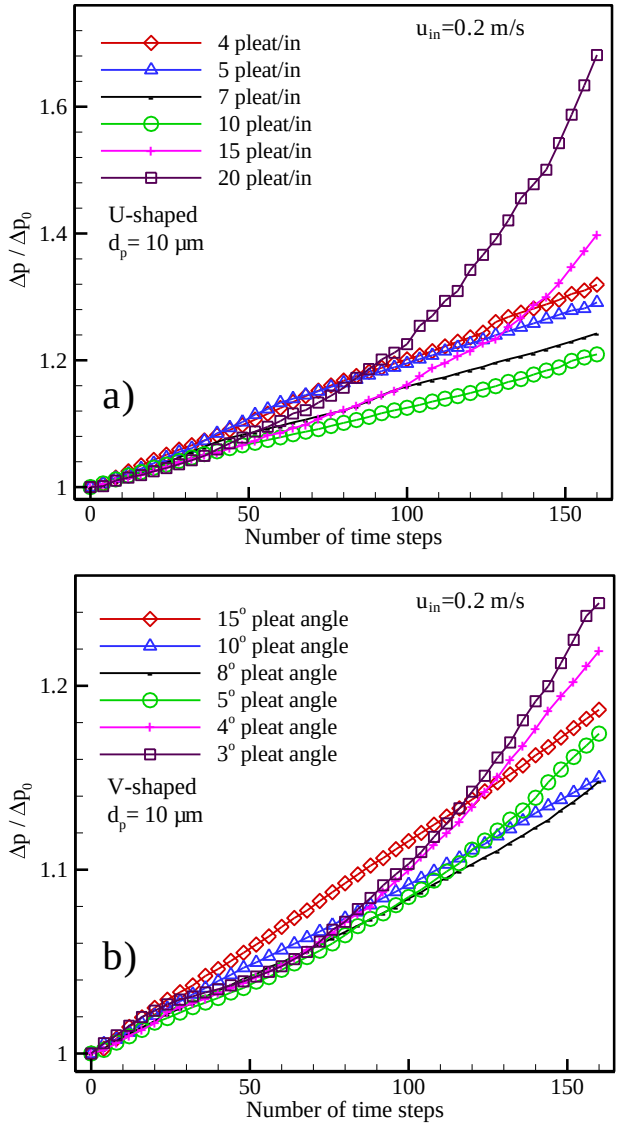

Figure 5.10: Pressure drop increase during particle loading with rectangular and triangular pleats. The dust cake is assumed to be three times more permeable than the fibrous media.

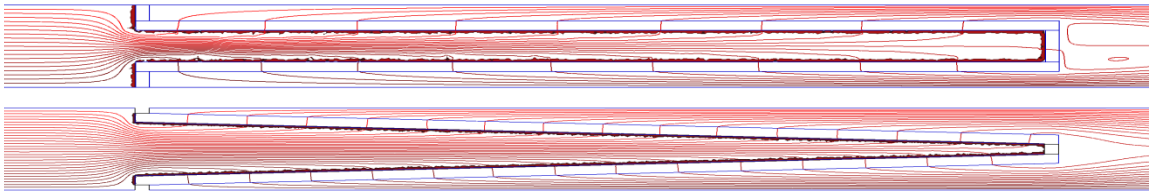

a) d_p= 3µm, u_{in}= 0.2 m/s

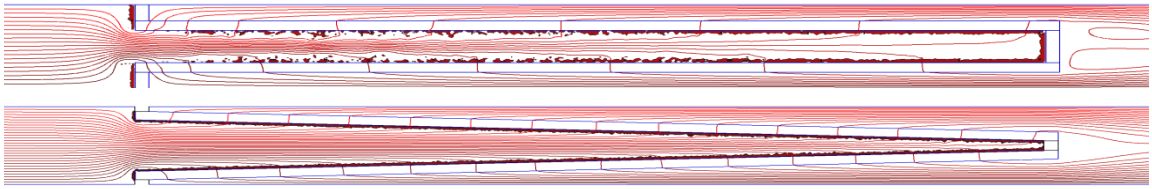

b) d_p= 10µm, u_{in}= 0.2 m/s

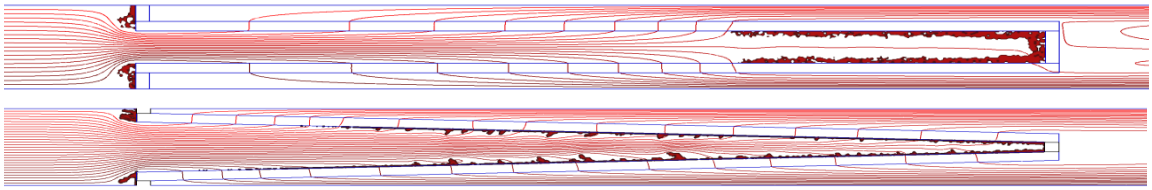

c) d_p= 10µm, u_{in}= 1.0 m/s

Figure 5.11: Dust cake deposition pattern and air streamlines inside filters with 15 rectangular or triangular pleats per inch loaded with particles having 3 and 10µm diameters with air velocities of 0.2 and 1 m/s.

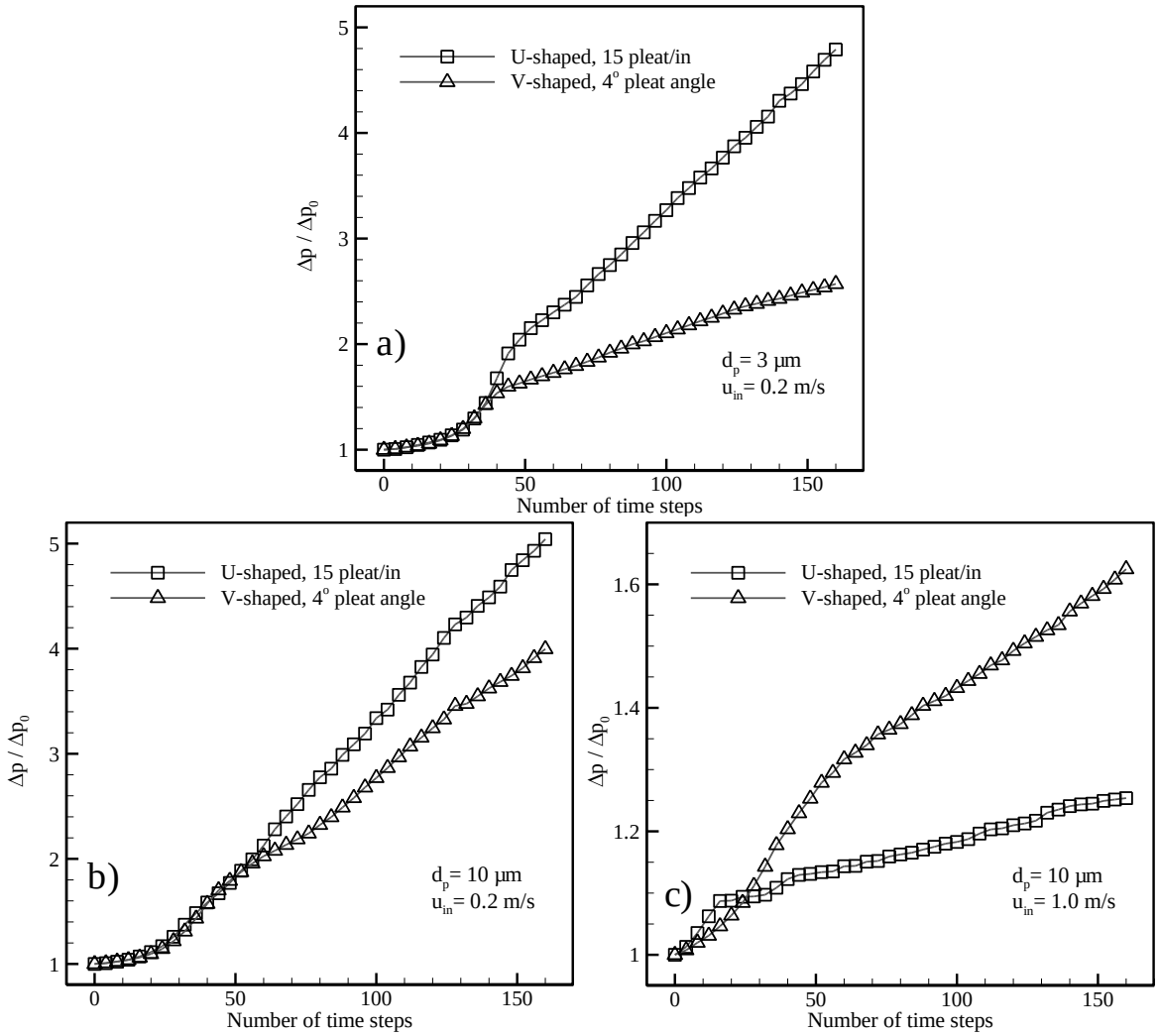

Figure 5.12: Comparison between the pressure drop increase for filters with 15 rectangular and triangular pleats per inch loaded with particles having 3 and 10μm diameters with air velocities of 0.2 and 1 m/s.

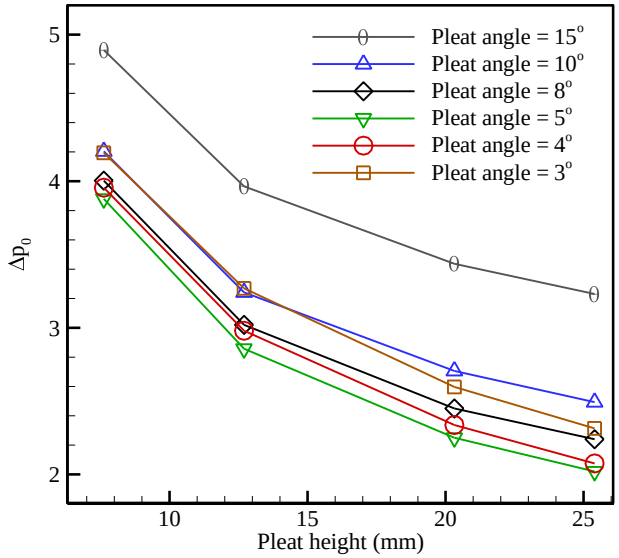

Figure 5.13: Clean filter pressure drop for pleat angles of 15^{o}, 10^{o}, 8^{o}, 5^{o}, 4^{o} and 3^{o}, regarding to different pleat heights.

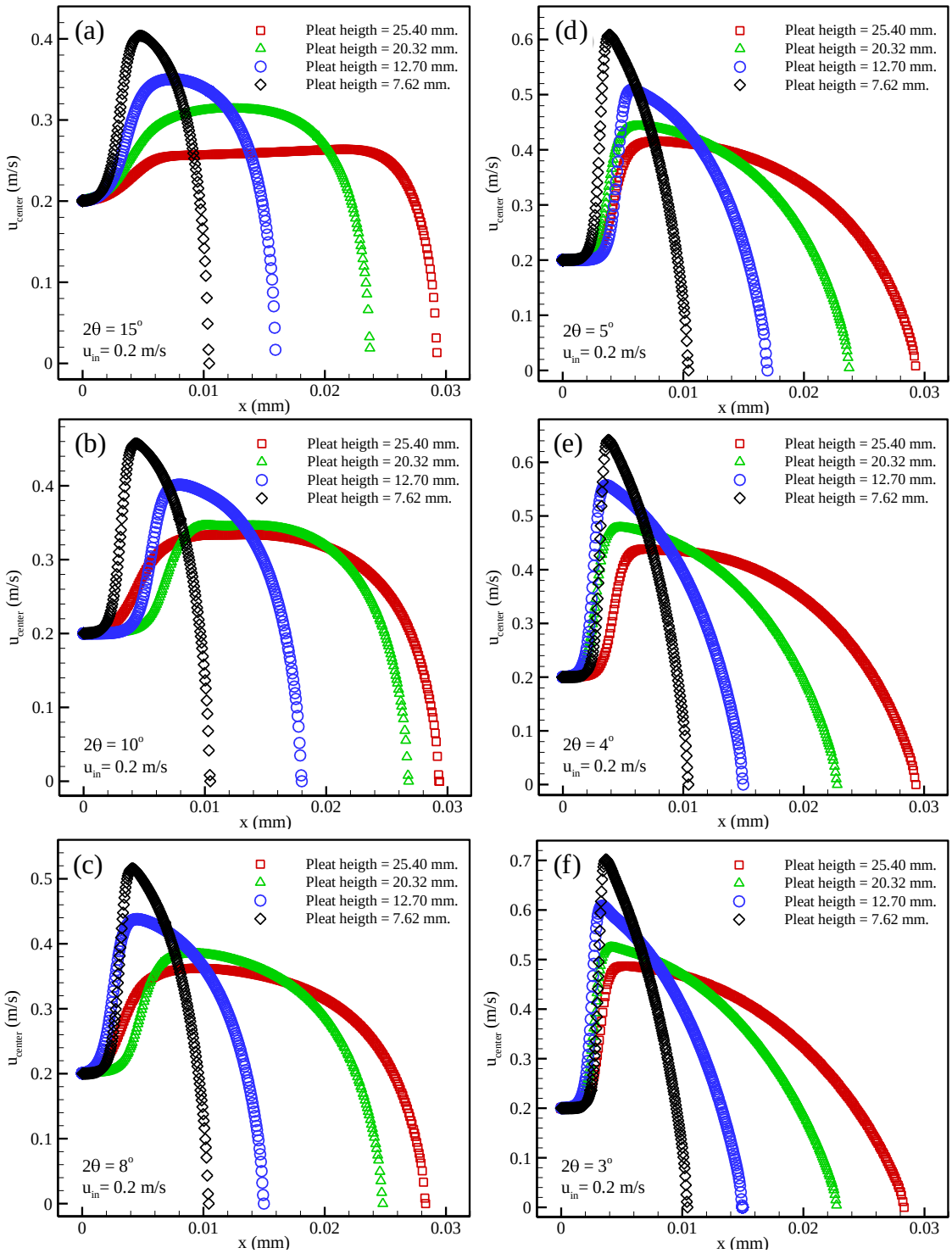

Figure 5.14: Clean filter centerline velocity profile for pleat angles of 15^{o}, 10^{o}, 8^{o}, 5^{o}, 4^{o} and 3^{o} for different pleat heights.

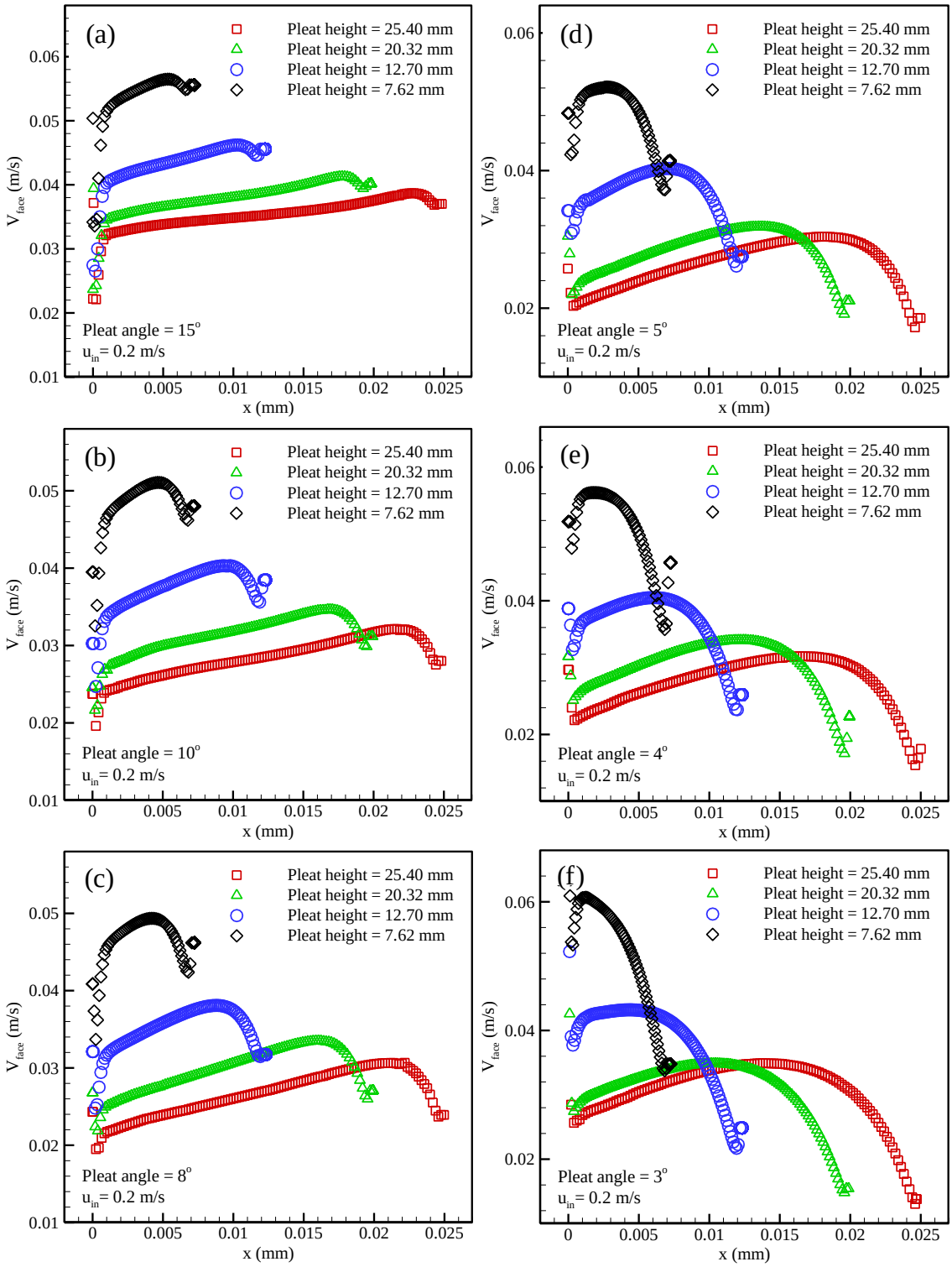

Figure 5.15: Clean filter face velocity profile for pleat angles 15^{o}, 10^{o}, 8^{o}, 5^{o}, 4^{o} and 3^{o} regarding to different pleat heights.

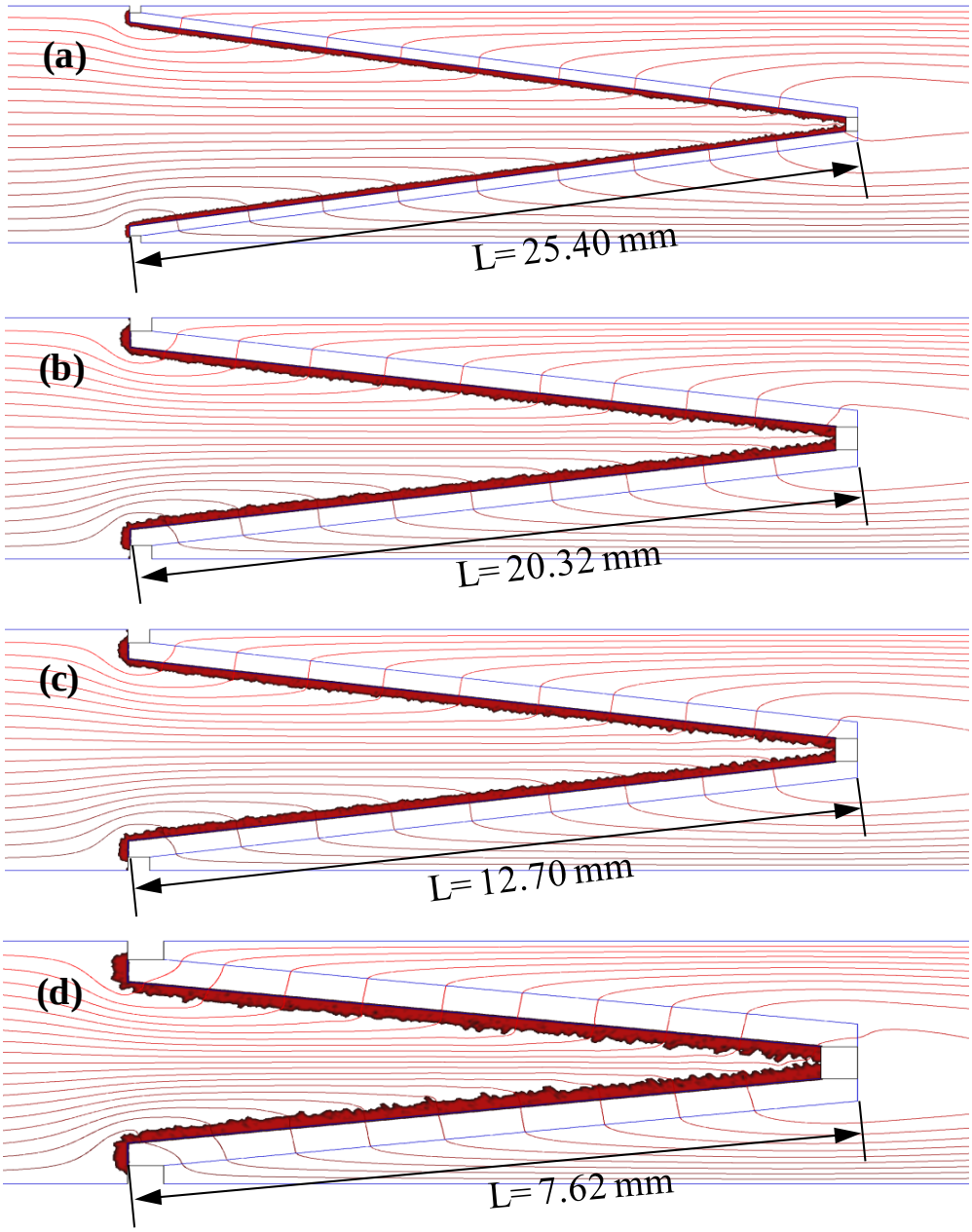

Figure 5.16: Graphical dust pattern and streamlines for pleat angle of 15^{o} and inlet velocity of 0.2 m/s with 10µm injected particles.

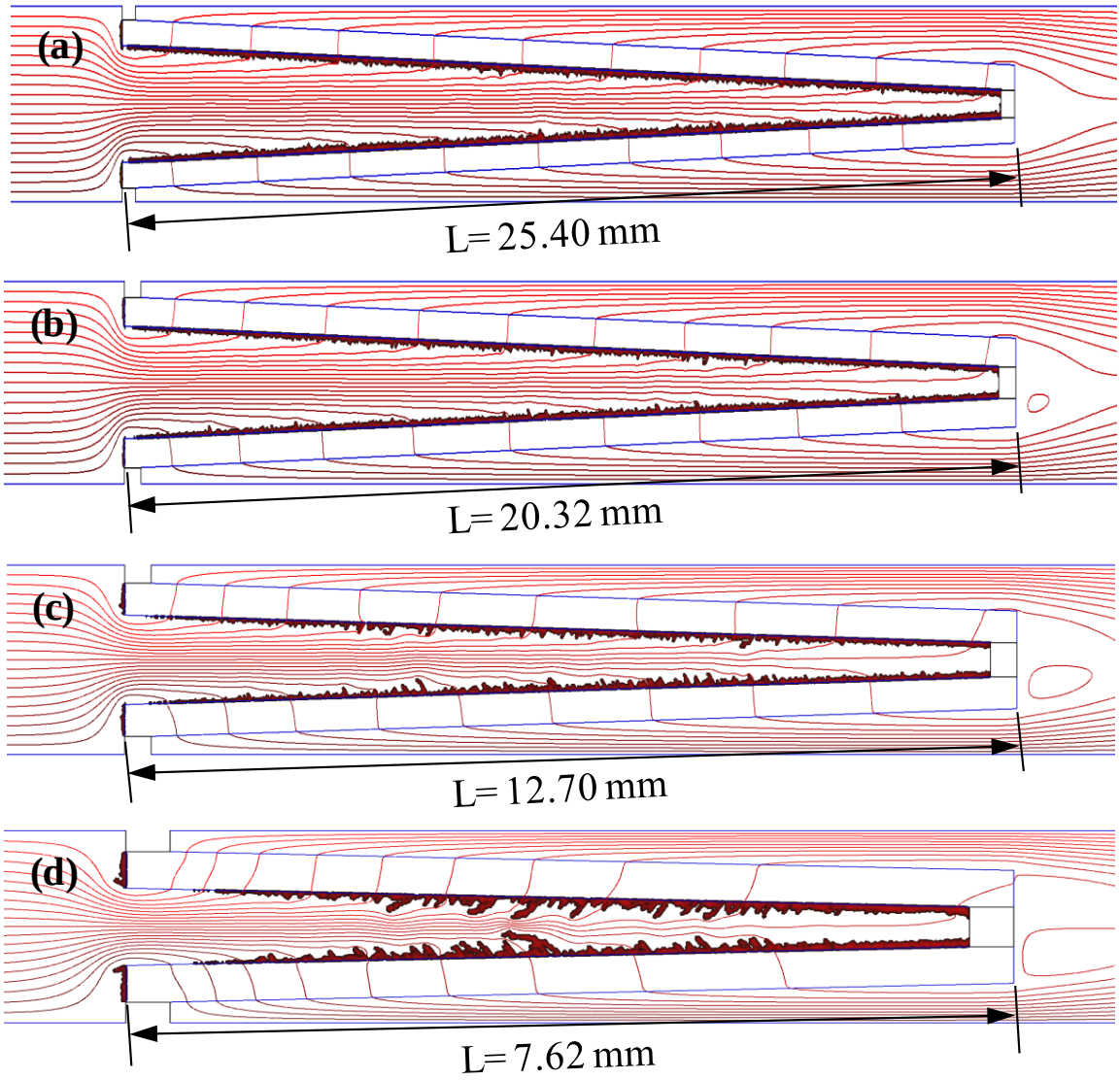

Figure 5.17: Graphical dust pattern and streamlines for pleat angle of 3^{o} and inlet velocity of 0.2 m/s with 10µm injected particles.

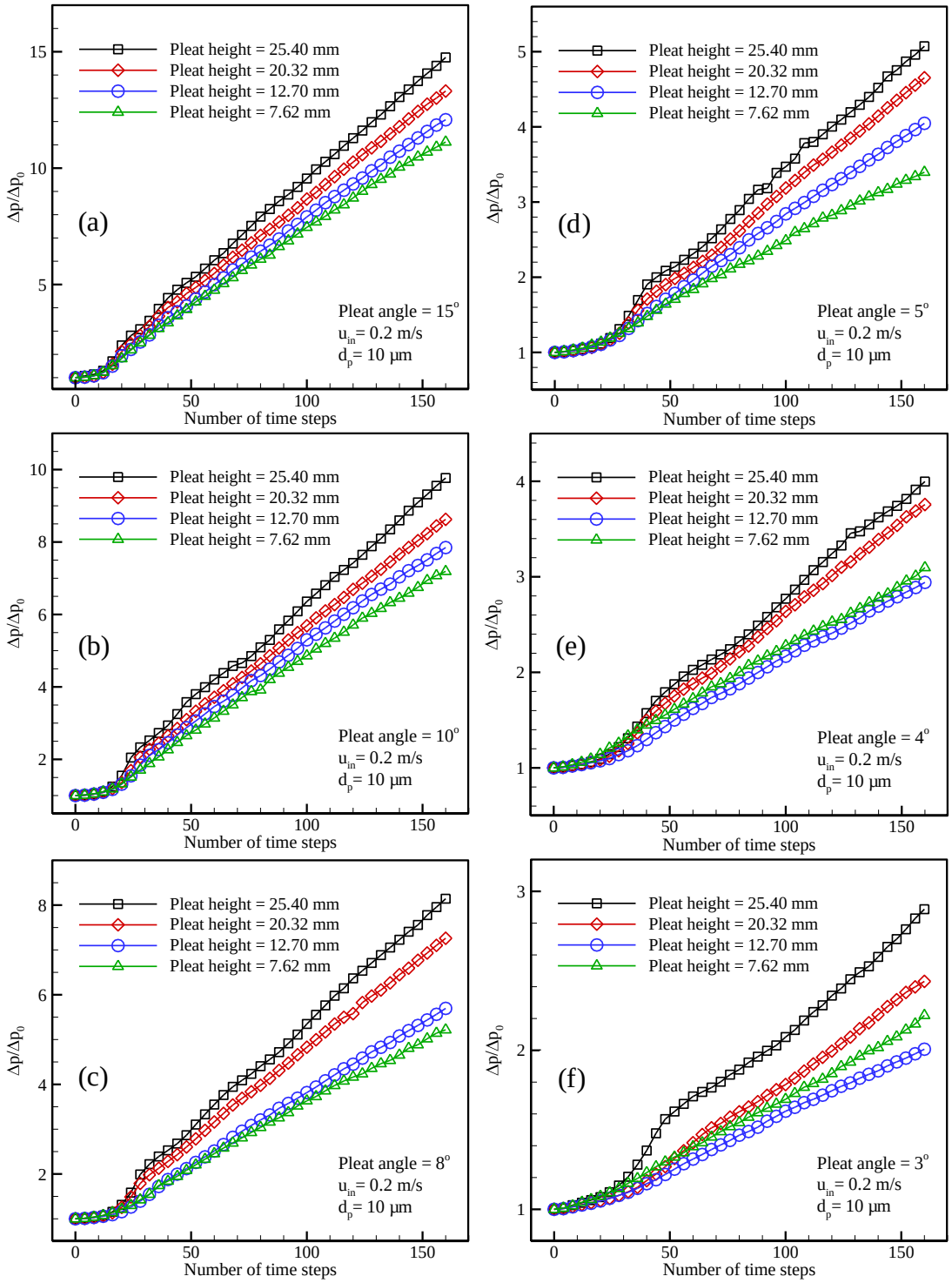

Figure 5.18: Pressure drop increase ratio respect to number of time steps for injected particles with 10µm diameter and 0.2m/s inlet velocity for pleat angles of 15^{o}, 10^{o}, 8^{o}, 5^{o}, 4^{o} and 3^{o}.

CHAPTER 6 Macro-Scale Modeling of Pleated Depth Filters[♣]

6.1 Introduction

In principle, pressure drop and particle collection efficiency of a pleated filter depend on two contributing factors. The first, and most prominent, is the fibrous medium itself, and the second, which is often underestimated, is the pleat geometry. The general consensus in designing pleated fibrous filters in industry is that a filter's collection efficiency is independent of its pleat shape or pleat count, and filter designers often optimize the pleat geometry only to minimize the filter's pressure drop. This approach is quite suitable for designing HEPA filters, where the filter media have very high particle collection efficiency. However, when a filter's particle collection efficiency small, like in the case of pre-filters or auxiliary filters used in residential buildings, the pleat geometry can significantly influence the collection efficiency of the filter, especially when the filter becomes loaded with deposited particles over time. According to the literature and published works to date, there are no criteria for designing pleat shape and pleat count for optimizing both the pressure drop and collection efficiency. More importantly, the influence of particle loading (i.e., filter aging) on performance of fibrous filters has never

[♣] *Contents of this section have been published in an article entitled "A Macro-scale Model for Simulating Pressure Drop and Collection Efficiency of Pleated Filters over Time", by S. Fotovati, H. Vahedi Tafreshi, B. Pourdeyhimi, Journal of Separation and Purification Technology , (submitted) 2011.*

been studied in the past, except for our own work, in which the effects of micron-sized dust deposition on pressure drop of HEPA filters were simulated (Fotovati *et al*., 2011). The objective of the current chapter, therefore, is to develop a methodology for predicting the effects of pleat shape on both instantaneous pressure drop and instantaneous collection efficiency of a filter.

The first numerical simulation to study the effects of pleat geometry on performance of a fibrous filters dates back to 1995, when Chen et al. calculated the pressure drop across clean fibrous filters with rectangular pleats, and showed that there exists an optimum pleat count at which the pressure drop of a clean pleated filter reaches a minimum. Since the work of Chen *et al*. (1995), only a few other investigations have been reported in the literature with regards to the effects of pleat geometry on performance of a filter as we cited them in previous chapter. None of the above studies, however, included the effects of particle loading in their pleat optimization. As mentioned before, the only available publication in which particle deposition is taken into account in developing guidelines for pleat shape optimization is that of ours presented in Chapter 5. Our previous simulations, however, were only appropriate for HEPA filters, as the influence of pleat shape or dust deposition on collection efficiency was neglected. This restriction is relaxed in the current study, thanks to a new modeling concept that we have developed for inclusion of particle deposition inside the fibrous structure over time, and simulation of instantaneous performance of the filter. This has been made possible by developing a CPU-friendly

macro-scale model that treats the fibrous structure of a filter as a porous medium with varying permeability and collection efficiency, as will be described later in this chapter.

6.2 Flow Field and Particle Tracking

In this study, we consider triangular (V-shaped) pleats with different widths (or angles) but an identical length of 25.4 mm (see Figure 6.1). The fibrous medium is assumed to have a thickness of 0.7 mm, an SVF of 5%, and a fiber diameter of 15μm. Two different inlet air velocities of 0.05 m/s and 0.5 m/s with a constant aerosol number concentration of $C = 2 \times 10^9$ m^{-3} are considered in this study. Note that the inlet velocity is the velocity of the air flow at the inlet to the filter package (or the duct in which the filter is mounted) and should not be confused with the face velocity, which is the air velocity as it enters the fibrous media. Since our simulation domain is two-dimensional, we assume a unit length for the dimension perpendicular to the simulation plane (xy plane). As the above particle number concentration cannot be directly used in our 2-D simulations, an equivalent particle concentration is obtained as follows. Let $\tilde{C}$ denote the number of particles that pass through a unit area perpendicular to the flow direction in the unit of time, then:

$$\tilde{C} = C \cdot u_{in} \tag{6.1}$$

where u_{in} is the inlet velocity. Assuming the particles to have a uniform spatial distribution, one can specify the number of particles per unit of length in the y or z-direction as:

$$N_p = \sqrt{C \cdot u_{in}} \tag{6.2}$$

Therefore, the number of particles to be injected at the inlet of our simulation domain in each batch can be found by multiplying the linear particle density N_P to the size of the inlet

boundary (i.e., *W* in the half-pleat geometry shown with solid lines in Figure 6.1). Note that each batch injection resembles a time interval equal to one second.

Due to the inherent symmetry of the pleated geometries, we only considered one pleat bounded by symmetry boundary conditions. The governing equations for the flow of air in a pleated geometry are the Navier–Stokes equations as discussed in second section of Chapter 5. Governing equations for the air flow inside the fibrous media is the same as what we have for inlet domain, except for the convective terms on the left hand side of the equations, which will be negligible for flow in dense porous medium (reducing to the Stokes equations). In fact, the filter media in our work are modeled like a porous material with a given permeability tensor. We assume that the fibrous media are layered and therefore, the in-plane and through-plane permeability components can easily be obtained from the expressions of Spielman and Goren (1968). This information is fed into the ANSYS CFD code for simulating the pressure drop across pleated media.

We used to use Equation 2.9 to model sub-micron size particles using Eulerian approach. In addition, in Equation 2.10 we presented a correlation due to a Lagrangian approach for particle tracking in which balance of drag forces exerted on a particle is integrated to obtain its speed and position over time. The latter is applied to track micron size particles where the random Brownian motion of particles is negligible. In this part of the study however, sub-micron size particles should be considered using DPM (Lagrangian approach), as we considered the fibrous structure as a lumped porous zone. Therefore,

Equation 2.9 cannot be applied here. To do so, an extra term is added to Equation 2.10 and its new 2-D form becomes:

$$\frac{du_p}{dt} = \frac{18\mu}{d_p^2 \rho_p c^c}\left(u - u_p\right) + b_1(t) \tag{6.3-1}$$

$$\frac{dv_p}{dt} = \frac{18\mu}{d_p^2 \rho_p c^c}\left(v - v_p\right) + b_2(t) \tag{6.3-2}$$

In Equation 6.3, $b_i(t)$ is the Brownian force in the i^{th} direction (Li and Ahmadi, 1992; Longest and Xi, 2007).

$$b_i(t) = G_i \sqrt{\frac{216\nu\sigma T}{\Delta t \pi \rho_p d_p^5 S^2 c^c}} \tag{6.4}$$

where G_i is a random number chosen from a normal distribution with a zero mean and a unit variance. Our particle trajectory calculations are performed by enhancing the Discrete Phase Model (DPM) of the ANSYS code with our in-house subroutines that are executed in software environment. The above-mentioned Brownian forces are incorporated into particle trajectory calculations via a User Defined Function (UDF), referred to as UDF1 here.

As will be discussed later in this chapter, our objective is to develop a computationally affordable model to simulate the formation of particle deposits inside the fibrous fabric of a pleated filter (depth filtration), and its influence on the filter's instantaneous pressure drop and collection efficiency. To accelerate the deposit formation process, a process which is very slow in both the real and virtual worlds, we treat each particle in the discrete particle

tracking model as a clusters of particles of the same size. It is then possible to assume that a cluster continuously deposits fractions of its mass (i.e., particles) as it travels through a fibrous material. In other words, each computational cell inside the fibrous media acts as a standalone virtual filter (with fiber diameter and SVF same as the whole fibrous fabric, but a thickness equal to the size of the cell) that collects a fraction of the cluster's mass. The mass of each cluster is considered to be $m_{t,j} = 3 \times 10^{-13}$ kg regardless of its diameter. With this numerical scheme, one does not need to repeat the particle injection process thousands of times or more to simulate the formation of particle deposit inside a fibrous medium.

6.3 Macro-Scale Modeling of Dust-Loaded Fibrous media

To model the deposition of aerosol particles inside a fibrous medium, the fibrous structure is treated as a lumped porous layer in which the particles can deposit over time. This causes the layer's permeability and particle collection efficiency to change over time. In contrast to our previous micro-scale modeling work (Chapters2–4), in which the micro-structure of the fibrous structures were directly included in our simulations, in the current simulations, the effects of microstructural parameters are fed to a macro-scale model that simulates the entire dimensions of the filter. To accomplish this, a series of in-house subroutines are developed to run simultaneously with the flow solver of the ANSYS code for changing the local properties of the above-mentioned porous layer over time. In this method, the SVF of each computational cell inside the filter media must be monitored and increased in response to particle deposition. Ultimately, when the SVF of a cell reaches a given limit, that cell has to become impermeable to particles (but not to air). The SVF for a

cell is defined as the ratio of the volume of deposited particles (and existing fibers) to the volume of the cell.

In reality, the particle deposit formation inside a filter is a very slow process. Developing a virtual simulation of this phenomenon requires extensive CPU time. To accelerate particle deposit formation in our simulations, we have developed a new modeling strategy in which each aerosol particle entering the domain (the discrete phase) is assumed to be a cluster of imaginary particles (replicas) with the same size as the cluster itself, as mentioned in the Section 6.2. The number of imaginary particles in each cluster n_{cl} is designed to be an input depending on the actual size of the particle and the desired CPU time (the initial mass of a cluster is a constant number arbitrarily chosen to be $m_{t,j} = 3\times10^{-13}$ kg). Injecting a cluster containing, for example, 1000 imaginary particles and tracking its trajectory throughout the filter resembles the situation in which the trajectory of such a particle, injected at the same location at the inlet, is tracked 1000 times. As our cluster travels through the fibrous zone, it loses some of its mass in each computational cell to proportional to the fraction of the above 1000 particles that will be filtered by the media.

Knowing the initial mass of a cluster at the inlet $m_{t,j}$ and the dimensions of the cells inside the fibrous media, the mass of particles deposited in each cell can be obtained using the available cell-model (see Tables 1.2–1.4) given in Chapter 1. Here, j is a counter for the number of clusters in a single injection batch at the inlet. The initial mass for the j^{th} cluster in the injection batch can be calculated as:

$$m_{t,j} = n_{cl} V_p \rho_p = 3\times 10^{-13} \tag{6.5}$$

The deposited mass $m_{d,k}$ after a cluster passes through a computational cell is:

$$m_{d,k} = m_{i,j} - m_{o,j} \tag{6.6}$$

where the counter k refers to the number of clusters passing through any particular cell (different from counter j, which is the particle identification number in the injection batch), and $m_{d,k}$ is the deposited mass after the k^{th} cluster has passed through a particular cell (see Figure 6.2). The cell's SVF can be calculated as follows:

$$\alpha_c = \frac{N_p \times \sum m_{d,k}}{\mathrm{V}_c \rho_p} \tag{6.7}$$

The flow field must be recalculated after each batch injection. However, before flow recalculation, the permeability of the computational cells inside the fibrous domain should be updated. To do so, we assume that the deposited particles make a permeable granular medium around the fibers. For simplicity, we assume the fibrous and granular porous media to act like resistors in series. We therefore update the directional permeability components of the fibrous zone and obtain effective permeability constants as follows:

$$\begin{cases} \dfrac{1}{k_{IP}} = \dfrac{1}{k_{IP}^{lay}} + \dfrac{1}{k_g} \\ \dfrac{1}{k_{TP}} = \dfrac{1}{k_{TP}^{lay}} + \dfrac{1}{k_g} \end{cases} \tag{6.8}$$

Where, the permeability of the particle bed (k_g) is calculated using the Kozeny–Carman expression (Dullien, 1991):

$$k_g = \left(\frac{d_p^2}{180}\right)\frac{\varepsilon^3}{1-\varepsilon^{\,2}} \tag{6.9}$$

As can be seen in Equation 6.9, permeability of a granular cake strongly depends on its porosity which can be calculated using the result of Equation 6.7.

The SVF of cells collecting particles will eventually reach a maximum value. This value is the minimum allowable porosity of a granular bed comprised of a given particle size. Determining the porosity of the particle bed produced by the deposition of dust particles inside a filter medium is a challenging task. We used the empirical correlation of Kasper et al. (2010) obtained for mono-dispersed particles:

$$\varepsilon_m = 0.36 + 0.44\left[\exp\left(-0.29\frac{\rho_p}{\rho_w}d_p\right)\right] \tag{6.10}$$

Note that in this equation particle diameter d_p is in micrometers. It is worth mentioning that the macro-scale modeling algorithm developed in this section of the dissertation for predicting the instantaneous pressure drop and collection efficiency of pleated filters is computationally quite inexpensive. The simulations presented in this study took on average about 3–4 hours on a single CPU with a speed of 2.50 GHz. The simulation domains considered for the study were meshed using 40000 to 250000 triangular cells depending on the geometry. Mesh-independency has been ensured by monitoring the pressure drop values obtained for clean media. Simulations presented here are obtained by considering 14 mesh-points across the thickness of the fibrous zone.

6.4 Model Implementation and Validation

6.4.1 CFD Implementation

Our simulation procedure starts by first solving the flow field inside the domain. With the local velocity vectors at each computational cell available, we trace each cluster and if this cluster is inside the filter domain, estimate the collection efficiency of each cell inside the fibrous zone by developing a new UDF, hereon referred to as UDF2, using equations given in Chapter 1. Since the DPM module of the ANSYS considers a particle as a point mass instead of an object with a finite size, UDF2 also modifies ANSYS's standard particle tracking scheme to include particle deposition via interception, which is especially important for particles depositing on previously deposited particles.

Continued particle injection results in an increase in the mass of the deposited particles inside the cells. With the mass of deposited particles and their diameter available, new SVFs (and so new permeability constants) will be assigned to the affected cells via a third UDF (UDF3) that incorporates Equation 6.7 into the calculations. This procedure will be repeated until the SVF of a cell inside the medium reaches a certain value obtained using Equation 6.10. If a blocked cell is located upstream of the fibrous zone, further particle encounters will result in surface deposition (as opposed to the depth deposition). We stop our particle loading simulations before surface loading begins, as it is outside the scope of the current study.

We define a User Defined Memory (UDM) for cells that are filled with particle deposits to mark them as "blocked". UDMs are allocated memory storage locations which are assigned to each computational cell in the ANSYS code. When a cluster passes through a cell within the fibrous domain, the amount of deposited mass must be recorded. To do so, we defined another UDM for the amount of mass deposited in each cell. With the mass of particles deposited in each cell recorded, UDF2 updates the SVF of the cells and stores the information in another UDM. An additional UDF, hereon called as UDF4, is also developed to update the permeability tensor of the affected cells. The above steps are shown more systematically in the flowchart shown in Figure 6.3. The final UDF (UDF5) that we have introduced into our simulation maintains the random injection of particles into the domain.

6.4.2 Validation

To investigate how accurately the above methodology can simulate reality, we considered a flat sheet filter—the only case for which some analytical/experimental correlations are available. We started our investigation by modeling pressure drop and collection efficiency for a clean filter. As can be seen in Figure 6.4, for a flat sheet with an SVF of 5%, a fiber diameter of 15 μm, and an inlet air velocity of 0.2 m/s, our model predicts clean filter collection efficiency values (shown in terms of $-\ln(P_0)/t$) in perfect agreement with the cell-model equations given in Chapter 1. Since the same equations are used in the calculations shown in Figure 6.4, this agreement only indicates that there are no errors with regards to the implementation of the cell-model equations in our simulations.

To simulate particle-loaded filters, we allow the particles to deposit inside the fibrous domain. Figure 6.5 shows an example of our particle deposition simulations inside a flat fibrous sheet at two different times during particle deposition. Particles have a diameter of 10 μm and the air inlet velocity is 0.05 m/s. Formation of particle dendrites and the preferential paths of minimum resistance chosen by the streamlines can easily be seen in this figure and its magnified subfigures. Here Black to white shows SVF of the cells in the fibrous zone. The maximum allowable SVF is 0.6 here.

Only a few empirical correlations are available for predicting the instantaneous pressure drop of a fibrous medium. Thomas *et al*. (2001) presented a semi-empirical expression to obtain the pressure drop of loaded flat-sheet fibrous media,

$$\Delta p = \Delta p_0 + \kappa u_{in} m \qquad (6.11)$$

where κ is defined as $\kappa = h_k a_p^2 (1-\varepsilon)\mu / (c^c \varepsilon^3 \rho_p)$. Note that h_k is the Kozeny constant considered to be 5 for spherical particles. Figure 6.6 shows our pressure drop predictions as a function of the mass of deposited particles for two different particle diameters and at two different flow velocities. The predictions of Equation 6.11 are also added to this figure for comparison. It can be seen that our instantaneous pressure drop calculations match reasonably well with the predictions of Equation 6.11. Note that the *x*-axis in this figure is the deposited mass m^*, non-dimensionalized using the mass of a single particle. After each flow batch injection (i.e., time step), the total amount of mass deposited inside the fibrous zone is recorded and used in Equation 6.11.

It is hard to present a one-to-one validation for our instantaneous collection efficiency calculations here, only because most existing expressions for collection efficiency in the literature require a variety of case-dependent empirical coefficients. However, to show that our results for collection efficiency (penetration) follow a reasonable trend, we used the expression of Kanaoka *et al*. (1980) as given below.

$$E_{\Sigma} = E_{\Sigma 0}\ 1+\lambda m \qquad (6.12)$$

where λ is an empirical factor obtained here via curve fitting. $E_{\Sigma 0}$ is the total single fiber collection efficiency of a clean fiber. Figure 6.7 shows our predictions of $-\ln(P/P_0)$ as a function of the mass of particle deposit in the filter. Equation 6.12 is fitted into our results to better illustrate the trend of our simulation results.

6.5 Results and Discussions

In this section, we simulate filters with V-shaped pleats. In-plane and through-plane permeability constants for the filter material are obtained using Equations 1.19 and 1.20 to be $k_{IP}^{lay} = 5.028\times10^{-10}\,\mathrm{m}^2$ and $k_{TP}^{lay} = 3.117\times10^{-10}\,\mathrm{m}^2$, respectively. We considered filters with 4, 6, 8, 10, and 12 pleats per inch. To study the performance of clean filters, we considered the particles ranging in size from 100 nm to 10 μm. With the unsteady simulations (filter aging simulations), however, we only considered particles of 100 nm and 3 μm diameters. These particles are chosen to simulate performance of our filters against low- and high-inertia particles.

6.5.1 Clean Pleated Filters

Figure 6.8 shows $-\ln(P_0)/t$ for filters with different pleat counts. Our results indicate that, for light particles (e.g., submicron particles), higher collection efficiencies can be achieved by increasing the pleat count. However, the effect of pleat count on collection efficiency is negligible, or even becomes reserved, when particles are inertial (e.g., particles with a diameter of about 10 microns). Note that as can be seen in Figure 6.8, this trend is valid for at least any inlet velocities between 0.05 to 0.5 m/s. The effects of pleat count on collection efficiency can be better explained by reporting the area-averaged face velocity over the filtration surface in Figure 6.9a. It can be seen that face velocity decreases with increasing pleat count. This improves particle capture due to Brownian diffusion, but adversely affects particle capture due to inertial impaction. Therefore, the collection of a filter changes depending on which capture mechanism is dominant for the given particle size.

Pressure drop values obtained for our clean pleated filters are presented in Figure 6.9b for inlet velocities of 0.05 and 0.5 m/s. It can be seen that there exists an optimum pleat count at which pressure drop is minimized, as expected.

6.5.2 Particle-Loaded Pleated Filters

To simulate particle-loaded filters, we allow the particles to deposit inside the fibrous domain. Figure 6.10 shows an example of our particle deposition simulations inside V-shaped geometries. Note how the streamlines adjust their paths between the particle dendrites to flow through the most permeable regions.

In Figures 6.11, we present the influence of pleat count on the instantaneous performance (pressure drop and collection efficiency) of pleated filters versus time for two different particle diameters of 100 nm and 3 μm and flow velocities of 0.05 and 0.5 m/s. Note in these figures that simulation time is different for aerosols with different particle diameters or velocities. This is because, as mentioned before, each particle injection represents a time interval equal to one second, and to accelerate particle deposit formation process, we have assumed each injected particle to be a cluster of many particles with the same diameter as the cluster itself. Therefore, injecting a batch of clusters with each cluster containing n_{cl} particles accelerate the simulation time by a factor of n_{cl}. Note again that since loading is a slower process for smaller particles, we have chosen a larger value for n_{cl} when simulating small particles. The n_{cl} values are obtained by considering a constant mass for the clusters regardless of their size. It is important to note that although a constant mass is considered for each cluster $m_{t,j} = 3\times10^{-13}$ kg (and the number concentration of the clusters at the inlet has been kept at $C = 2\times10^{9}$ m^{-3}) this does not mean that the mass concentration of the aerosol particles has been kept constant for all the simulations reported here. The value considered for the mass of our clusters is only an arbitrary number and does not need to be held constant when varying the particle diameter. In our simulation method, the number concentration of the aerosol particles is help constant kept at $C = 2\times10^{9}$ m^{-3} and the concept of clusters and imaginary particles within a cluster are only a means of advancing in time without actually repeating the particle injection process.

The results shown in Figures 6.11and 6.12 indicate that the rate of increase of pressure drop and collection efficiency decreases by increasing the number of pleats. This is chiefly due to the fact that when a pleated filter is exposed to a given aerosol flow, each pleat receives less number of particles when increasing the pleat count. Also note that increasing the flow rate (flow speed) increases the rate of pressure drop increase, as expected (see Figures 6.11a–d). Similarly, pressure drop increases much faster when particles are larger (note that all filters are exposed to an aerosol with a fixed number concentration rather than fixed mass concentration). As can be seen in Figures 6.12a–d, the rate of change of collection efficiency is more for filters with less number of pleats. The information given in Figures 6.11–6.12 clearly demonstrate that the new algorithm developed in this work can be used to predict the instantaneous pressure drop and collection efficiency of a fibrous filter in its entire actual dimensions and with an affordable computational time.

6.6 Conclusions

This Chapter has been focused on developing a novel macro-scale model for studying the aging of pleated filters. To date, the current work is the only numerical simulation capable of quantifying the effects of dust deposition inside the fibrous fabric of pleated filter media to predict the instantaneous pressure drop and collection efficiency of a filter. Our simulations with pleated filters exposed to flows of aerosol particles with different diameters and velocities indicate that increasing the number of pleats decelerates the aging of a filter. It was also shown that increasing the speed of the flow or the diameter of the aerosol particles accelerates the aging process, if the aerosol number concentration is held

constant. Our algorithm has been used to obtain pressure drop values for dust loaded flat sheet media. These values are compared with the experimental data reported by Thomas *et al*., (2001), and good agreement has been observed.

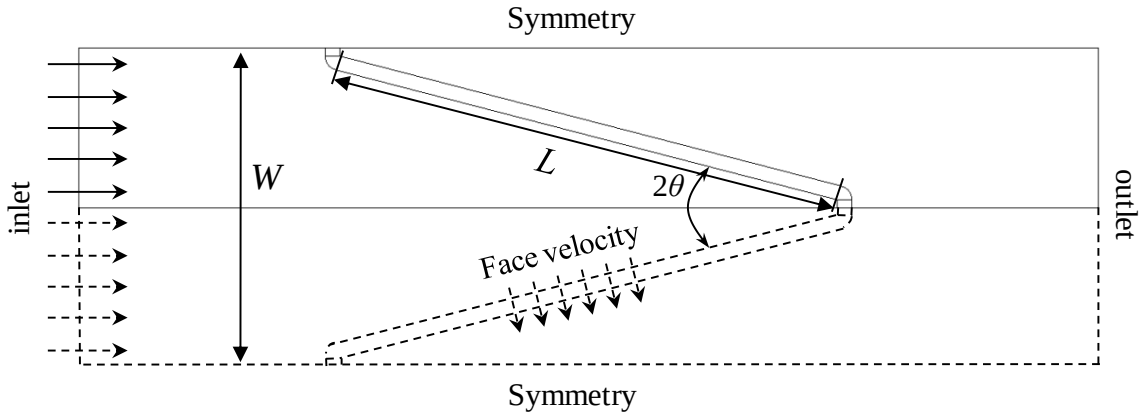

Figure 6.1: Simulation domain for triangular pleats with a pleat angle of 2θ and a pleat height of L.

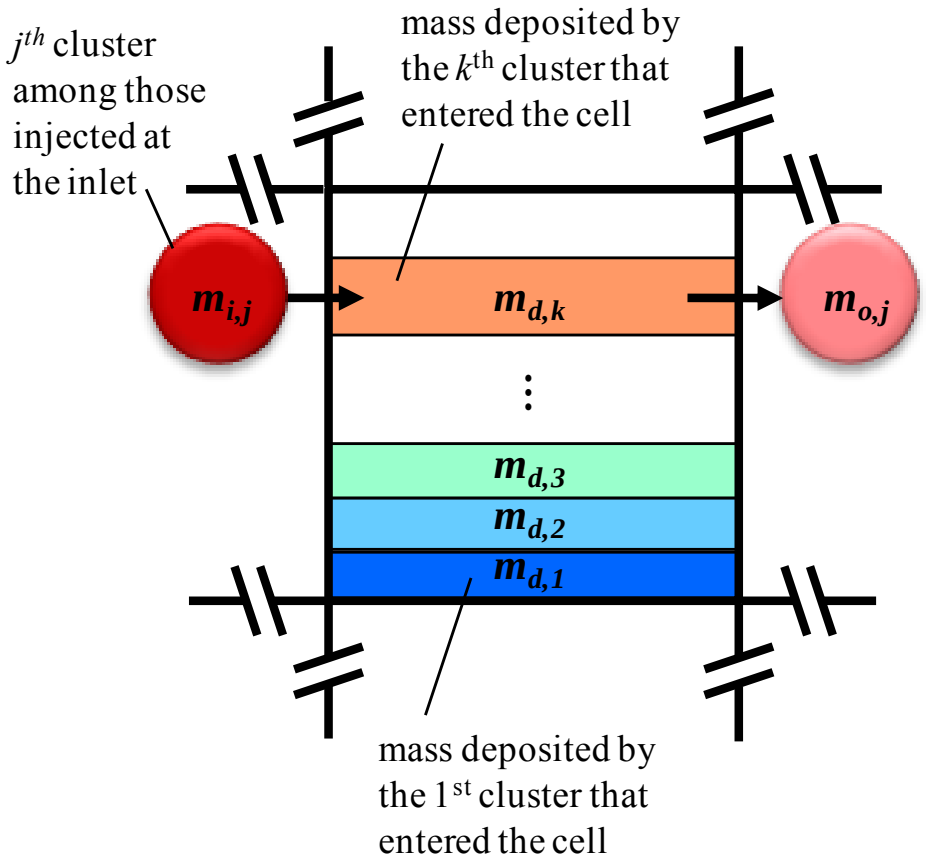

Figure 6.2: Schematic illustration of transient particle deposit increase inside a computational cell.

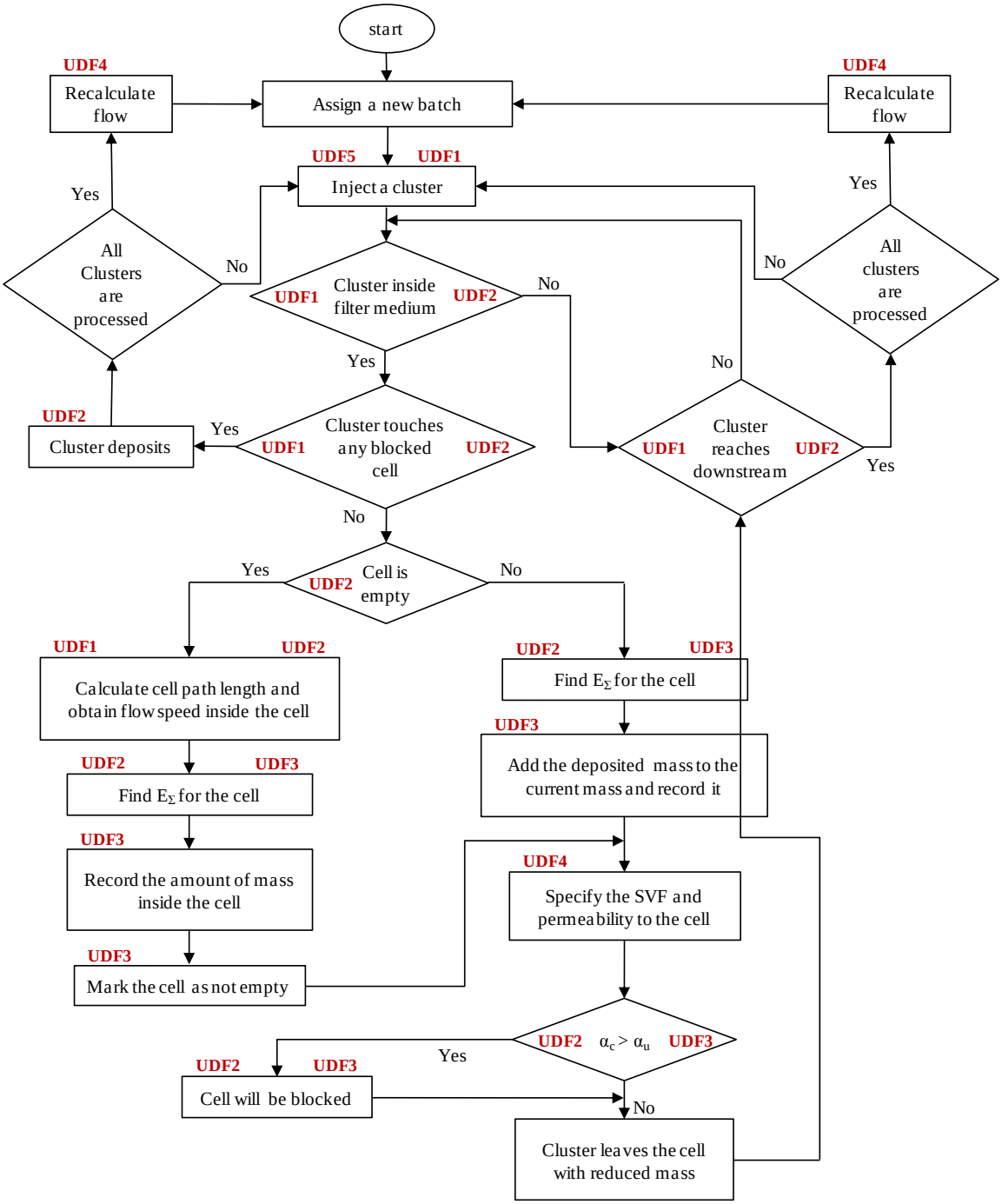

Figure 6.3: Numerical simulation flow chart. At each stage, the effective UDF has been mentioned.

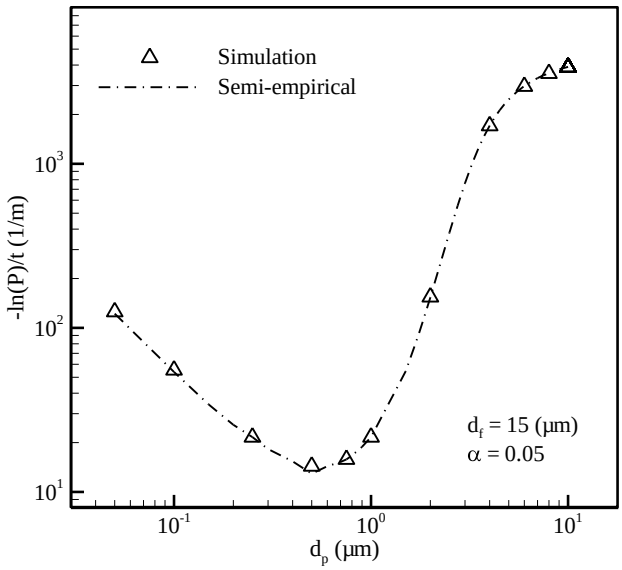

Figure 6.4: Comparison between our simulation outputs and the cell model semi-empirical equations for particle penetration through a clean fibrous medium. The cell model equations are shown in Chapter 1.

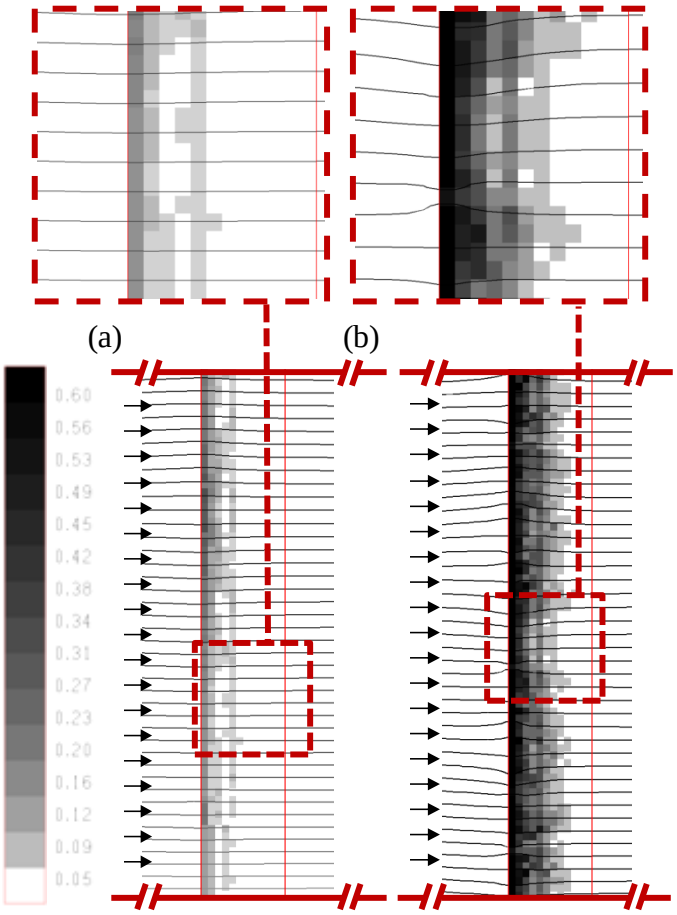

Figure 6.5: Contour plots of cell SVF together with air streamlines showing an example of particle deposition inside the fibrous zone at two different simulation times of $t = 40\,\text{s}$ (a), and $t = 180\,\text{s}$ (b). The simulations are conducted with a particle diameter of $d_p = 10\,\mu\text{m}$ at a speed of $u_{in} = 0.05$ m/s. The fibrous medium is assumed to have a SVF of 5% and a fiber diameter of $d_f = 15\,\mu\text{m}$ with the thickness of 0.7mm. Maximum allowable SVF is obtained accordingly from Equation 6.10.

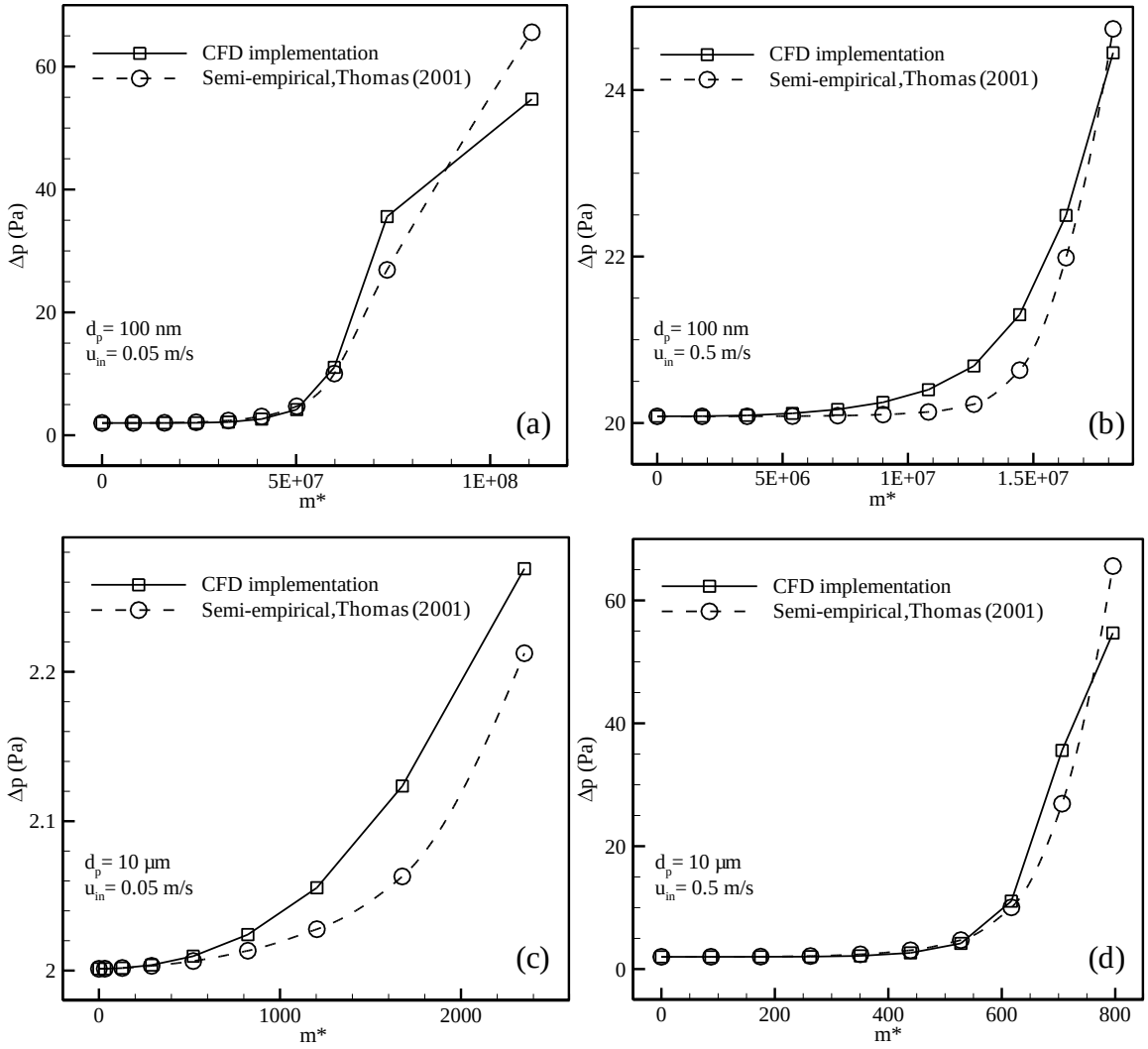

Figure 6.6: Comparison between our pressure drop predictions and those of the semi-empirical expression of Thomas *et al.* (2001) for fibrous flat sheets during dust deposition. The fibrous medium is assumed to have a SVF of 5%, a fiber diameter of $d_f = 15\,\mu\text{m}$, and a thickness of 0.7mm.

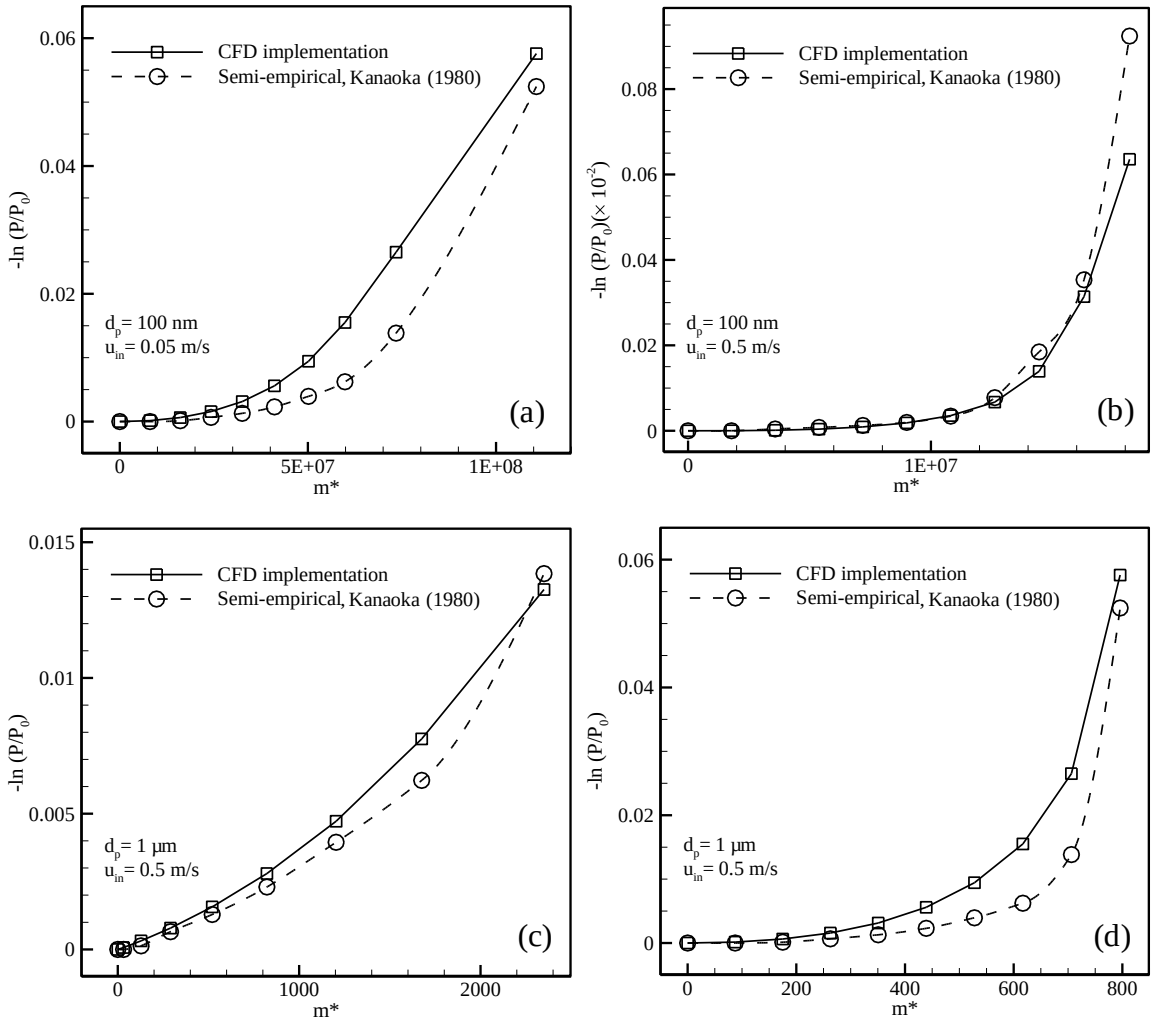

Figure 6.7: Our collection efficiency predictions are used along with the semi-empirical expression of Kanaoka *et al*. (1980) for particle penetration through fibrous flat sheets during dust deposition. The curve fitting parameters are (a) λ=5000, (b) λ=3000, (c) λ=250, and (d) λ=500. The fibrous medium is assumed to have a SVF of 5%, a fiber diameter of $d_f = 15\,\mu\text{m}$, and a thickness of 0.7mm.

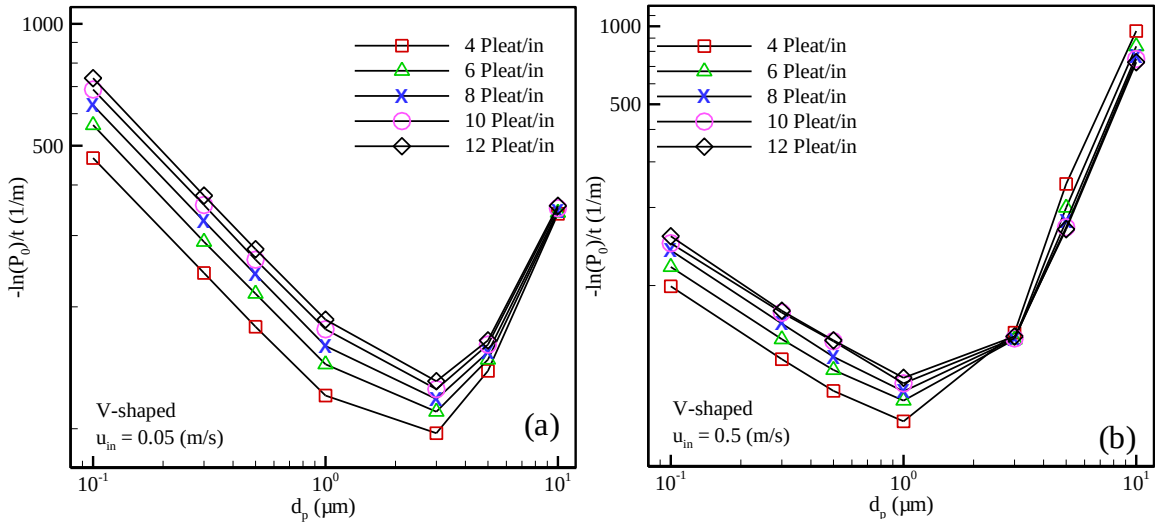

Figure 6.8: Particle penetration per thickness obtained for clean filters with different pleat counts at two different air inlet velocities of 0.05 and 0.5 m/s.

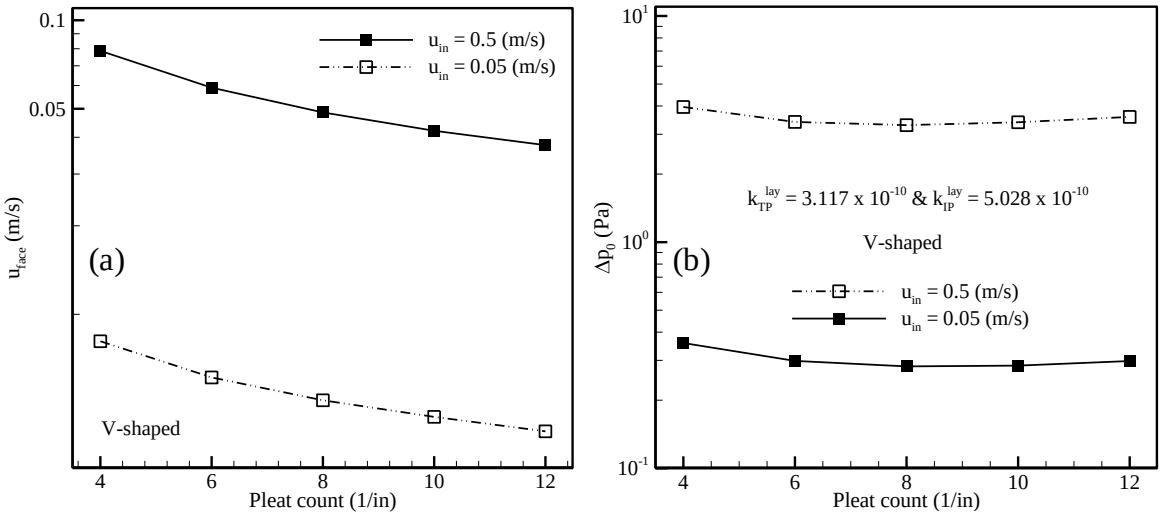

Figure 6.9: Effects of pleat count of the face velocity (a) and pressure drop (b) obtained for clean filters at two different air inlet velocities of 0.05 and 0.5 m/s. Fibrous media have a SVF of 5%, a fiber diameter of $d_f = 15\,\mu m$, a thickness of 0.7 mm.

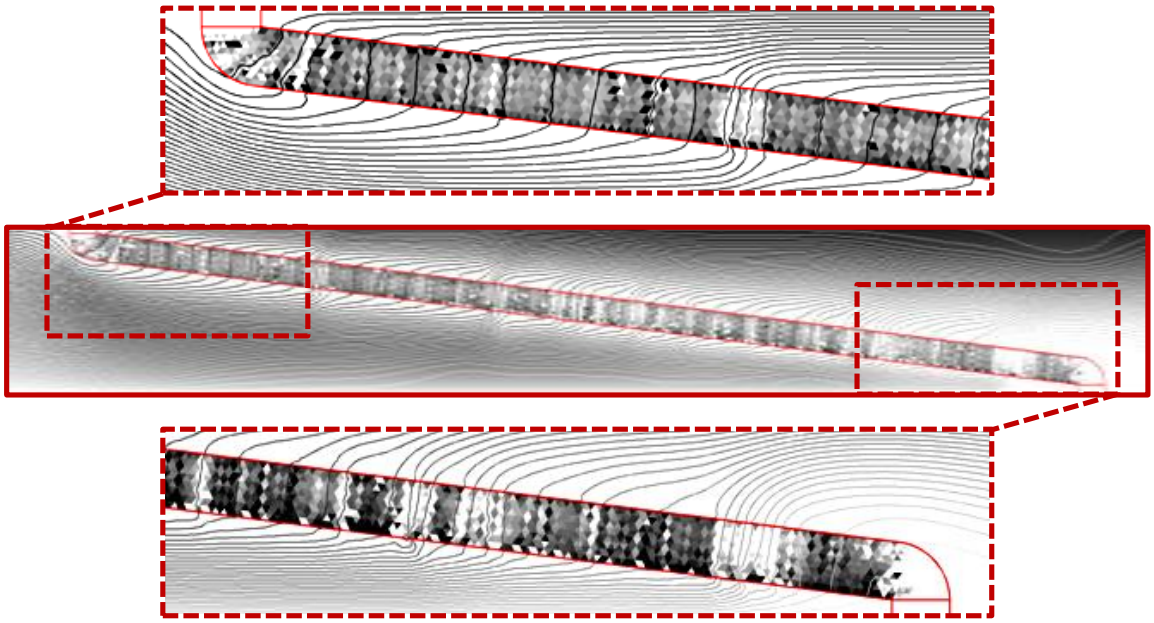

Figure 6.10: Contour plots of cell SVF together with air streamlines showing an example of particle deposition inside the fibrous zone in a pleated filter. The particle diameter and air inlet velocity are considered to be $d_p = 3\mu m$ and $u_{in} = 0.05$ m/s, respectively. Here SVF is 5%, fiber diameter is $d_f = 15$ µm, and thickness of 0.7 mm.

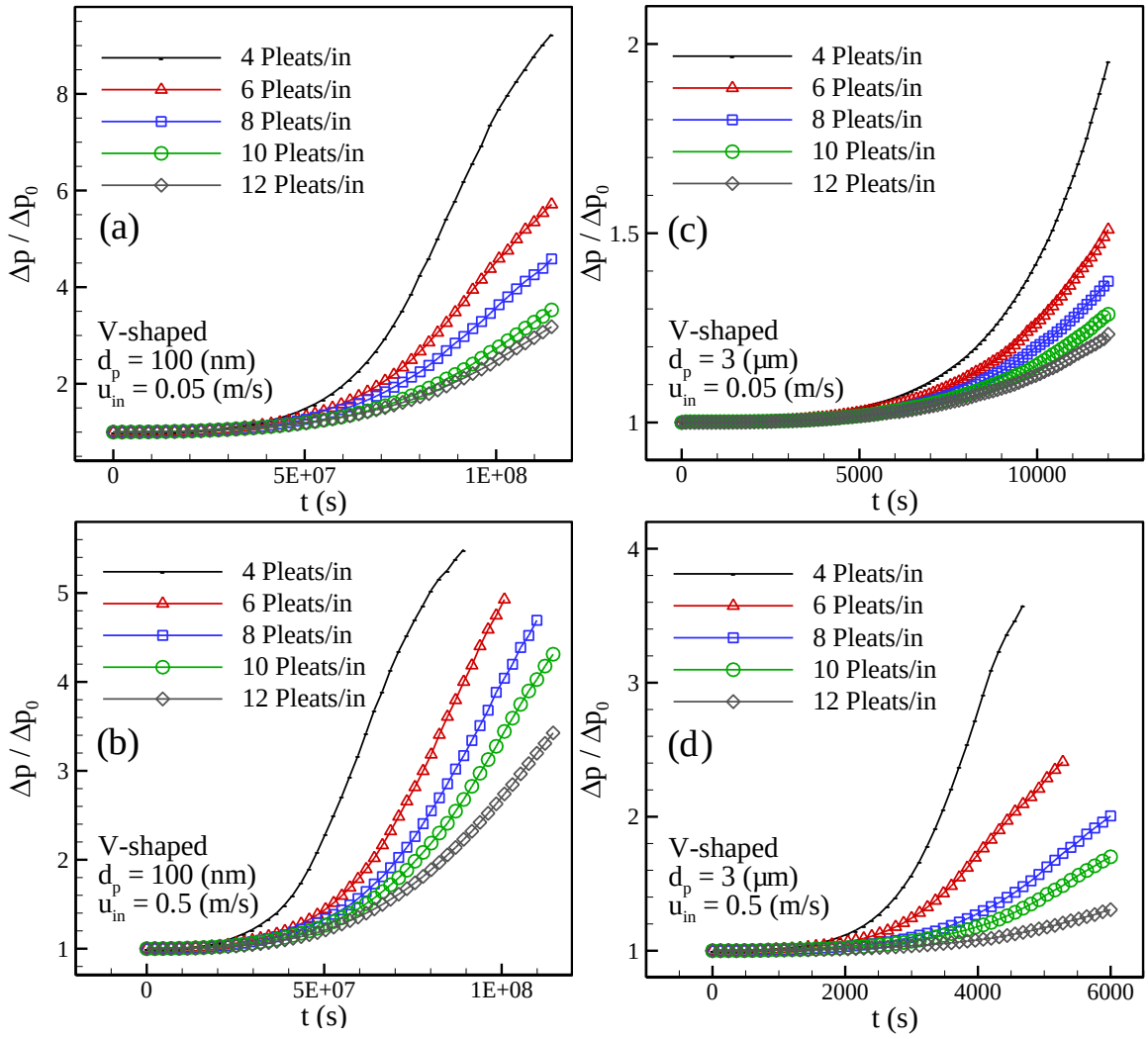

Figure 6.11: Instantaneous pressure drop versus time for two different particle diameters of 100 nm and 3μm, and at two different air inlet velocities of 0.05 and 0.5m/s.

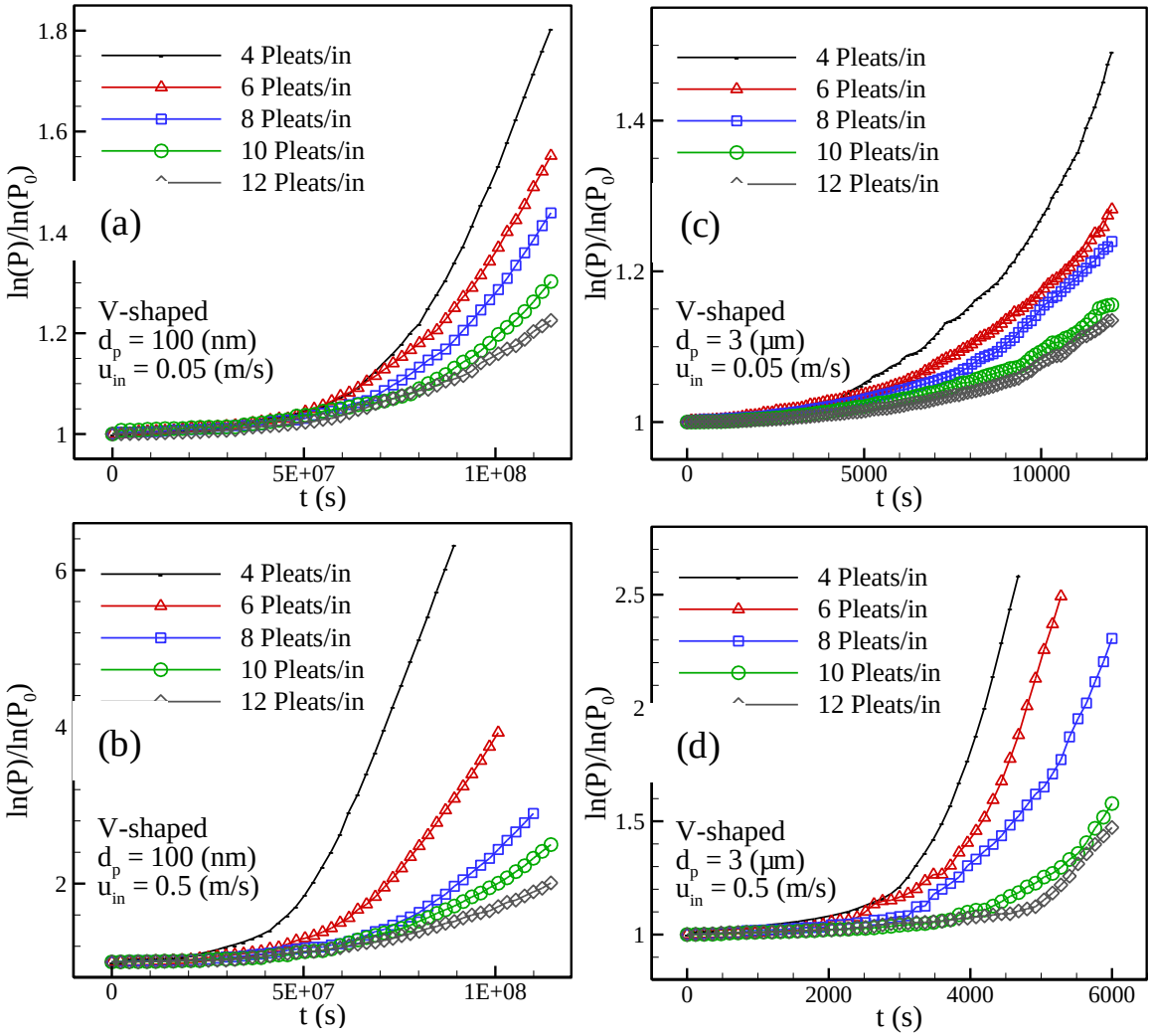

Figure 6.12: Instantaneous penetration versus time for two different particle diameters of 100 nm and 3μm, and at two different air inlet velocities of 0.05 and 0.5m/s.

CHAPTER 7 Macro-Scale Modeling of Pleated Filters Challenged with Poly-Disperse Aerosols[♣]

7.1 Introduction

Pleated filters are used in vast areas of application in automotive industry, HVAC systems, and clean rooms among many others, especially when high performance in aerosol filtration or compact design of filters is required. Controlling the air flow inside pleats is an essential consideration which leads to minimizing pressure drop and maximizing particle collection efficiency. as mentioned in previous two chapters, air flow control in pleated filters usually depends on two major contributors. As discussed earlier, one is the fibrous medium or flat sheet thin paper, which will be folded to make pleats. The second is the pleat geometry (i.e. pleat width, pleat height and pleat shape) which can influence the performance of the filter due to viscous effects. In addition, there is another factor involved which can affect filter performance and that is dust deposition. In general, most of the published research in studying pleated filters is concentrated on optimizing pleats to minimize pressure drop (the related works have been cited in Chapter 5). To date, there are no criteria for designing pleat shape and pleat count for optimizing both the pressure drop and collection efficiency. More importantly, the influence of particle loading (i.e., filter aging) on performance of fibrous filters has never been studied in the past. There only two

[♣] *Content of this section is currently in the final stages of preparation for submission to an engineering journal for publication.*

studies can be found: analytical work of Rebai *et al.*, (2010), our own works (Fotovati et al., 2011; this work was previously presented in Chapter 5). In our work the effects of micron-sized dust deposition on pressure drop of HEPA filters were simulated. In addition, we introduced a numerical scheme which allows obtaining the deposition pattern of the particles inside the fibrous filters (Fotovati et al., 2011, this work was previously presented in Chapter 6) and also studying the collection efficiency of pleated filters.

The first two aforesaid works are limited to some sort of simplifications and mainly covered surface deposition and monitored pleats pressure drop, while the latter is just proposing a methodology to model in-depth dust deposition and measure the collection efficiency of pleated filters. This part of the study, however, provides the most realistic and comprehensive study about the performance of pleated filters to date. In this chapter, we combine the depth and surface deposition and it is of the interest to investigate whether our achievements for surface-only deposition can be verified when depth deposition is included. We also allow the aerosol particles to be poly-dispersed in size and model their deposition pattern. We consider the fibrous structure as a lumped porous zone, and particles will be filtered inside the zone due to cell model equations for a fibrous domain. When there is a poly-dispersed surface dust cake however, we assume that the cake acts as a granular bed of spherical collectors (deposited particles in this case) and we therefore solve the related equations at the outside cake for particle filtration. In addition, we assume aerosol with range of particle-size distribution, and also, if it is acceptable, particles are allowed to penetrate into currently deposited dust cakes. This novel methodology provides

the most complete and general study about the performance of pleated filters under dust-load effects.

The flow field is modeled exactly the same fashion as we discussed in previous two chapters. To track the aerosol particles and determine their paths through the filter, we consider the same Lagrangian approach, introduced in previous chapter. Our particle trajectory modeling and flow calculations are performed by enhancing the Discrete Phase Model (DPM) of the ANSYS CFD code with our in-house subroutines (UDF's) that are executed in ANSYS's environment. The strategy for particle tracking (both for depth and surface deposition) is based on assigning a mass to each injected particle and monitoring the rate of deposition. This means that we considered each injected particle as a group of same size sub-particles (see Chapter 6 for more details).

7.2 Modeling of Dust Deposition

Instead of modeling Dust deposition inside the fibrous micro-structure, it is modeled while fibrous media are considered as lumped porous region (for simulation domain see Figure 6.1 from previous chapter). Therefore, the particles can deposit over time, and their permeability and collection efficiency would change as deposition occurs. In our simulations we calculate the amount of mass deposition inside each computational cell after each individual dust clusters pass across it, and the values for permeability would be updated for flow recalculation. In addition, when dust clusters leave the filter, the amount of mass which they carry is known and after all particles clusters are injected, the filter

penetration can be predicted inside simulation domain. The SVF for each cell is estimated by knowing the amount of deposited mass in that cell and its volume. The maximum allowable SVF (α_{max}) for each cell is found according to the deposited particle diameter in that cell using Equation 6.10 (Kasper et al., 2010). If the cell SVF is greater than the predicted value by equation 6.10, then this cell is impermeable to the incoming particles with diameter of d_p. The flow field must be recalculated after each batch injection. However, before flow recalculation, the permeability of the computational cells inside the fibrous domain should be updated. To do so, we assume that the deposited particles make a permeable granular medium around the fibers. For simplicity, we assume the fibrous and granular porous media to act like resistors in series (see Equations 6.8 and 6.9).

With mono-dispersed particles, all injected particles have identical diameter (d_p) and therefore, no further consideration regarding particle diameter is necessary. The particle tracking follows perfectly the steps presented in Figure 6.3 in previous chapter. First, particle clusters enter the fibrous domain, and the cell model equations for cylindrical fibrous structures are solved inside each computational cell using cell model equations introduced in Chapter 1. According to these calculations, the permeability change due to granular particle deposition inside the fibrous domain will be calculated and the directional permeability components related to the fibrous domain will be updated before flow recalculation. When a cell's SVF reaches to its maximum allowable value, then if any cluster touches this cell, all of its mass will deposit at once. This process will be taken

place until the cells adjacent to the filter surface are blocked. At this point, surface deposition starts.

With surface deposition starts, then any newly incoming particle is faced with the granular beds of previously deposited particles (granular filter). At this stage, we solve the cell model equations for granular collectors (equations A1–A5 in Appendix A) inside cells that contain deposited mass with the diameter of d_p. The cells' SVF will be assigned based on the deposited mass and whenever the SVF is greater than the maximum allowable value, the cell will be blocked and is not allowed to admit anymore particles.

7.3 Poly-Dispersed Particle Consideration

The main objective of this chapter is to study the influence of poly-dispersed dust deposition on the performance of pleated geometries. It is important to note that with polydisperse aerosol injection, particles may penetrate through already deposited cakes. To conduct this study, we need to assign an equivalent diameter for each cell, when different clusters with different diameters deposit inside it. A general definition for an average particle diameter is given as (Dullien, 1992):

$$\bar{d} = \frac{\left[\int_0^\infty d_p \, d_p^r \, n\ d_p\ \ d\ \ d_p \right]}{\left[\int_0^\infty d_p^r \, n\ d_p\ \ d\ \ d_p \right]} \qquad (7.1)$$

where $n\ d_p$ is the density function (number fraction) of each particle diameter. The value $r = 0$ gives the result for the number average diameter. For the value of $r = 2$, the

above expression gives the surface average, and with $r = 3$, it gives the volume average diameter. According to the works of Macdonald et al. (1979) and Rumpf and Gupte (1971), the best results are obtained by the surface averaging method (i.e. $r = 2$). Thus in the current work, we use this method to predict the average particle diameter inside each cell.

We assumed that inside each cell, we deal with two different particle sizes, an averaged diameter of already deposited particles in the cell ($\bar{d}_p$) and the diameter of currently incoming cluster (d_p). Therefore Equation 7.1 can be simplified to the following format:

$$\bar{d}_p = \frac{n_{\bar{d}_p} \cdot d_{\bar{d}_p}^3 + n_{d_p} \cdot d_{d_p}^3}{n_{\bar{d}_p} \cdot d_{\bar{d}_p}^2 + n_{d_p} \cdot d_{d_p}^2} \tag{7.2}$$

In above, $n_{\bar{d}_p}$ and n_{d_p} are the number fractions (density functions) for already deposited particles and incoming particle, respectively. To find these number fractions, we simply use the following:

$$\begin{cases} N_{\bar{d}_p} = \dfrac{\bar{m}_d}{m_{\bar{d}_p}} \\ N_{d_p} = \dfrac{m_{cl}}{m_{d_p}} \end{cases} \Rightarrow \begin{cases} n_{\bar{d}_p} = \dfrac{N_{\bar{d}_p}}{N_{d_p} + N_{\bar{d}_p}} \\ n_{d_p} = \dfrac{N_{d_p}}{N_{d_p} + N_{\bar{d}_p}} \end{cases} \tag{7.3}$$

Parameter N refers to the exact number of particles while n is their fractional value ($0 < n < 1$). Also note that $\bar{m}_d$ and m_{cl} are the cell's deposited mass and incoming cluster mass, while $m_{\bar{d}_p}$ is the mass of one single particle with the diameter identical to that of the

averaged deposited particle in each cell, and m_{d_p} is the mass of single particle inside the incoming cluster. Figure 7.1 shows these steps in a flow chart format. To add above considerations into our simulations, we modified our UDF for particle-tracking, in such a way that it checks for previously deposited mass inside each computational cell and assigns the average dust particle diameter to it, where this diameter will be considered as collector diameter in Equations A1–A4. Knowing incoming clusters' diameters, and their mass fractions, poly-dispersed dust deposition in pleated geometry can be modeled.

7.4 Results and Discussions

In the current work, we consider triangular (V-shaped) pleats with different widths (or angles) but an identical length of 25.4 mm (same as what we have shown in Figure 6.1). The pleat width is set in a sort of way that we model filters with 4, 8, and 12 pleats per inch. The fibrous medium is assumed to have a thickness of 0.7 mm, SVF of 7.5%, and fiber diameter of 15μm. Two different inlet air velocities of 0.05 m/s and 0.5 m/s with a constant aerosol number concentration of $C = 2\times10^{9}\,\mathrm{m}^{-3}$ are considered in this study. Note that the inlet velocity is the velocity of the air flow at the inlet to the filter package (or the duct in which the filter is mounted) and should not be confused with the face velocity, which is the air velocity as it enters the fibrous medium. Since our simulation domain is two-dimensional, we assume a unit length for the dimension perpendicular to the simulation plane (x-y plane). An equivalent particle concentration is obtained based on the concentration flux at each time. Note that each injection batch resembles a time interval

equal to one second. After each injection we recalculate the flow field and monitor and report the pressure drop and penetration changes. We injected particles with 1 and 10 micron in size as a sample for our mono-dispersed particle injection. To model poly-dispersed particle deposition, we used particles with size dispersion between 1μm and 10 μm follows a lognormal distribution with mean diameter of 4.53 μm and standard deviation of 0.733.

7.4.1 Mono-Dispersed Dust Loaded Filter Performance

At first our results for the effects of particles size and inlet velocity (inertia) on the performance of pleated filters are presented. . Figure 7.2a–b gives the dust pattern inside filters with 4, 8 and 12 pleats per inch for low and high inertial particles, respectively. In Figure 7.2a, low inertial particles with 1μm diameter and 0.05 $m.s^{-1}$ injection speed, shows a very uniform deposition, no significant dendrite has been observed and in addition, the depth deposition is not negligible as can be seen. Accordingly, no filter blocking can be detected. With high inertial particles injection (Figure 7.2b), the depth deposition is not dominant and surface deposition has been occurred faster compare to low inertial particle injection. As was expected, large dendrites have been formed and blocked the filter. Note that due to the random nature of dust injection, these dendrites may occur at any location over the pleat surface or at any time. These blocking inside the pleat channels can be detected faster when dealing with more number of pleats. Note that in this study, we did not take particles bouncing into account.

In Figures 7.3 and 7.4, we reported transient pressure drop and collection efficiency increase ratio during time. Each of our time steps represents one second, however, due to simulations artifact (i.e. filter geometry generation simplifications) we decided to report simulation times with an arbitrary unit. Figure 7.3a–b shows that filters with more number of pleats always has less pressure drop and collection efficiency increase ratio, when they are dealing with low inertial particles. Even though we let the simulations to continue for long simulating time, no blocking by dendrites has been observed. With higher inertial particles injection, as can be seen in Figure 7.3c–d, no significant change occurred compare to results of Figure 7.3a–b. The values for maximum pressure drop and collection efficiency increase ratio are significantly higher compare to very low inertial particles, and the reason is due to higher aerosol flux that is injected into filter at each time step. Filters with more number of pleats have higher pressure drop and collection efficiency increase ratio and our results are in complete agreement with our previous work (Fotovati et al., 2011). This trend cannot be observed as filter encounters with very highly inertial particles. As Figure 7.4a–b depicts, even after a very short while, the filter is getting blocked by dendrites and because this phenomenon happens faster for filters with higher number of pleats, therefore, they have higher pressure drop and collection efficiency ratio.

7.4.2 Poly-Dispersed Dust Loaded Filter Performance

The graphical demonstrations of particle deposition pattern have presented in Figure 7.5a–b. We let the simulations to run for 152000 time steps and as can be seen, regardless of

particle inertia, all of our simulations resulted in filter blocking by dust cake. In addition as can be seen in Figure 7.5, depth filtration is important as well. The reason can be defined regarding to the particles distribution. As is known, due to log-normal distribution, in each injection batch there are a greater number of fine particles than large size particles, and as we discussed in previous section, with smaller particle size, depth filtration must be considered.

Figure 7.6a–b shows the increase ratio for filter pressure drop and collection efficiency for filter faces with low inertial particles injection. As can be seen, unlike pressure drop, the collection efficiency increase ratio is higher when filter comprises of fewer number of pleats. The reason can be related to the importance of particles' size distribution. Although number fraction of small size particles is higher, mass fraction of the large size particles is dominated. Therefore, with less number of pleats, filters are associated with higher values of face velocity and therefore, collection efficiency increase ratio remains higher with filters with less number of pleats. It was mentioned that respect to low inertial particles, and due to our filter flat sheet parameters, the depth-deposition is also important because of low filter efficiency for low inertial particles (see Figures 7.3b and d). Therefore, when filter has more number of pleats per inch, this means that face velocity is lower, and particles arrive into the fibrous domain with lower velocity. Conclusively, the filter collects low inertial particles with higher performance. Figure 7.6c–d, presents the performance of filters for the same particle distribution (as for the case in Figure 7.6a–b) but with higher inlet speed. Again, when one wants to monitor the pressure drop increase

ratio, it can be seen that filters with higher number of pleats get blocked faster and therefore, higher values for pressure drop can be obtained. In addition, with the identical elapsed time steps, the pressure drop increase ratio of filters which operate under higher flow rate is higher, which is an expected fact. In Figure 7.6d, again, due to more mass fraction of particles with larger diameter at injection, unlike the pressure drop, more number of pleats causes filter to have lower efficiency increase ratio. Also, the comparison between Figures 7.6b and d, shows that at the same number of pleats, filter performs better (i.e. it has lower pressure drop and higher collection efficiency increase ratio) when it encounters lower inertial particles.

7.5 Conclusions

As an extension to our previous publications on the pleated filters subject, we conducted the most realistic numerical study for the pleated filters, while they encounter particle surface and depth deposition altogether. In addition, our model considered poly-dispersed particle deposition as well.

We showed that depth filtration should not be neglected when filter has low collection efficiency due to low inertial (Stokes number) particle at injection. It has been demonstrated that low inertial particles deposits inside the fibrous domain and therefore, filters are not getting blocked by dust cake, regardless of the number of pleats.

For the case of mono-dispersed particles, with low inertial particles (low Stokes number), more number of pleats always result in lower pressure drop and collection efficiency increase ratio. In contrast, when filter encounters with highly inertial particles, then more number of pleats causes

filter to get blocked faster if the filter is exposed to aerosol for enough time. In this work we also proposed a methodology to model poly-dispersed particle deposition in pleated filters. When particles are poly-dispersed in size with log-normal distribution, then although each injection batch of particles contains more number of small size particles, the mass fraction of larger particles is higher and therefore, they will be collected better via filters with less number of pleats respect to higher face velocity. However, due to the existence of low inertial (Stokes number) particles, the dust depth deposition is observed. Also we showed that in the presence of filter blocking, those with less number of pleats perform better in having higher collection efficiency and lower pressure drop increase ratio.

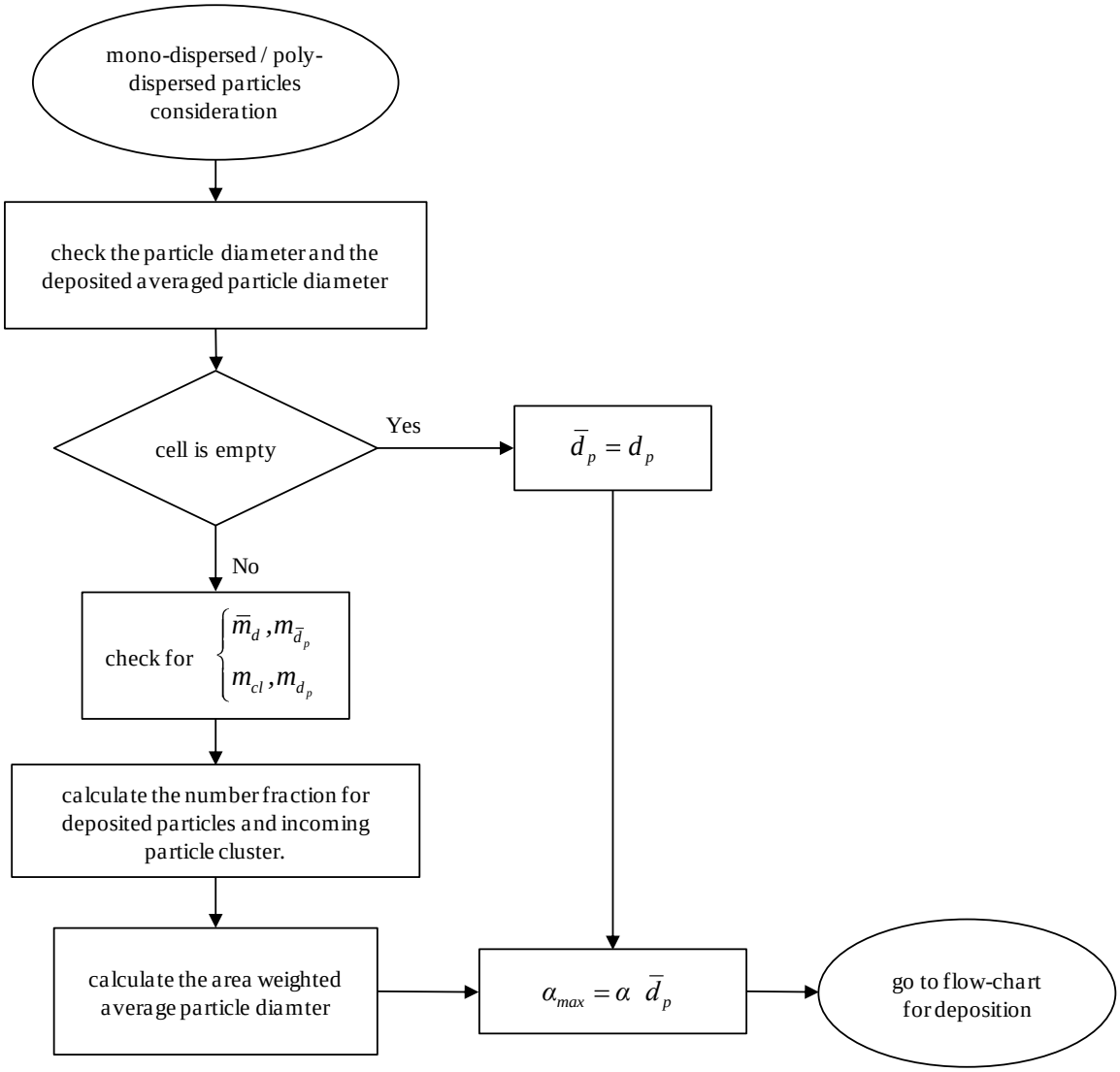

Figure 7.1: Flow chart which describes poly-dispersed particle deposition.

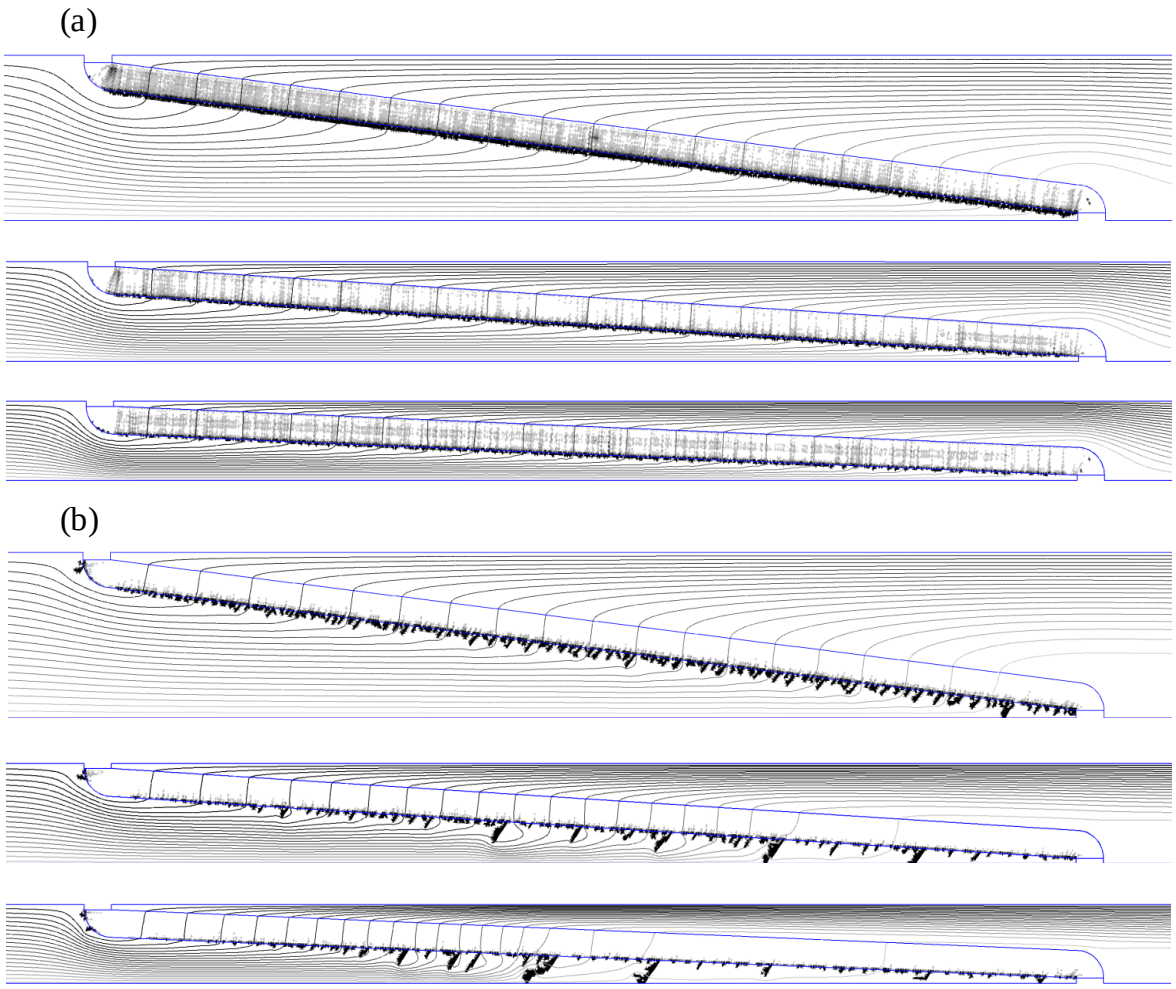

Figure 7.2: Graphical demonstration for mono-dispersed dust deposition pattern inside filters 4, 8 and 12 pleats/in with (a) 1µm particles and 0.05 $m.s^{-1}$ inlet velocity and, (b) 10µm particles and 0.5 $m.s^{-1}$ inlet velocities.

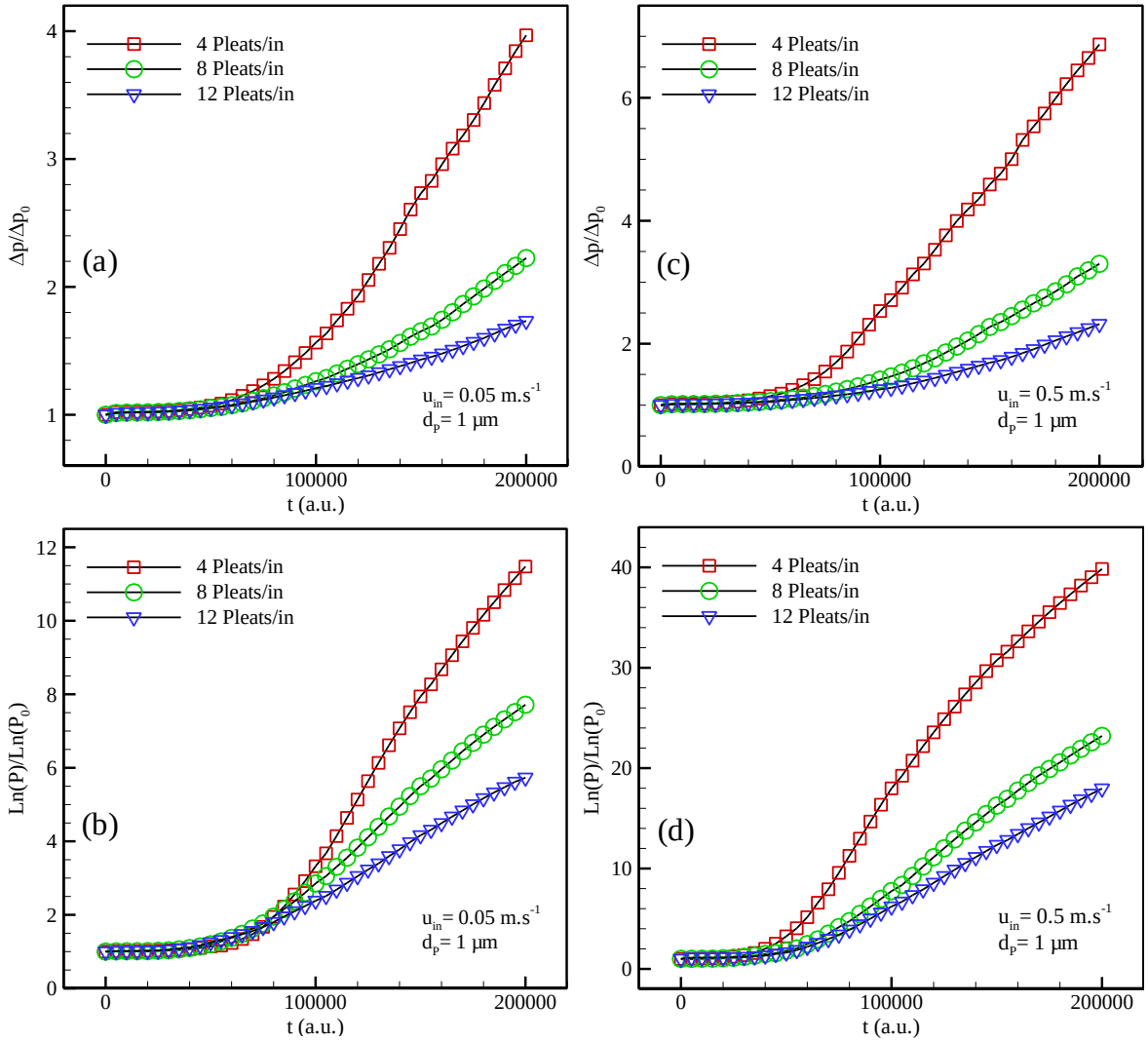

Figure 7.3: Performance of filters with 4, 8, and 12 pleats/in with 1μm particles (a) Pressure drop increase ratio for 0.05 $m.s^{-1}$ inlet velocity. (b) Collection efficiency increase ratio for 0.05 $m.s^{-1}$ inlet velocity. (c) Pressure drop increase ratio for 0.5 $m.s^{-1}$ inlet velocity. (d) Collection efficiency increase ratio for 0.5 $m.s^{-1}$ inlet velocity.

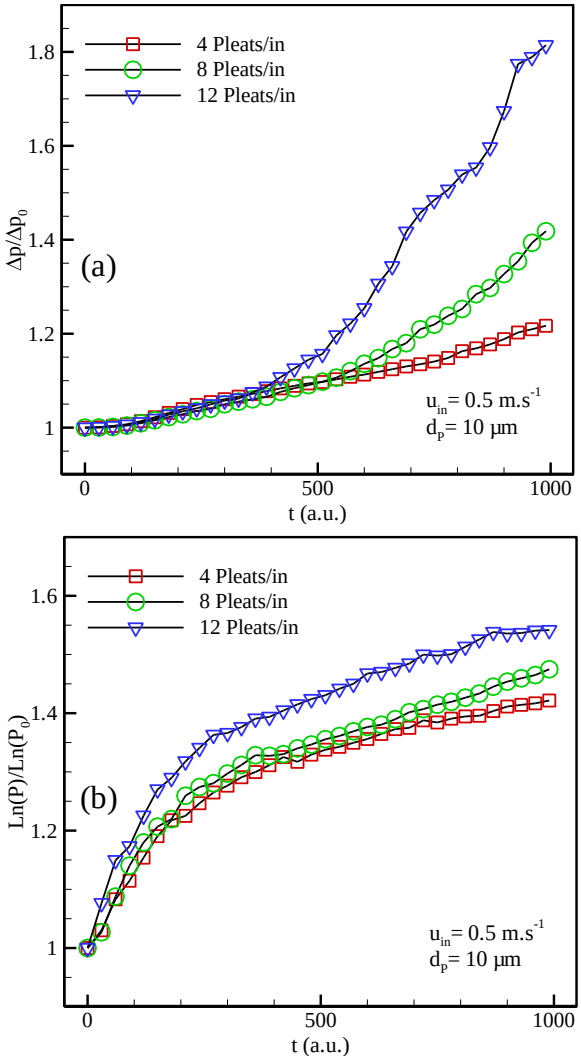

Figure 7.4: Performance of filters with 4, 8, and 12 pleats/in with 10µm particles and 0.5 $m.s^{-1}$ inlet velocities. (a) Pressure drop increase ratio. (b) Collection efficiency increase ratio.

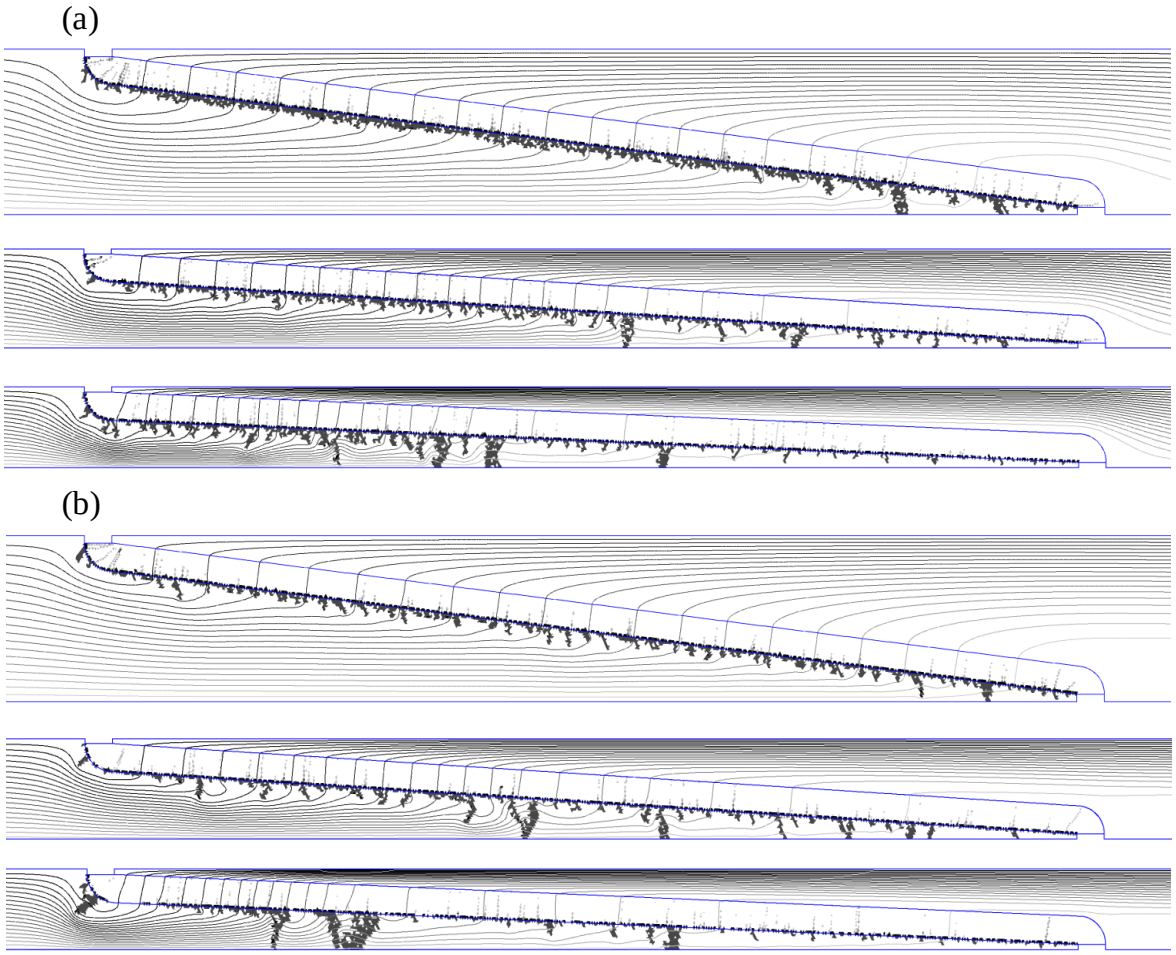

Figure 7.5: Graphical demonstration for poly-dispersed dust deposition pattern inside filters 4, 8 and 12 pleats/in with 1–10μm particles distribution for (a) 0.05 $m.s^{-1}$ inlet velocity and, (b) 0.5 $m.s^{-1}$ inlet velocity.

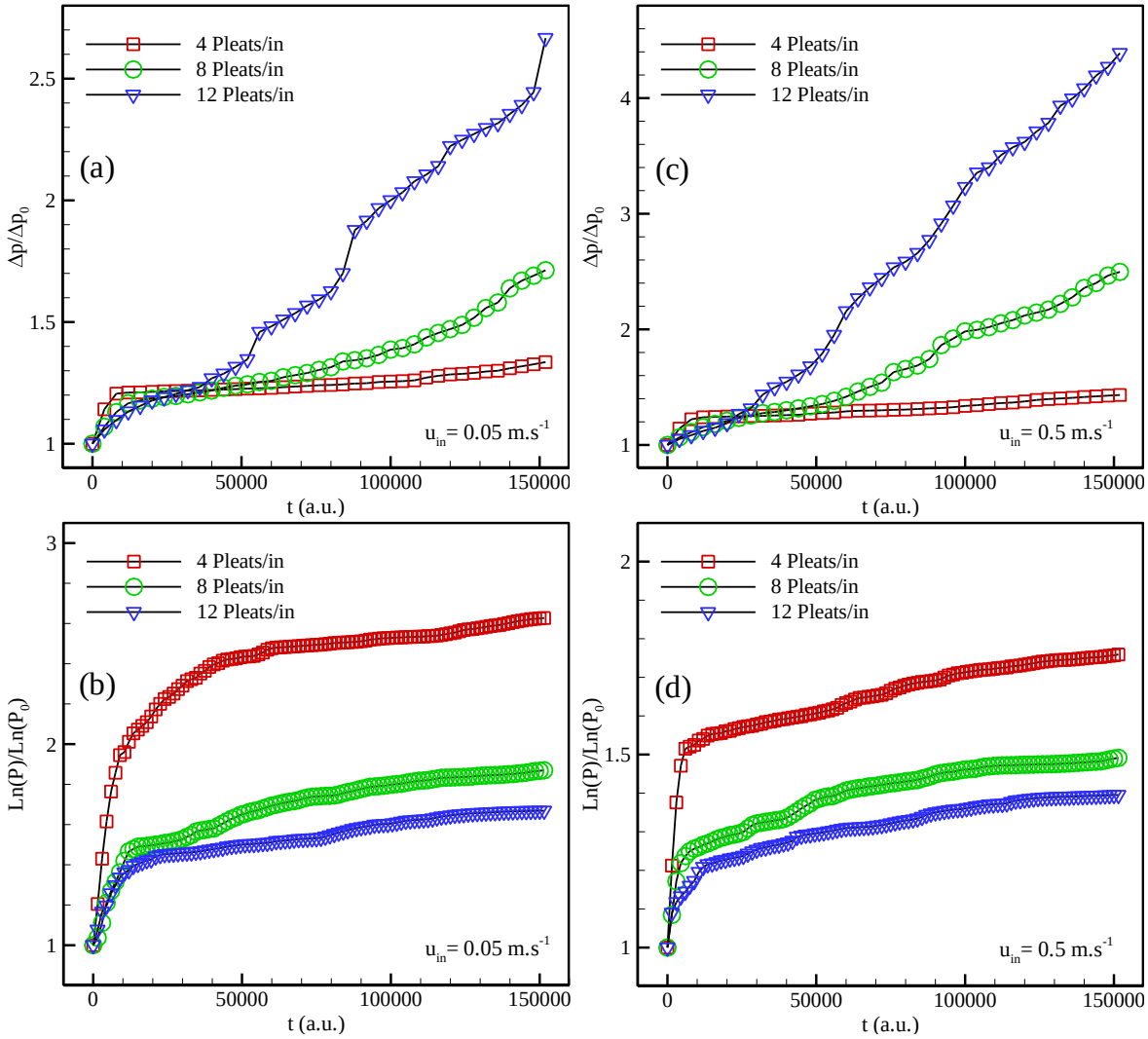

Figure 7.6: Performance of filters with 4, 8, and 12 pleats/in with poly-dispersed particles (a) Pressure drop increase ratio for 0.05 $m.s^{-1}$ inlet velocity. (b) Collection efficiency increase ratio for 0.05 $m.s^{-1}$ inlet velocity. (c) Pressure drop increase ratio for 0.5 $m.s^{-1}$ inlet velocity. (d) Collection efficiency increase ratio for 0.5 $m.s^{-1}$ inlet velocity.

CHAPTER 8 Overall Conclusions

This dissertation is intended to model the effects of micro-scale geometric parameters on the performance of fibrous structures and propose a method to use them to study the effects of the macro-scale geometric parameters on the performance of pleated filters. Our micro-scale simulations (Chapters 2–4) are comprised of a series of computational fluid dynamics calculations conducted in virtual fibrous geometries that resemble the internal micro-structure of a fibrous medium. These simulations were conducted to isolate the effects of each microstructural parameter (e.g., fiber diameter, fiber orientation, fiber cross-sectional shape, and porosity) and study its influence of the performance of the filter medium. In our macro-scale simulations (Chapters 5–7), the filter medium is treated as a lumped porous material with its properties obtained via the results of the micro-scale simulations. The macro-scale model is developed to simulate the unsteady-state performance of pleated filters, and study the importance of their macro-scale dimensions (e.g., pleat shape, pleat height, and pleat count).

While analytical expressions are available for the predicting performance of filters made up of fibers with a unimodal distribution, there are few equally simple relations for bimodal/multimodal filters. A series of numerical simulations were therefore formulated for studying the performance of filter media with bimodal fiber diameter distributions. The results were then utilized to establish an equivalent diameter for the bimodal media,

thereby taking advantage of the existing expressions for unimodal filters. Our results indicate that the cube root relation of Tafreshi *et al*. (2009) offers the closest predictions for the range of consideration for particle diameter, fiber number (mass) fractions, fiber diameter ratio, and solid volume fraction (SVF). Another part of our micro-scale study was conducted to better understanding of the influence of fibers' in-plane and through-plane orientations on the performance of fibrous media. Our results indicate that pressure drop of common fibrous filters is independent of the in-plane orientation of the fibers, but decrease with increasing the fibers' through-plane orientation. More interestingly, it was found that filters with higher through-plane fiber orientations have a higher Figure of Merit if challenged with nano-particles. The Figure of Merit of these media, however, decreases as the particle size increases, reversing the effect of fibers' through-plane orientation. It was also shown that when the diameter of the particles is comparable to that of the fibers, collection efficiency increases with decreasing the fibers' in-plane orientation, while the pressure drop remains almost unchanged.

As mentioned, no mathematical formulations have yet been developed to predict the performance of non-circular fibrous media. In this study, trilobal fibers with different dimensions and aspect ratios were considered to study performance of filters made of such fibers. More importantly, the above information was utilized to define an equivalent medium with circular fibers. Our results indicate that the circumscribed circle of a trilobal fiber can serve as an equivalent circular diameter, and thereby be used in the existing semi-empirical correlations for predicting performance of filters with circular fibers. We have

also proposed easy-to-use expressions that can be used with our equivalent circumscribed diameters for calculating the pressure drop of trilobal media.

While micro-scale simulations are accurate and most realistic, they are computationally very expensive, and cannot be utilized to simulate a filter on scales comparable to its actual dimensions. Therefore, we developed a novel macro-scale model that can incorporate micro-scale information in cost-effective calculations performed for the filters in their actual dimensions. Pleat optimization has been of particular interest in this study. We considered three different classes of filters: 1) HEPA filters (performing as surface filters); 2) pre-filters (performing as depth filters); and 3) intermediate filters (performing at a level between the above two extremes).

For HEPA pleated filters with the presence of dust surface deposition, it was found that the rate of increase of pressure drop decreases with increasing the pleat count. Especially when particles are sufficiently large, the dust cake tends to form deeper inside the pleated channel when the pleat count is high. We also observed that rectangular pleats are preferred over the triangular pleats when the particles are highly inertial, i.e., filtering high-speed large particles.

To model pre-filters, a computationally affordable macro-scale method was developed to simulate the instantaneous performance of these aerosol filters. Our results indicate that increasing the number of pleats reduces the rate of increase of a filter's pressure drop and

capture efficiency. Predictions of our model are compared against available experimental data, and good agreement has been observed.

At last, we enhanced the above algorithms to model filters that do not necessarily perform as a perfect depth or a perfect surface filter. For the case of mono-dispersed low-inertia particles, more number of pleats always results in lower pressure drop and collection efficiency increase. In contrast, when a filter encounters with highly inertial particles, then more number of pleats causes the filter to clog faster. When particles are poly-dispersed in size, then the aerosol contains higher mass fraction due to large size particles, and therefore, fewer number of pleats shows better performance.

Literature Cited

References

Banks, D.O., 1987. Stokes flow through a system of parallel infinite cylinders with axes oriented at angle top the direction of mean flow. Particulate Science and Technology 5, 339-353

Banks, D.O, Kurowski, G.J, Whitaker, S., 1990. Diffusion deposition on a fiber in non-transverse flow. 2nd World congress: Particle Technology.

Batel, W., 1959. Chemie Ingenieur Technik, 31, 388.

Brown, R.C., 1993. Air filtration. Pergamon Press.

Brown, R.C. and Thorpe, A., 2001. Glass-fiber filters with bimodal fiber size distributions. Power Technology. 118, 3.

Caesar, T., Schroth, T., 2002. The influence of pleat geometry on the pressure drop in deep –pleated cassette filters. Filtration and Separation 39 (9), 48-54.

Chen, C.W., Huang1, S.H., Chiang, C.M., Hsiao, T.C., Chen, C.C., 2008. Filter quality of pleated filter cartridges, Annual Occupation Hygiene, 52, 3, 207–212.

Chen, D.R., Pui, D.Y.H., Liu, B.Y.H., 1995. Optimization of Pleated Filter Designs Using a Finite-Element Numerical Model. Aerosol Science and Technology 23 (4), 579-590.

Clague, S.D. and Phillips, R.J. (1997) A numerical calculation of the hydraulic permeability of tree dimensional disordered fibrous media. Physics of Fluids. 9 (6), 1562.

Davies, C.N., 1973. Air Filtration. Academic Press, London.

Del Fabbro, L., Laborde, J.C., Merlin, P., Ricciardi, L., 2002. Air flows and pressure drop modeling for different pleated industrial filters. Filtration and Separation 39 (1), 48-54.

Dhaniyala S., Liu, B.Y. H., 1999. "An asymmetrical, three-dimensional model for fibrous filters. Aerosol Science and Technology 30 (4), 333-348.

Doganoglu, Y., Jog, V., Thambimuthu, K.V., Clift, R., 1978. Removal of fine particles from gases in fluidized beds. Transactions of the Institution of Chemical Engineering 56: 296.

Drummond, J.E. and Tahir, M.I. (1984) Laminar viscous flow through regular arrays of parallel solid cylinders. International Journal of Multiphase Flow. 10, 515.

Dullien, F.A.L., 1992. Porous Media, Fluid Transport and Pore Structure. Academic Press Inc. 2nd edition.
Friedlander, S.K., 2000. Smoke, Dust, and Haze: Fundamentals of Aerosol Dynamics, 2nd edition Oxford University Press.

Fotovati, S., Tafreshi, H.V., Pourdeyhimi, B., 2010. Influence of fiber orientation distribution on performance of aerosol filtration. Chemical Engineering Science. 65 (18): 5285-5293.

Fotovati, S., Hosseini, S.A., Tafreshi, H.V., Pourdeyhimi, B., 2011. Modeling instantaneous pressure drop of pleated thin filter media during dust loading. Chemical Engineering Science. 66: 4036–4046.

Fotovati, S., Tafreshi, H.V., Pourdeyhimi, B., 2012. Modeling instantaneous pressure drop of pleated thin filter media during dust loading. Separation and Purification Technology (submitted).

Happel, J., 1959. Viscous flow relative to arrays of cylinders. A.I.Ch.E. Journal 5 (2), 174-177.

Henry, F.S., Ariman T., 1983. Particulate science and technology, 1, 1-20.

Hoffmann, A.C., Finkers, H.J., 1995. A relation for the void fraction of randomly packed particle beds. Powder Technology 82 (2), 197-203.

Hosseini, S.A., Tafreshi, H.V., 2010. Modeling Permeability of 3-D Nanofiber Media: Effects of Slip

Jackson, W.G. and James, F.D., 1986. The permeability of fibrous porous media. The Canadian Journal of Chemical Engineering. 64, 364.

Jaganathan, S., Tafreshi, H.V. and Pourdeyhimi, B., 2008. On the Pressure Drop Prediction of Filter Media with Bimodal Fiber Diameter, Powder Technology. 181, 89.

Kasper, G., Schollmeier, S., Meyer, J., 2010. Structure and density of deposits formed on filter fibers by inertial particle deposition and bounce. Journal of Aerosol Science 41(12), 1167-1182.

Koponen, A., Kandhai, D., Hellen, E., Alava, M., Koekstra, A., Kataja, M., Niskanen, K. Sloot, P., Timonen, J., 1998. Permeability of three dimensional random fiber webs. Physical Review Letters 80(4), 716-719.

Kuwabara, S., 1959. The forces experienced by randomly distributed parallel circular cylinders of spheres in a viscous flow at small Reynolds number. Journal of the Physical Society of Japan 14 (4), 527-532.

Lamb, G.E.R., and Costanza, P.A., 1980. Influences of Fiber Geometry on the Performance of Non-Woven Air Filters: 3. Cross-Sectional Shape, Text. Res. J. 50 (6) 362-370.

Lee, K.W., Gieseke, J.A., 1980. Note on the approximation of interceptional collection efficiencies, J. Aerosol Sci. 11, 335-341.

Lee, K.W., Liu, B.Y.H., 1982. Theoretical study of aerosol filtration by fibrous filters, Aerosol Sci. Tech. 1, 147-161.

Li, A., Ahmadi, G., 1992. Dispersion and deposition of spherical-particles from point sources in a turbulent chemical flow. Aerosol Science and Technology 16 (4), 209-226.

Liu, B.Y.H., Rubow, K.L., 1990. Efficiency, pressure drop and figure of merit of high efficiency fibrous and membrane filter media, Fifth World Filtration Conference, Nice, France (1990).

Lucke, T., Fissan, H., 1996. The prediction of filtration performance of high efficiency gas filter elements, Chemical Engineering Science 51 (8), 1199-1208.

Lundstrom, S.T., Gebart, G.B., 1995. Effect of perturbation of fiber architecture on permeability inside fiber tows. Journal of Composite Materials. 29, 424.

Macdonald, I.F., El-Sayed., M.S., Mow., K., Dullien F.A.L., 1979. Flow through porous-media - ergun equation revisited. Industrial and Engineering Chemistry Fundamentals, 18 (3), 199-208.

Mattern, J.K., Deen, M.W., 2008. Mixing rules for estimating the hydraulic permeability of fiber mixtures. AIChE Journal. 54, 32.

Papathanasiou T.D., 2001. The hydraulic permeability of periodic arrays of cylinders of varying size. Journal of Porous Media. 4(4), 323.

Payet, S., 1991. Filtrationstationnaire et dynamique des aerosols liquids submicroniques, These de l'universite Paris XII4 oct., 150 p., rapport CEA-R-5589.

Pich, J., 1965. The filtration theory of highly dispersed aerosols, Staub Reinhalt. Luft. 5, 16-23.

Pich, J., 1966. In aerosol science C. N. Davis, Academic Press, New York.

Rebai, M., Prat, M., Meireles, M., Schmitz, P., Beclet, R., 2010. Clogging modeling in pleated filters for gas filtration, Chemical Engineering Research and Design 88 (4A), 476-486.

Rao, N., Faghri, M., 1988. Computer modelilng of aerosol filtration by fibrous filters. Aerosol Science and Technology, 8 (2) 133-156.

Raynor, P.C., Kim, S.W., 2004. CFD modeling of filter fibers with non-circular cross-sections, AAAR conference, Atlanta.

Raynor, P.C., Chae, S.J., 2005. The Long-Term Performance of Electrically Charged Filters in a Ventilation System, Journal of Occupational and Environmental Hygiene, 1, 463–471.

Rumer, R.R., 1962. Proc. ASCE, Journal of Hydraulics Division, 88 (4) 147.

Rumpf, H., Gupte, A.R., 1971. Influence of porosity and particle size distribution in resistance law of porous flow. Chemie Ingenieur Technik, 43 (6) 367.

Sanchez, J.R., Rodriguez, J.M., Alvaro, A., Estevez, A.M., 2007. The capture of fly ash particles using circular and noncircular cross-section fabric filters, Environ. Prog. 26 (1) 50-58.

Schweers, E., Loffler F., 1994. Realistic modeling of the behaviour of fibrous filters through consideration of filter structure. Powder Technology 80, 191-206.

Sirkar, K.K., 1975. Transport in packed beds at intermediate Reynolds numbers. Ind. Eng. Chem. Fundam. 14: 73.

Spielman, L., Goren, S.L., 1968. Model for predicting pressure drop and filtration efficiency in fibrous media, Environmental Science and Technology 2, 279.

Stechkina, I.B., 1969. Diffusion precipitation of aerosols in fiber filters, Dokl. Acad. Nauk. SSSR. 167, 1327.

Stechkina, I.B., Kirsch, A.A., Fuchs, N.A., 1969. Studies on fibrous aerosol filters- IV. Calculus of aerosol deposition in model filters in the region of maximum penetration. Ann. Ocup. Hyg. 12,1-8

Subrenat, A., Bellettre, J., Cloirec, P.L., 2003. 3-D numerical simulations of fows in a cylindrical pleated filter packed with activated carbon cloth, Chemical Engineering Science 58, 4965 – 4973.

Tafreshi H.V., Rahman M.S.A., Jaganathan S., Wang Q., Pourdeyhimi B., 2009. Analytical Expressions for predicting permeability of bimodal fibrous porous media. Chemical Engineering Science. 64, 1154.

Tahir, M. A., Tafreshi, H. V., 2009. Influence of fiber orientation on the transverse permeability of fibrous media, Physics of Fluids 21, 083604.

Spurny, K.R., 1998. Advances in aerosol filtration, Lewis Publisher, CRC Press LLC: 471.

Thomas, D., Penicot, P., Contal, P., Leclerc, D., Vendel, J., 2001. Clogging of the fibrous filters by solid aerosol particles experimental and modelling study. Chemical Engineering Science 56 (11), 3549-3561.

Tien, C., 1989. Granular filtration of aerosols and hydrosols, *Butterworths*, Boston.

Tronville, P., Sala, R., 2003. Minimization of resistance in pleated-media air filter design: empirical and CFD approach, HVAC&R Reasearch, 9, 1, 95-106.

Waghode, A.N., Hanspal, N.S., Wakeman, R.J., Nassehi, V., 2007. Numerical analysis of medium compression and losses in filtration area in pleated membrane cartridge filters, Chemical Engineering Comm., 194, 1053–1064.

Wakeman, R.J., Hanspal, N.S., Waghode, A.N., and Nassehi, V., 2005. Analysis of pleat crowding and medium compression in pleated cartridge filters, Chemical Engineering Research and Design, 83(A10), 1246–1255.

Wang, Q., Maze, B., Tafreshi, H.V., Pourdeyhimi, B., 2007. Simulating through-plane permeability of fibrous materials with different fiber lengths. Modeling and Simulation in Materials Science and Engineering 15(8), 855-868.

APPENDIX A: Granular Filtration

The three major particle capture mechanisms mentioned in Appendix A have been developed and presented for fibrous media. To predict the capture mechanisms due to Diffusion in granular beds for a single collector, we used the work of the following expression (Spurny, 1998):

$$E_D = 4\, g\ \varepsilon\ Pe^{2/3} \qquad \text{(A1)}$$

In above, Pe is the Peclet number and $g\ \varepsilon$ is the correction factor. To obtain the capture efficiency due to interception with Reynolds number less than 1, we used the following:

$$E_R = 1.5\, g^3\ \varepsilon\ R^2 \qquad \text{(A2)}$$

The correction factor $g\ \varepsilon$ for the range of granular collectors (previously deposited particles) in this study is as following (Sirkar, 1975):

$$g\ \varepsilon = \left\{ \left[2 + 1.5\ 1-\varepsilon\ + 1.5 \left[8\ 1-\varepsilon\ - 3\ 1-\varepsilon\ ^2 \right]^{0.5} \right] \Big/ \varepsilon \left[2 - 3\ 1-\varepsilon\ \right] \right\}^{1/3} \qquad \text{(A3)}$$

Equation B3 is valid when the granular collector has $Re < 1$, with cell porosity ε of greater than 0.33 and Peclet number greater than 1000. Finally, for the SFE due to inertial impaction, we used the equation offered by Doganoglu (1978) and modified it for the range of our collector and particles sizes:

$$E_I = 2.89 \times Stk \times \gamma \qquad \text{(A4)}$$

$Stk = \frac{\rho_P d_P^2 c^c u}{18 \mu d_f}$ is the particles Stokes number. Note that $\gamma = 0.00318 Stk^{-1.248}$ is the correction factor. It has been added to the equation A4, to make it valid for the range of particles Stokes number ($Stk > 0.01$) in this study (Tien, 1989).

Particle penetration through a filter can be estimated based on the above SFE expressions:

$$P_0 = exp\left(\frac{-4\alpha E_{\Sigma 0} thk_c}{\pi d_f (1-\alpha_c)}\right) \qquad \text{(A5)}$$

In this equation $E_{\Sigma 0}$ is the total SFE, and is defined as $E_{\Sigma 0} = 1-(1-E_{D0})(1-E_{R0})(1-E_{I0})$. Particle penetration through each computational cell (P_0) is calculated using the above equation. The cell dimension here is used as the filter thickness. Note that fiber diameter d_f is constant, but the SVF of the cell (α) will be updated every time some mass is deposited in the cell.

VITA

Shahryar Fotovati

Education:

- **PhD, Mechanical and Nuclear Engineering**
  Virginia Commonwealth University. (Jan. 2009–March 2012)

  Dissertation: Effects of Micro and Macro-Scale Geometrical Parameters on Performance of Pleated Aerosol Filters.

- **M.Sc., Mechanical Engineering**
  Shiraz University. (Sep. 2004–Sep. 2007)

  Thesis: Analysis and Control of Dynamic Stall on an Airfoil in 2-D Compressible Turbulent Flows

- **B.Sc., Mechanical Engineering**
  Persian Gulf University. (Sep. 1996–May 2001)

Journal Publications:

1. **S. Fotovati,** H.V. Tafreshi, 2012, Pleated Filters Performance under Realistic dust load conditions with poly-dispersed particles distribution; Effects of Depth and Surface Deposition, (to be submitted).

2. B. Emami, **S. Fotovati** , H.V. Tafreshi, 2011. Effects of Fiber Orientation on Permeability of Fibrous Media to Power-Law Fluids. *Chemical Engineering Science* (under review).

3. **S. Fotovati**, H.V. Tafreshi, B. Pourdeyhimi, 2011. A Macro-scale Model for Simulating Pressure Drop and Collection Efficiency of Pleated Filters over Time. *Separation and Purification Technology* (under review).

4. **S. Fotovati**, S.A. Hosseini, H.V. Tafreshi, and B. Pourdeyhimi, 2011. Modeling Instantaneous Pressure Drop of Pleated Thin Filter Media during Dust Loading. *Chemical Engineering Science*, 66, 4036-4046.

5. **S. Fotovati**, H.V. Tafreshi, and B. Pourdeyhimi, 2011. Analytical Expressions for Predicting Performance of Aerosol Filtration Media Made up of Trilobal Fibers. *Journal of Hazardous Materials*, 186 (2), 1503-1512.

6. **S. Fotovati**, H.V. Tafreshi, and B. Pourdeyhimi, 2010. Influence of Fiber Orientation Distribution on Performance of Aerosol Filtration. *Chemical Engineering Science*, 65 (18), 5285-5293.

7. **S. Fotovati**, H.V. Tafreshi, *et al.*, 2010. Analytical Expressions for Predicting Capture Efficiency of Bimodal Fibrous Filters. *Journal of Aerosol Science*, 41 (3), 295-305.

Selected Conferences:

- **S. Fotovati**, H.V. Tafreshi, and B. Pourdeyhimi. Transient Modeling of Dust-Loaded Pleated Air Filters. *American Filtration and Separation Society*, June 2012, Boca Raton, FL.

- **S. Fotovati**, H.V. Tafreshi, and B. Pourdeyhimi. Transient Modeling of Dust-Loaded Pleated Air Filters. *American Filtration and Separation Society*, May 9-12, 2011, Louisville, KY.

- **S. Fotovati**, H.V. Tafreshi, and B. Pourdeyhimi. Effect of Fiber Orientation Distribution on Filter Performance. American Filtration and Separation Society, March 22-25, 2010, San Antonio, TX.

- **S. Fotovati**, H.V. Tafreshi, B. Pourdeyhimi. Two-dimensional Modeling of Nanoparticle Collection Efficiency in Bimodal Filters. *American Filtration and Separation Society*, May 4-7, 2009, Minneapolis, MN.

Computational and Programming Skills

CFD Modeling: Turbulence, Aerodynamics, Discrete-Phase and Multi-Phase flows, Porous Media.
Mesh Generation using Algebraic Model, or software.
Strong programming skills with: C++, FORTRAN, MATLAB, UDF.
Software packages: ANSYS-Fluent, GAMBIT, Flex-PDE, GeoDict, TECPLOT, MS Office.
Experienced: AutoCAD, MATHEMATICA, Linux and Windows OS.
Familiarity: CFX, SOLIDWORK, ICEM CFD, R.

Honors and Awards:

Winner of the Best Technical Merit award in semiannual meeting IAB-NCRC (Jun. 2011).

Winner of VCU Dissertation Scholarship-award (Fall 2011).

Member of Honor Society of Phi Kappa Phi (2010-Present).

PhD GPA: 4.0 out of 4.0